

Topological Metamaterials for Engineering Applications

Joshua Feis

Christ Church & Department of Engineering Science
University of Oxford

A thesis submitted for the degree *Doctor of Philosophy.*

Abstract

Topological properties of wave systems link seemingly abstract mathematical quantities with very real physical effects. In recent years, advances in the engineering of metamaterials have allowed for the implementation and application of such effects for electromagnetic waves from radio frequencies all the way to the visible range. With recent advances in the fundamental science underlying topological systems, their vast application potential due to desirable properties of topological effects such as their strongly resonant nature or remarkable robustness against disorder is moving into the spotlight. However, despite the great promise of using topological metamaterials in microwave and radio frequency applications, most work so far has been focused on fundamental and qualitative properties instead of concrete and quantitative studies of their applicability.

The work presented here aims to address this by studying topological metamaterials supporting magnetoinductive waves, a type of excitation that is found in metamaterials comprising magnetically coupled resonant elements such as split ring resonators, with a particular focus on applying them to the construction of wireless links in the microwave and radio frequency range. To this end, a connection between magnetoinductive wave theory and the formalism of quantum theory, which the topology of matter has historically been discussed in, is established. It is shown that magnetoinductive lines may indeed host topological edge states, which are resonant modes in the stopband of the line whose existence is mandated by its topological properties. Based on this result, proposals for the application of topological edge states in wireless power transfer and wireless communication are made. Topological wireless power transfer is

shown to allow for efficiencies comparable to its conventional counterpart based on propagating waves with an increased robustness against disorder as well as reduced electromagnetic pollution. Further, topological wireless communication is revealed to facilitate a significant enhancement in signal power and, in systems with sufficiently low loss and high noise, also in the Shannon capacity of the communication link. Finally, the range limitation of wireless links due to the exponentially localised nature of topological edge states is addressed by the introduction of topological relay interfaces, which enable the construction of longer links while avoiding a degradation in efficiency or signal power.

In summary, this work studies the topological properties of magnetoinductive metamaterials and utilises them in several important engineering applications, showcasing how topological metamaterials may provide various benefits to them.

Contents

1 Fundamentals 1

1.1 Introduction & Outline . . . 1

1.2 Metamaterials . . . 3

1.3 Magnetoinductive metamaterials . . . 6

1.3.1 Magnetic resonators . . . 8

1.3.2 Coupling mechanism . . . 9

1.3.3 Generalised Kirchhoff's law . . . 13

1.3.4 Magnetoinductive waves . . . 14

1.4 Topology . . . 18

1.4.1 Winding numbers . . . 19

1.4.2 Interlude: Hamiltonians . . . 23

1.4.3 Topological physics . . . 26

1.4.4 Symmetry and topology . . . 28

2 Topology of magnetoinductive waves 33

2.1 Circuit Hamiltonian . . . 34

2.2 Diatomic magnetoinductive lines . . . 37

2.3 Topology of diatomic magnetoinductive lines . . . 41

2.3.1 Bloch Hamiltonian . . . 41

2.3.2 Topological invariant . . . 43

2.4 Topological edge states . . . 45

2.5 Conclusions . . . 51

3 Topological wireless power transfer **53**

3.1 Wireless power transfer: Introduction 54

3.2 Asymmetric topological edge states 56

3.2.1 Asymmetry through superposition 56

3.2.2 Asymmetry through tuning 59

3.3 Analysis of topological wireless power transfer 63

3.3.1 Optimal load for efficient power transfer 63

3.3.2 Electromagnetic pollution and safety 66

3.3.3 Robustness against disorder 68

3.4 Conclusions 73

4 Topological wireless communication **75**

4.1 Wireless communication: Introduction 75

4.2 Impedance matching 77

4.3 Analysis of topological wireless communication 79

4.3.1 Power enhancement 80

4.3.2 Robustness against disorder 86

4.3.3 Shannon capacity enhancement 87

4.4 Conclusions 92

5 Topological relay interfaces **95**

5.1 Range limitations 95

5.2 Topological interfaces as relays 97

5.3 Topological wireless links with relay interfaces 100

5.3.1 Wireless power transfer 100

5.3.2 Wireless communication 101

5.4 Conclusions 103

6 Conclusions & Outlook **105**

Bibliography **111**

1 Fundamentals

1.1 Introduction & Outline

In recent years, topological phases of matter have grown into a flourishing field of research, forging links between seemingly abstract mathematical properties of wave systems and showing their very real physical consequences. Topological edge states in particular, which are a type of mode localised at the boundary of a system and mandated by its fundamental mathematical properties, have stimulated considerable interest. A major cause of this attention are their desirable qualities of being both strongly resonant as well as remarkably robust to external disorder [1].

At the same time, considerable advances in the design and fabrication of electromagnetic metamaterials also facilitated efficient engineering of the topological properties of electromagnetic waves [2, 3], giving rise to the rapidly growing field of topological photonics [4, 5]. A significant driver for this field is the great promise that topological photonic systems hold for a plethora of applications, ranging from topological lasers [6, 7] over topological waveguides [8, 9] to topological sensors [10, 11], to name just a few. Nevertheless, particularly for the case of topological metamaterials designed for microwave and radio frequencies, most published work so far remains fundamental and qualitative rather than focused on engineering challenges.

The aim of this thesis is to conduct a study of how, in concrete and quantitative terms, the topological physics of metamaterial systems may benefit several engineering applications in the radio frequency and microwave regime. This work is structured as follows: As the starting point, this first chapter provides an introductory overview over the fundamentals of both metamaterials and topological physics. Based on this, Chapter 2 presents results linking magnetoinductive wave theory and topological physics

by developing a framework to analyse the topological properties of magnetoinductive lines. Chapter 3 applies these results to wireless power transfer, showing that topological wireless power transfer can be as efficient, more robust and less electromagnetically polluting than its conventional counterpart based on propagating waves. Chapter 4 focuses on wireless communication, highlighting the benefits of topological wireless communication, which is shown to offer significantly increased signal powers and, in systems with high noise and low noise, enhanced Shannon capacity. In Chapter 5, range limitations of topological wireless links are discussed and topological relay interfaces are proposed as a solution enabling the circumvention of these limitations. Finally, in Chapter 6 conclusions are drawn and an outlook towards potential future research avenues is given.

Some of the work presented in this thesis also forms part of the following publications:

- **J. Feis**, C. Stevens, E. Shamonina, "Wireless power transfer through asymmetric topological edge states in diatomic chains of coupled meta-atoms", Applied Physics Letters **117** (2020).

- **J. Feis**, L. Solymar, E. Shamonina, "Wireless links via coupled topological edge states", 16th International Congress on Artificial Materials for Novel Wave Phenomena (Metamaterials) (2022).

- **J. Feis**, L. Solymar, E. Shamonina, "Wireless power transfer through asymmetric topological edge states in diatomic chains of coupled meta-atoms", Journal of Applied Physics **133** (2023).

- **J. Feis**, L. Solymar, E. Shamonina, "Topological wireless power transfer with relay edge states", 17th International Congress on Artificial Materials for Novel Wave Phenomena (Metamaterials) (2023).

➤ **J. Feis**, L. Solymar, E. Shamonina, "Topological wireless links with relay interfaces", in preparation (2023).

1.2 Metamaterials

The engineering of materials is a challenge as old as mankind itself; a challenge so important and influencing technological development such that historians have even named periods in time after them: iron age, bronze age, silicon age. However, until recently, all these developments pertained to creating new natural materials made up of atoms and molecules put into their arrangements typically by chemical processes, which makes it difficult if not impossible to tailor material parameters arbitrarily. In the past few decades though, attention has turned towards a new type of not natural but artificial material, one that is not necessarily bound by the properties of its constituent atoms anymore in the way that natural materials are. Going beyond the properties of conventional materials, a new class of materials was born: metamaterials, from the Greek word "μετα" for "beyond".

While, as it is with many young fields, the precise starting points are not easy to determine, this section shall give a brief introduction into the field of metamaterials guided by some landmark results throughout its comparatively short but very active history. The earliest results trace back as far as the works of Maxwell [12] and Lord Rayleigh [13] on the electromagnetic properties of dielectric composites. Quite often, the motivation and desire to create a metamaterial is traced back to early consideration by Veselago [14], who discussed the implications of having both a negative permittivity and permeability in some medium. He showed that, when these parameters are simultaneously negative, the refractive index must turn negative as well. Crucially, he also discovered that a material with such a negative refractive index may focus light like a lens despite not being curved, a phenomenon now typically called Veselago lensing.

Despite this result at first glance sounding a bit outlandish, it leads up to an im-

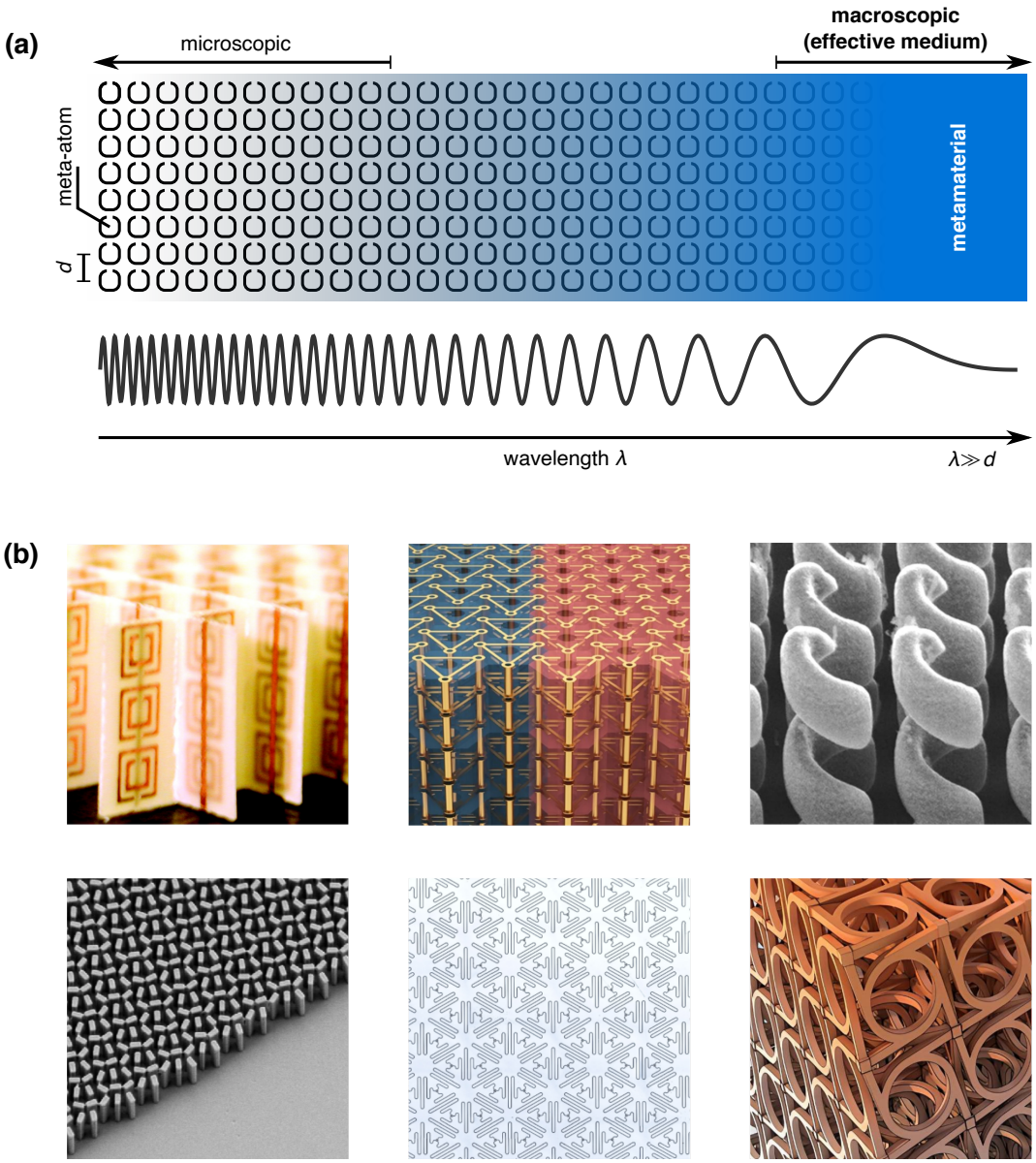


Fig. 1.1: **(a):** Metamaterials are constructed from arrangements of meta-atoms with features smaller than the wavelength ($\lambda \gg d$), where they may be described macroscopically as an effective medium as opposed to a microscopic description of the individual meta-atoms. **(b):** Metamaterials come in a large variety, with meta-atoms designed for various types of waves and across length scales as well as dimensions. Depicted here are several examples of metamaterials. The microwave metamaterial used by Shelby *et al.* to demonstrate negative refraction (top left, adapted from [15]), as well as a microwave metamaterial implementing a 3D topological insulator (top centre, adapted from [16]). At optical wavelengths, a metamaterial made from plasmonic gold helices acting as a broadband circular polariser (top right, adapted from [17]) as well as a dielectric flat metamaterial lens (bottom left, adapted from [18]). Metamaterials have also entered other realms of physics such as with superconducting metamaterials (bottom centre, adapted from [19]) or mechanical metamaterials (bottom right, adapted from [20]).

portant question: How can one control material parameters at will and perhaps even beyond the limits nature seems to impose? The key to answering this question is the *meta-atom*. This smallest subdivision of a metamaterial and how it is coupled to other meta-atoms in the material ultimately dictates its effective properties, just like the atoms do in conventional materials [21, 22]. The term "effective" used here hints at an important concept for metamaterials, which is homogenisation. A key criterion of what one considers a material as opposed to a loose assembly of individual parts is that there is a simpler macroscopic description that may, to a good degree of accuracy, supersede the often complicated behaviour in terms of the individual constituents. The process of finding these effective parameters is called homogenisation. For conventional materials, this is done quite intuitively: When learning about electromagnetism, effective macroscopic parameters such as permeability and permittivity are used without sparing much thought for the complicated quantum mechanics of the atoms the medium is composed of [23]. Of course, if one creates a metamaterial with properties by design, this step from microscopic to macroscopic needs to be understood much better. The key reason is that the wavelength of even visible light at several hundreds of nanometers still does not reach anywhere near resolving the Ångstrom scale that atoms are on. Thus, for natural materials any microscopic features are almost always extremely *sub-wavelength* and can be treated macroscopically. A meta-atom as an artificially engineered object does not automatically obey this rule, so an often-cited law for metamaterials is that their unit cells be sub-wavelength to a degree where the lack of resolution enables effective descriptions [24]. For completeness, it should be noted though that this rule can and is bent sometimes, resulting in interesting phenomenology of its own [25, 26].

Returning to Veselago and his negative refraction, in 2000 Pendry [27] showed that negative refraction could not just facilitate lensing but in fact make a perfect lens without any of the aberrations that plague lenses with positive refractive indices. With this highly desirable goal in sight, it only took until 2001 that a metamaterial was found

by Shelby, Smith and Schultz [15] that made negative refraction an experimental fact. While this by most definitions was certainly not the first metamaterial, it was probably the first of many to bear that name. The meta-atom designed for microwave frequencies that enabled this first observation of negative refraction was a combination of electrically resonant wires allowing for negative permittivity and magnetically resonant split rings allowing for negative permeability (see Fig. 1.1). The latter in particular were quickly shown to be an exceptionally useful building block for metamaterials at many scales, as in 2002 such coupled loops loaded with a capacitance were shown by Shamonina *et al.* [28] to facilitate the propagation of magnetoinductive waves, establishing a highly versatile platform to engineer metamaterials that is used very actively to this day, including in this work. While the following section will discuss these in more detail, an extremely wide range of other metamaterial designs were conceived: To name a few popular examples, plasmonic and dielectric meta-atoms soon extended the reachable wavelength range downwards from microwave to the visible regime [29], but other types of waves such as acoustic and elastic were soon made accessible [30, 31]. Figure 1.1 shows a few landmark examples of these, though the zoo of possible choices has grown exceedingly large by today. The range of possible applications also grew very quickly, from perfect lensing to cloaking [32], sensing [33], imaging [34], wireless power [35], communications [36], and beyond [24, 37].

1.3 Magnetoinductive metamaterials

As mentioned in the previous section, magnetoinductive waves make for a highly versatile framework to design metamaterials within. Magnetoinductive waves were first introduced theoretically by Shamonina in 2002 [28], where it was shown that magnetically coupled lines of resonators are able to support propagating waves. Shortly after, an experimental implementation using split-ring resonators was offered [38], with various alternative implementations across different wavelength regimes following [39–

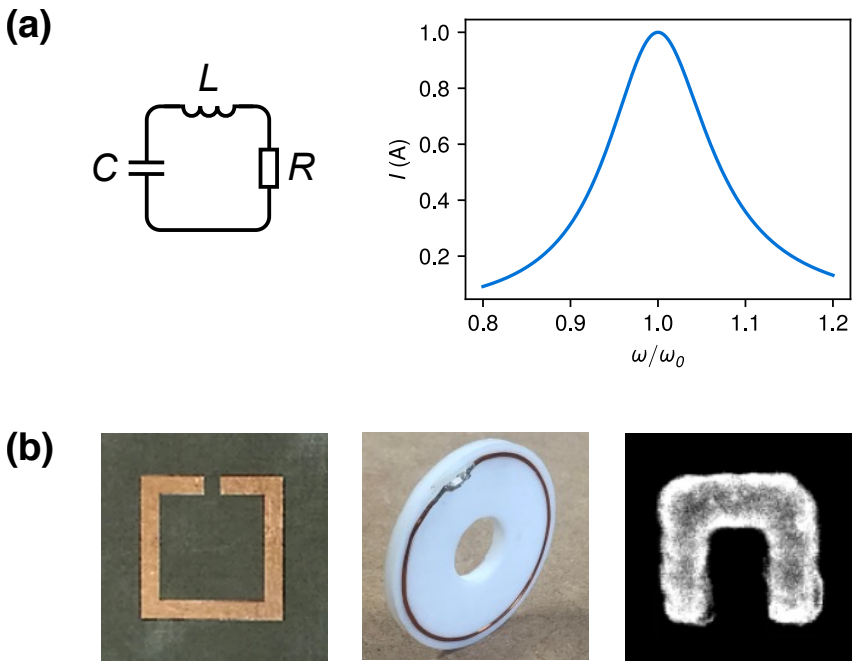


Fig. 1.2: **(a):** Circuit diagram for an *LCR*-resonator, with an inductance L, a capacitance C and a resistance R. **(b):** The meta-atoms for magnetoinductive metamaterials come in all shapes and sizes. A few examples are a split-ring resonator made for operation at microwave frequencies (left, adapted from [55]), a loop loaded with a lumped capacitance for operation at radio frequencies (middle) or a nano-split-ring resonator designed for operation at terahertz frequencies (right, adapted from [56]).

42]. Further, they were generalised to two and three spatial dimensions [43], completing a toolkit to design metamaterials with. Magnetoinductive metamaterials were used, among other applications, to implement wireless power transfer [44], wireless communications [45, 46], directional couplers [47, 48], superdirective antennas [49, 50], as well as sensing [51, 52] and imaging [53, 54] devices.

This section shall serve to introduce the magnetic resonator as the meta-atom for magnetoinductive metamaterials, as well as magnetic induction as their coupling mechanism. Further, the formalism to treat them as well as the simplest example of a structure supporting magnetoinductive waves, the magnetoinductive line, will be discussed.

1.3.1 Magnetic resonators

Ultimately, the properties of any metamaterial are determined by its constituent meta-atoms and how they couple together. Magnetoinductive waves may only propagate on magnetically coupled resonant elements. Hence, the meta-atom for a magnetoinductive metamaterial must also host a resonance. The perhaps simplest magnetic resonators are *LCR*-resonant elements, as sketched in Figure 1.2. They host exactly one resonance and are fully described in terms of the circuit theory of a rather simple circuit containing an inductance L, a capacitance C and a resistance R. Assuming a time-harmonic excitation, i.e. current I and voltage V proportional to $\exp(\mathrm{j}\omega t)$, the ratio of voltage to current is given by the self-impedance of the resonator

$$Z_0(\omega) = \mathrm{j}\omega L + \frac{1}{\mathrm{j}\omega C} + R. \tag{1.1}$$

The resonance occurs at the eigenfrequency of the system, meaning the solution of the system $Z_0 I = 0$ for non-vanishing current, i.e. $Z_0(\omega) = 0$ in the lossless case. Then, the resonant frequency is

$$\omega_0 = \frac{1}{\sqrt{LC}}, \tag{1.2}$$

which can be seen in Figure 1.2(a), where the current peaks at that frequency. The current (for an applied voltage of constant amplitude) follows a Lorentzian curve centred around the resonant frequency with a width of ω_0/Q with the quality factor Q defined as

$$Q = \frac{1}{R}\sqrt{\frac{L}{C}} = \frac{\omega_0 L}{R}. \tag{1.3}$$

The quality factor is a measure of the losses of a resonator, with a higher quality factor and hence sharper resonance corresponding to a structure with lower losses. This fact becomes particularly relevant when multiple resonances are in relative proximity to each other on the frequency axis as for insufficiently high quality factors they may overlap and thus mix significantly.

This type of model of meta-atoms as relatively simple resonators works well, though it should be emphasised that it of course has certain limits. In particular, as frequencies go higher the parameters of the resonator become noticeably dispersive, particularly towards optical frequencies [57–59]. Additionally, an *LCR* resonator only hosts one resonance but many meta-atoms have higher resonances which are thus not captured by this simplest model. Nonetheless, there is a large set of meta-atoms that do follow this behaviour for a wide range range of frequencies hence allowing for this model to be used as a convenient design tool for them.

1.3.2 Coupling mechanism

The second and key ingredient and what allows for a pile of meta-atoms to be turned into an actual metamaterial is the mechanism coupling the meta-atoms. As the name of the magnetoinductive metamaterial suggests, the physical effect behind its coupling mechanism is magnetic induction. The following subsection is a brief sketch of how magnetic induction leads to the coupling of meta-atoms *via* mutual induction. The physics of magnetic induction is formalised in one of Maxwell's equations, namely Faraday's law of induction. It reads:

$$-\frac{\partial \Phi}{\partial t} = -\frac{\partial}{\partial t}\int_C \mathbf{B}\cdot \mathrm{d}\mathbf{A} = \int_{\partial C} \mathbf{E}\cdot \mathrm{d}\mathbf{r}. \tag{1.4}$$

In plain words instead of mathematics, this equation states that a change in magnetic flux Φ, which is the integral of a magnetic field piercing some surface C, induces an electric field $\mathbf{E}$. Given two loops of wire, such as they are sketched in Fig. 1.3, this results in a mutual induction, i.e.

$$\frac{\partial \Phi_{12}}{\partial t} = \frac{\partial}{\partial t}\int_{C_2} \mathbf{B}_1 \cdot \mathrm{d}\mathbf{r}. \tag{1.5}$$

Here, Φ_{ij} denotes the magnetic flux through coil j caused by the magnetic field $\mathbf{B}_i$ of

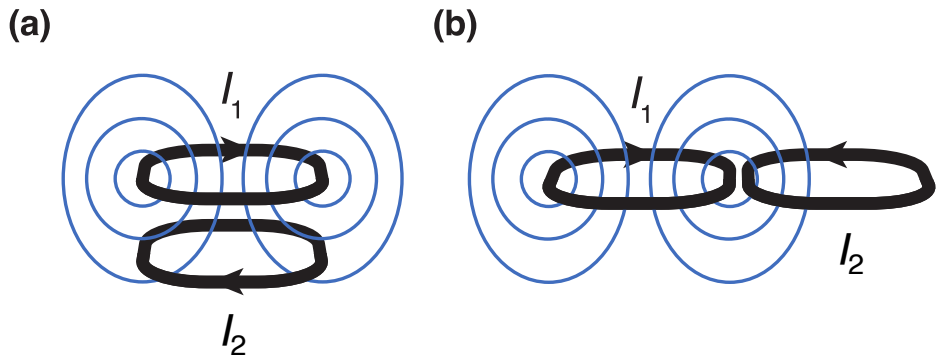


Fig. 1.3: A loop of wire with a current flowing through it generates a magnetic field. When the magnetic field lines, sketched in blue here, penetrate another loop, they cause magnetic induction, i.e. there is a voltage induced in this other loop. For magnetoinductive waves, there are two main arrangements that are typically considered, the axial arrangement (shown in **(a)**) and the planar arrangement (shown in **(b)**). The mutual inductance is positive in the axial case and negative in the planar case.

coil i and C_j is a surface bounded by the wire of the coil. Since the magnetic field of such a loop of wire is directly proportional to the current flowing through it, $\mathbf{B}_1 \propto I_1$, and assuming that the current is spatially constant everywhere along the wire, ratio of induced flux to current is a constant called the mutual inductance

$$M_{12} = \frac{\Phi_{12}}{I_1}. \tag{1.6}$$

Since, as Eq. (1.4) states, a change in flux induces an electric field along the wire, a current in coil 1 will induce a voltage in coil 2

$$U_2 = M_{12}\frac{\partial I_1}{\partial t}. \tag{1.7}$$

Assuming harmonic currents, i.e. $I_1 \propto \exp(\mathrm{j}\omega t)$ gives an expression for a mutual impedance $Z_{12} = U_2/I_1$ as

$$Z_{12} = \mathrm{j}\omega M_{12}. \tag{1.8}$$

Note that due to the reciprocity of electromagnetism, $Z_{12} = Z_{21}$ must hold. Additionally, the generalisation of this mechanism to more than two loops is straightforward: Any two loops i and j exhibit mutual induction according to

$$Z_{ij} = \mathrm{j}\omega M_{ij}. \tag{1.9}$$

There are two main arrangements to consider when discussing mutual induction, the axial case where the loops face each other as well as the planar case where they are adjacent to each other. In the former case, the mutual inductance is positive while in the latter case it is negative. It should be noted that when considering the inevitable radiation losses [40] or induction through lossy media [60], it may well turn complex. For this work though, it is assumed to be real. Additionally, it should be mentioned that typically M is bounded by the self-inductance L as

$$-L \leq M \leq L, \tag{1.10}$$

since any a wire loop may not induce a greater flux in another wire loop than it does in itself. Finally, it is important to briefly show the form for the mutual inductance for a relevant case, where a simple analytical solution is possible, namely for small wire loops. A wire loop can be considered small if its dimensions are sufficiently below the wavelength, i.e. $r_0 \ll \lambda$, where r_0 is the radius of the loop. The analytical expression for the magnetic field of a loop contains lengthy elliptical integrals [23] and shall not be shown here, but for a small loop may be expanded in λ/r_0 [61]. Neglecting all higher order terms under the assumption $\lambda/r_0 \ll 1$ shows that the magnetic field is equal to that of a magnetic dipole generated by a current I in zeroth order, reading [62]

$$\mathbf{B} = \mu_0 \frac{r_0^2 I}{2\pi r^3} \left[\mathbf{e}_r \cos(\theta) + \mathbf{e}_\theta \sin(\theta)\right], \tag{1.11}$$

where $\mathbf{e}_r$ and $\mathbf{e}_\theta$ denote the unit vectors in spherical coordinates and μ_0 is the magnetic permeability of vacuum [23]. Correspondingly, the magnetic flux of this field threading another small loop a distance d away both for the axial arrangement ($\theta = 0$) and the planar arrangement ($\theta = \pi/2$) reads

$$\Phi = \left(\pi r_0^2\right) \frac{\mu_0 r_0^2 I}{2\pi d^3}. \tag{1.12}$$

Then, the mutual inductance between the two loops is

$$M = \frac{\Phi}{I} \propto \frac{1}{d^3}, \tag{1.13}$$

showing that the mutual inductance between two small loops follows an inverse cubic law.

Before moving to metamaterials with typically many elements, it is instructive to consider what happens when coupling few elements to gain an understanding of the coupling mechanism. For two coupled elements both being resonators with self-impedance Z_0 of the type discussed in the previous section, the system for currents and voltages reads

$$\begin{aligned} Z_0 I_1 + \mathrm{j}\omega M I_2 &= V_1 \\ Z_0 I_2 + \mathrm{j}\omega M I_1 &= V_2. \end{aligned} \tag{1.14}$$

Once again, the resonances may be found at the eigenfrequencies of the system, though this time the condition for a non-trivial solution (i.e. one with non-zero currents), is

$$\det \begin{bmatrix} Z_0 & \mathrm{j}\omega M \\ \mathrm{j}\omega M & Z_0 \end{bmatrix} = 0. \tag{1.15}$$

The solutions for the eigenfrequencies are

$$\omega_{1,2} = \omega_0 \sqrt{\frac{2}{2 \pm \kappa}}, \tag{1.16}$$

where the dimensionless coupling coefficient is defined as:

$$\kappa = \frac{2M}{L}. \tag{1.17}$$

The two eigenfrequencies are split around the resonant frequency of the individual resonator ω_0. One of the eigenfrequencies belongs to a symmetric mode where the currents through the two resonators oscillate in phase and the other to an anti-symmetric one where they oscillate in antiphase. For positive coupling, the anti-symmetric mode belongs to the higher resonant frequencies whereas for negative coupling this is reversed. This is in direct analogy to the bonding and anti-bonding of molecular orbitals, from which the band structures of solids ultimately arises [63].

1.3.3 Generalised Kirchhoff's law

This intermediate section is dedicated to a brief recapitulation of Kirchhoff's law, in particular a matrix version thereof also referred to as generalised Kirchhoff's law [43, 64]. Its elegant form significantly simplifies the description of magnetoinductive waves in metamaterials of finite size in the remainder of this work. Thus, it forms an integral tool in the unearthing of the results presented here. A motivation for writing Kirchhoff's law in matrix form could already be taken from the end of the previous section, where for two coupled resonators, a system of equations arises for which a matrix formulation helped extract certain results such as the resonant frequencies of the coupled pair. To generalise this approach to systems with an arbitrary number N of coupled resonators, one has to define a current vector $\mathbf{I}$ and a voltage vector $\mathbf{V}$ as

$$\mathbf{I} = \begin{bmatrix} I_1 \\ I_2 \\ \vdots \\ I_N \end{bmatrix} \quad \text{and} \quad \mathbf{V} = \begin{bmatrix} V_1 \\ V_2 \\ \vdots \\ V_N \end{bmatrix} \tag{1.18}$$

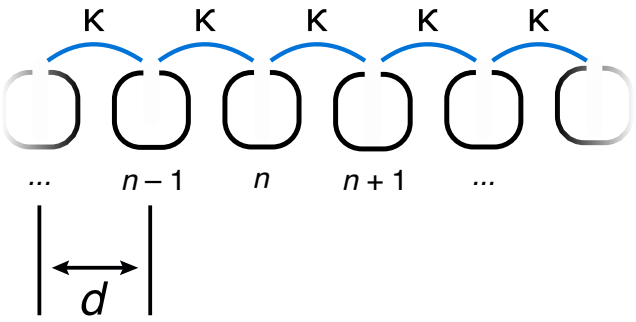


Fig. 1.4: Illustration of a monoatomic magnetoinductive line with a lattice spacing d, coupled via nearest-neighbour coupling with coupling coefficient κ.

One may write down the linear system given by Kirchhoff's equations in a very compact form by defining an impedance matrix Z. The generalised Kirchhoff's law then reads

$$Z\mathbf{I} = \mathbf{V}. \tag{1.19}$$

Written like this, extracting the response of a system to some application of external voltage becomes as elegant as a matrix inversion. Additionally, the calculation of eigenfrequencies in lossless systems may generally be performed by finding the singularities of the impedance matrix along the frequency axis, i.e. by solving the equation

$$\det Z(\omega) = 0. \tag{1.20}$$

For magnetoinductive metamaterials with the assumption of short-range coupling, this matrix is tridiagonal and hence also relatively sparse, allowing for a highly efficient numerical treatment.

1.3.4 Magnetoinductive waves

Equipped with an understanding of the magnetic resonators as the meta-atoms for magnetoinductive metamaterials, their coupling mechanism as well as how to treat them, the next step is to study the excitations of many magnetic resonators coupled together: magnetoinductive waves. The simplest possible structure for magnetoinduc-

tive waves to propagate on is a one-dimensional line of identical resonators, each with a self-impedance of Z_0, each coupled by the same mutual inductance M to their nearest neighbours. Figure 1.4 illustrates this arrangement. For such an infinite length of the chain of resonators, the constitutive equations read

$$Z_0 I_n + \mathrm{j}\omega M(I_{n-1} + I_{n+1}) = 0. \tag{1.21}$$

Alternatively, the elements of the (infinite-dimensional) impedance matrix $Z(\omega)$ are

$$Z_{n,n} = Z_0 \tag{1.22}$$

and

$$Z_{n,n+1} = \mathrm{j}\omega M = Z_{n+1,n}, \tag{1.23}$$

which, as mentioned above, is a tridiagonal matrix. The first step to describe waves on such a structure is to derive a dispersion relation by making a Bloch *ansatz* for a plane wave in a monoatomic structure as

$$I_n = I_0 \mathrm{e}^{-\mathrm{j}knd}. \tag{1.24}$$

The quantity d denotes a lattice spacing of the magnetoinductive line. The wave number $k = \beta - \mathrm{j}\alpha$ is typically split into its real part β, the propagation constant, and its negative imaginary part α, the attenuation constant. Inserting the wave *ansatz* for the current into the constitutive equation yields

$$Z_0 + \mathrm{j}\omega M\left(\mathrm{e}^{\mathrm{j}kd} + \mathrm{e}^{-\mathrm{j}kd}\right) = 0. \tag{1.25}$$

Rearrangement then leads to a formula for the wave number, and thus the dispersion relation for magnetoinductive waves on monoatomic lines,

$$\cos(kd) = \frac{2Z_0}{\mathrm{j}\omega M}, \tag{1.26}$$

which, using the definition of the self-impedance

$$Z_0 = \mathrm{j}\omega L + \frac{1}{\mathrm{j}\omega C} + R = \mathrm{j}\omega L\left(1 - \frac{\omega_0^2}{\omega^2} - \mathrm{j}\frac{\omega_0}{\omega Q}\right), \tag{1.27}$$

and the coupling coefficient

$$\kappa = \frac{2M}{L}, \tag{1.28}$$

may be separated into real part

$$\kappa\cos(\beta d)\cosh(\alpha d) = \frac{\omega_0^2}{\omega^2} - 1, \tag{1.29}$$

and imaginary part

$$\kappa\sin(\beta d)\sinh(\alpha d) = \frac{\omega_0}{\omega Q}. \tag{1.30}$$

For small losses (i.e. $\alpha d \ll 1$), it is possible to find a simplified relation for the attenuation constant as

$$\alpha d = \frac{1}{Q\kappa\sin(\beta d)}. \tag{1.31}$$

From this it can be seen that attenuation in lossy structures is increased approximately proportionally by both the quality factor and the coupling coefficients - in more intuitive words, structures with higher losses per element and weaker coupling attenuate magnetoinductive waves more.

In Figure 1.5, the dispersion diagrams for the monoatomic magnetoinductive line with a coupling coefficient of $\kappa = 0.2$ are shown. A sharp increase of the attenuation outside a certain interval can be seen there, showing the formation of a single band outside of which waves cannot propagate. Frequency ranges where waves can propagate

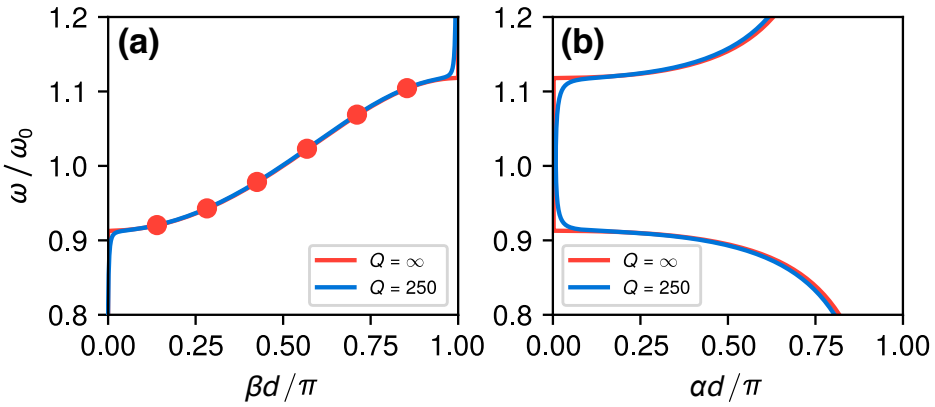


Fig. 1.5: Dispersion characteristics of a monoatomic magnetoinductive line for both lossless ($Q = \infty$) and lossy ($Q = 250$) cases, with $\kappa = 0.2$. **(a):** Dispersion diagram for the real part of the wave number, the propagation constant β. The red dots display the discrete resonant frequencies of a finite-length line with a length of $N = 6$. **(b):** Dispersion diagram for the attenuation constant α, the negative imaginary part of the wave number.

are called passbands or sometimes just bands and regions where they cannot are called stopbands. For a lossy structure with $Q = 250$, it can further be seen that some attenuation due to the resistance of the individual resonators also persists inside the band. The group velocity of the wave, defined as

$$v_g = \frac{\partial \omega}{\partial \beta}, \tag{1.32}$$

can be seen to taper off towards the edge of the band. Further note that the group velocity is of a single sign throughout the band but that flipping the sign of κ also flips the sign of the group velocity. This means that magnetoinductive lines with negative coupling, also exhibit a negative group velocity meaning they support what is known as backward waves. For backward waves, the direction of the energy flow, which is determined by the Poynting vector, points away from the source, but the phase velocity of the waves, defined as

$$v_p = \frac{\omega}{\beta} \tag{1.33}$$

points the opposite way [28].

While these results are assuming infinite-length lines, they also predict the be-

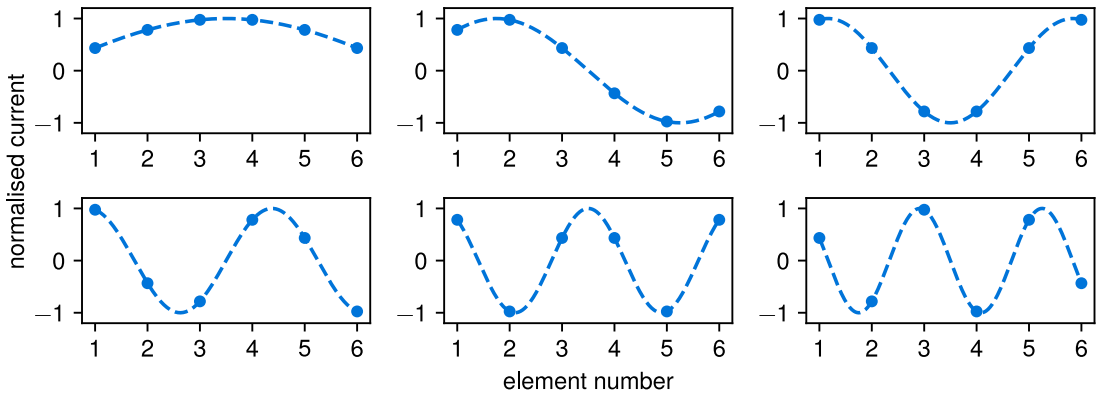


Fig. 1.6: Current eigenvectors for a monoatomic magnetoinductive line of length $N = 6$ with coupling $\kappa = 0.2$. The dashed lines show the continuous shape of the standing waves corresponding to each resonance. Each of the N resonances is a standing wave with a number of nodes ranging from 0 to $N - 1$.

haviour of finite lines. Calculating the resonant frequencies of a lossless line with a finite length of $N = 6$, it is shown in Figure 1.5(a) that they match the predicted dispersion perfectly. The wave numbers for the discrete resonances are

$$k_l d = \frac{\pi l}{N+1}, \tag{1.34}$$

where $1 \leq l \leq N$ indexes the resonances. The corresponding normalised current eigenvectors read

$$\left(\mathbf{I}^{(l)}\right)_n = \frac{2}{N+1} \sin\left(n k_l d\right), \tag{1.35}$$

where the superscript l indexes the eigenvector number and n denotes the element index of the current vector. For the case $N = 6$, these are displayed in Figure 1.6. They are standing waves with $l - 1$ nodes each, as shown by the dashed lines displaying the continuous shapes of Eq. (1.35).

1.4 Topology

At its heart, and without much thought about precise definitions, topology is a classification system for mathematical objects [65]. Typically, mathematics aims to make

statements with the most generality possible. Correspondingly, the detailed properties of some mathematical object are more of a hindrance than a help, as they offer no additional useful information about the object. Topology solves this problem by finding so-called topological invariants, a key property of a mathematical object in topology [65]. The topological invariant assigned to an object must stay the same, even if this object is transformed continuously. If one thinks of geometrical objects, this typically refers to any transformation that does not involve cutting the object in any way but merely deforms it. Since any two objects with the same topological invariant are the same up to a continuous transformation, i.e. topologically equivalent, they belong to a class of objects indexed by the topological invariant. Statements can be made about the objects in said class without ever paying attention to their details. Hence, topology works much like a filing system: As illustrated in Figure 1.7, different objects may be categorised into folders with the same topological invariant, allowing to ascend one step in the hierarchy and pay attention to the topology of the objects instead of the objects themselves. Admittedly, this is a very general formalism and not much has been said here about what concrete topological invariants may look like. As the variety of possible topological invariants is infinite, the next subsection shall provide a specific example of a topological invariant, which will also be of use in the further course of this work.

1.4.1 Winding numbers

One possible, commonly cited example for a topological invariant is the winding number [65]. Intuitively, the winding number is the amount of times a curve winds around a reference point, as sketched in Figure 1.8. The winding number shall serve as an introductory example of how to define a topological invariant and further of how to show that the presumed invariant is indeed one.

To that end, consider an arbitrary but definite closed curve in two spatial dimensions that does not pass through the origin. The coordinates of the two-dimensional

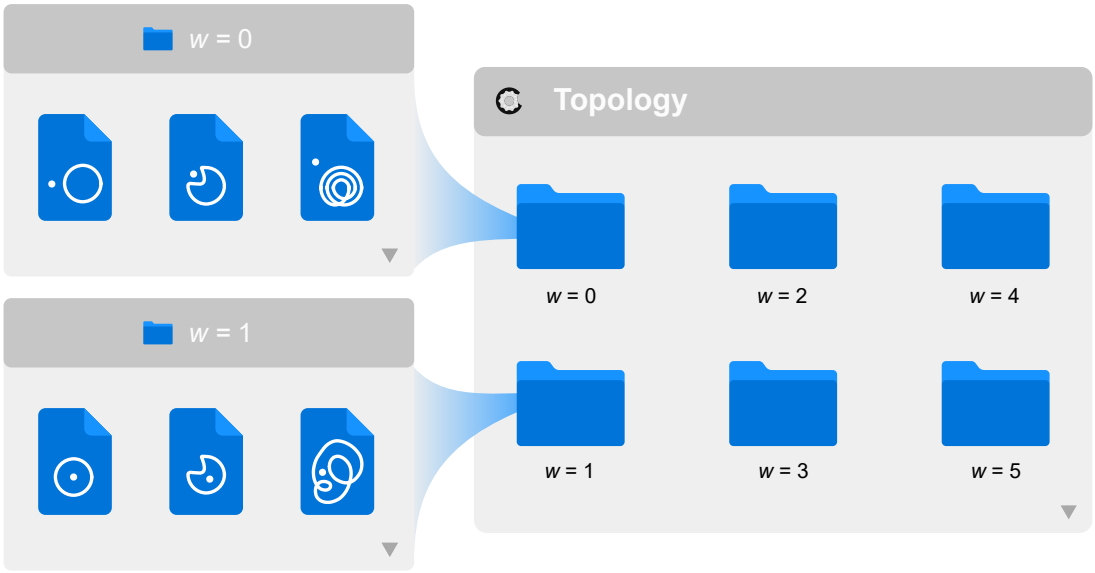


Fig. 1.7: Much like in a filing system, as shown in this illustration here, topology aims to classify mathematical objects by finding properties that remain unchanged even when the object is subjected to a continuous transformation. These properties are called topological invariants. In this illustration here, different objects are categorised into their topological classes by an invariant w. While they are not identical, they are topologically equivalent.

space, for the sake of elegance, are written as the real and imaginary part of a complex number. Then, written in polar coordinates, there is a continuous parametrisation $\gamma : [0,1] \longrightarrow \mathbb{C} \setminus \{0\}$ of this curve which reads

$$\gamma(s) = r(s)\mathrm{e}^{\mathrm{j}\phi(s)}, \tag{1.36}$$

with a parameter $s \in [0,1]$, a radial coordinate or amplitude $r(s) \in \mathbb{R}$ and a phase angle of $\phi(s) \in \mathbb{R}$. $\mathbb{C}\setminus\{0\}$ denotes the complex plane with the origin excluded and $\gamma(1) = \gamma(0)$ indicates that $\gamma(s)$ is a closed curve on the interval $[0,1]$. The angle ϕ determines how fast and hence how often the curve loops before closing on itself. One more restriction needs to be placed on the choice $\phi(s)$, namely that it is continuous. Otherwise, in principle, there are choices for $\phi(s)$ where it may jump by multiples of 2π along the curve, which describes the same curve but makes it unsuitable to determine the winding number of the curve. Since any discontinuity in $\phi(s)$ may be eliminated by simply

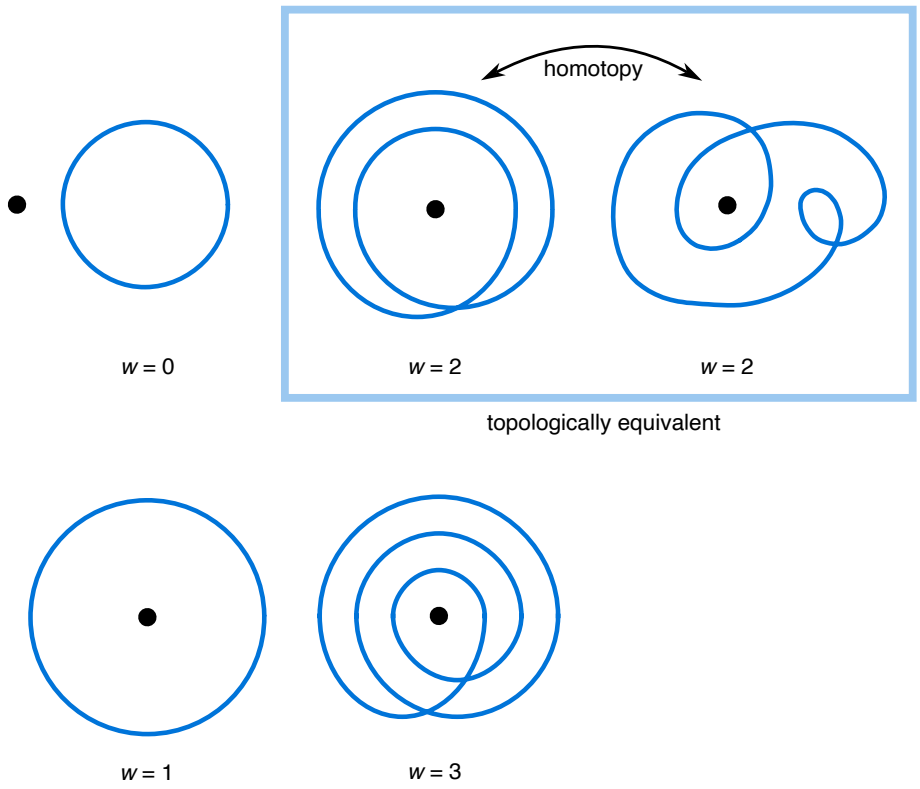


Fig. 1.8: The winding number w is a topological invariant of closed curves in the plane. It is defined as the number of times the curve winds around a common reference point, as shown here for a few examples with different winding numbers. Curves with the same winding number, such as the two examples with $w = 2$ here, are called topologically equivalent or homotopic as they are connected by a continuous transformation called a homotopy.

subtracting it, a parametrisation with continuous $\phi(s)$ can always be found. This choice is also often denoted as $\arg \gamma(s)$.

With this motivation and the preliminaries in place, the winding number around the origin shall be defined as

$$w = \frac{1}{2\pi \mathrm{j}} \int_0^1 \frac{\mathrm{d}}{\mathrm{d}s} \ln \gamma(s) \, \mathrm{d}s = \frac{\phi(1) - \phi(0)}{2\pi} \in \mathbb{Z}. \tag{1.37}$$

The fact that the winding number must be an integer is due to the curves under consideration being closed as otherwise $\gamma(1) \neq \gamma(0)$. Note that this definition of the winding number relies on the explicit exclusion of curves that pass through the origin. The reason for this is that the winding occurs around a reference point and is thus ill-defined

for a curve that passes through this point, here being the origin.

The claim to prove now is that w is indeed a topological invariant for curves. To that end, consider another curve $\tilde{\gamma}$ which may be continuously deformed into γ, meaning there exists a continuous function $H : [0,1]\times[0,1] \longrightarrow \mathbb{C}\setminus\{0\}$ such that for $H(s,u)$

$$H(s,0) = \gamma(s) \;\text{ and }\; H(s,1) = \tilde{\gamma}(s), \tag{1.38}$$

with $u \in [0,1]$ being the transformation parameter, holds. In words, this transformation means that the two curves can be deformed into each other without crossing the origin, where the winding number would not be defined. Should w really be a topological invariant, then it must be the same for both of these curves as they are connected by a continuous transformation and correspondingly topologically equivalent. In concrete terms,

$$w[\gamma] = w[\tilde{\gamma}] \tag{1.39}$$

needs to hold.

Suppose the winding number now somehow depends on the transformation parameter u:

$$w(u) = \frac{1}{2\pi \mathrm{j}} \int_0^1 \frac{\mathrm{d}}{\mathrm{d}s} \ln H(s,u)\, \mathrm{d}s. \tag{1.40}$$

As noted above, $w(u) \in \mathbb{Z}$ for all u. In turn, this means that any hypothetical change of the winding number is a discontinuity of $w(u)$. Correspondingly, if $w(u)$ were found to be a continuous function this would directly imply it being constant as well.

Indeed, the continuity of $w(u)$ is readily apparent if it is expressed as

$$w(u) = \frac{\arg H(1,u) - \arg H(0,u)}{2\pi}. \tag{1.41}$$

Since compositions of continuous functions are themselves continuous and arg was chosen to be continuous, so is $w(u)$. Hence, $w(u)$ is a constant integer and the winding number is invariant for two curves connected by a continuous transformation, and thus

it is indeed a topological invariant. The function H connecting them is also known as a *homotopy* with and any two functions γ and $\tilde{\gamma}$ connected by it are called *homotopic*.

1.4.2 Interlude: Hamiltonians

While topological physics may be explained without giving reference to Hamiltonians, its origins in condensed matter physics mean that this would constitute a disconnect to the majority of literature in the field. This subsection shall serve as a brief introduction into Hamiltonians as understood in the context of this thesis. One simplification that is assumed here is that of time-independence, meaning the parameters of any system shall not vary with time. Given that, the Schrödinger equation reads

$$\mathcal{H}\psi = E(\omega)\psi. \tag{1.42}$$

Here, ψ is an eigenmode of the system and $E(\omega)$ the corresponding eigenenergy, which is directly related to the eigenfrequency ω that is more commonly discussed in the field of metamaterials. If for a system there is an eigenvalue problem relating such an eigenmode to its eigenfrequency, the operator appearing in this problem is called the Hamiltonian $\mathcal{H}$. Note that this definition is not strict in a sense of mathematical physics but is still sufficiently precise in the context of this and related work. While, in general, $\mathcal{H}$ may be any linear operator including differential operators, in systems with discrete or at least countably infinite spectra, $\mathcal{H}$ can always be represented as a complex matrix and ψ as a complex vector. In crystals in general and metamaterials specifically due to their discrete nature, this holds. Hence, for simplicity and given it is sufficient, $\mathcal{H}$ will be treated accordingly in this thesis. The terms operator and its representation as a matrix shall also be used interchangeably here. Note that $\mathcal{H}$ for a system without gain or loss will be Hermitian, i.e.

$$\mathcal{H}^\dagger = \mathcal{H}, \tag{1.43}$$

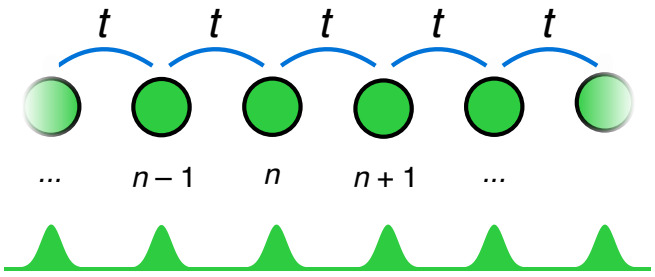


Fig. 1.9: Illustration of a monoatomic tight-binding model in one dimension. The highly localised electronic wave functions allow for an effective description in terms of a nearest neighbour coupling quantified by a hopping strength t.

where $\mathcal{H}^\dagger$ denotes the conjugate transpose of $\mathcal{H}$. Correspondingly, the eigenenergies of a system with a Hermitian Hamiltonian will be real, while for a system with gain and/or loss they may be complex. As each eigenmode will evolve in time according to

$$\psi(t) = \psi(0)e^{j\omega t}, \tag{1.44}$$

a complex eigenfrequency directly implies an exponential decay of the eigenmode profile over time (or, in the less commonly discussed case of gain, also an exponential rise).

Having introduced this formalism, the remainder of this subsection is dedicated to the example of a particular type of Hamiltonian: A specific, prototypical example originating from solid state physics are tight-binding Hamiltonians. These describe systems with electrons that are tightly bound, meaning the electrons are strongly localised at the sites of the atoms. Correspondingly, the electronic wave functions of the individual electrons have only a small overlap and do not strongly influence each other. This is illustrated in Figure 1.9 for a monoatomic tight-binding model. Conversely, in a metal for example, which constitutes the other extreme, electrons are essentially un-

bound and behaving as one extended gas. A tight-binding Hamiltonian in one spatial dimension can typically be written as

$$(\mathcal{H})_{ij} = \begin{cases} E_i, & i = j \\ \\ t_{i,j}, & i \neq j \end{cases}, \tag{1.45}$$

where E_i are the on-site energies and $t_{i,j}$ are the so-called hopping strengths. As will be shown later, for a magnetoinductive metamaterial we can find an equivalent description where the on-site energies are determined by the self-impedances and the hopping strengths by the mutual impedances of the resonators. If

$$t_{i,j} = 0, \ |i - j| \leq 1, \tag{1.46}$$

then the tight-binding model makes the assumption of nearest-neighbour interactions only, meaning that exactly like in the preceding example for magnetoinductive waves, any overlaps between wave functions not belonging to nearest neighbours are assumed to be negligible. Throughout this thesis, this approximation will hold, though in principle the formalism admits more complicated models.

For systems with spatial periodicity and hence periodic Hamiltonians, such as metamaterials, some further statements can be made. Specifically, the Bloch theorem states that all solutions may also be factorised into a periodic part u_l, which is identical for each unit cell, and a plane wave part. They thus have the form

$$\psi_l = u_l \mathrm{e}^{-\mathrm{j}kx}. \tag{1.47}$$

Here, the index l denotes the so-called internal degrees of freedom of the system, i.e. how many different amplitudes are required to describe one unit cell. The perhaps simplest internal degree of freedom is the number of atoms per unit cell, but in principle others such as higher-order resonances are also possible. As an example, for a

monoatomic structure $l = 1$ only (and hence not needed) or for a diatomic structure $l \in \{1, 2\}$. This limitation on the form and number of solutions means that the description of the full system is not needed but instead the equations describing the system can be reduced drastically to be equal to the number of internal degrees of freedom. Hence, the Schrödinger equation can be rewritten as

$$\mathcal{H}(k)\mathbf{u} = E(k, \omega)\mathbf{u}, \tag{1.48}$$

where the vector $\mathbf{u}$ contains the Bloch functions u_l and $\mathcal{H}(k)$ is called the Bloch Hamiltonian, the dimensionality of which crucially equals the number of internal degrees of freedoms (e.g. atoms). For periodic structures this is always smaller than the dimensionality of the Hamiltonian $\mathcal{H}$, and hence this typically significantly simplifies the mathematical description.

1.4.3 Topological physics

So far, topology has remained purely mathematical in its use. As a tool for physics, which may come as a surprise to some as the roots of topology lie in mathematical but also deeply abstract questions, it was brought into wide use more or less by accident. In 1980, Klaus von Klitzing performed experiments on the Hall effect, measuring the Hall resistance of samples with increasing magnetic field. To his surprise, he found that instead of the linear relationship typically expected for the Hall effect, plateaus, as shown for example in Figure 1.10, showed up throughout his measurements of the Hall resistance [67]. Moreover, these plateaus occurred at regular intervals of the inverse of the magnetic field, meaning

$$R_{\text{Hall}} \propto \frac{1}{\nu}, \tag{1.49}$$

where $\nu \in \mathbb{N}$ is an index counting the plateaus. Intriguingly, these plateaus occur at the exact same values of resistance no matter the properties of the sample, even when

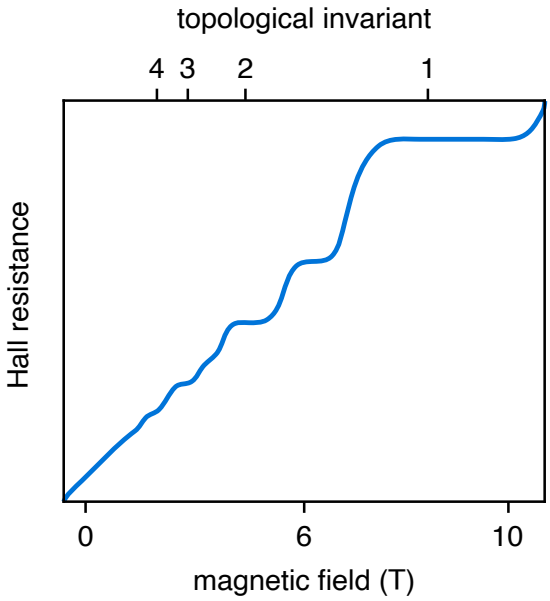


Fig. 1.10: The quantum Hall effect is the occurrence of extremely stable resistance plateaus in certain materials against an increasing magnetic field. These resistance plateaus do not depend on the properties of the sample, and samples with random disorder are in fact needed to observe them. The plateaus occur at integer values of the inverse of the magnetic field. These integers are a topological invariant of the system, which shows how topological properties of a system have observable consequences for its physical behaviour. (Hall resistance data taken from [66].)

they were not pure but contained significant amounts of random disorder. This discovery, known as the quantum Hall effect, being highly useful to the measurement science which aims for universal and accurate standardisation, lead to von Klitzing being awarded the Nobel price in physics just five years later.

Two years after the initial discovery, an explanation was given by Thouless, which would become the cornerstone of topological physics: the number ν, is in fact a topological invariant (now called the TKNN invariant) of the system or, in quantum mechanical terms, its Hamiltonian [68]. The topology of the system being responsible for the quantum Hall plateaus explains both the regularity with which the plateaus occur as well as their remarkable independence of the precise parameters of the system. Any change which could at least approximately be considered a continuous transformation of the system would, just like for the winding numbers of the curves, not change the invariant and hence also not the plateau. In 2016, Thouless too, together with Haldane and Kosterlitz, received a Nobel prize in physics for this discovery. The wider

understanding that topology could in fact influence the physics of a system meant that throughout all field of physics from electronics [69] and acoustics [70] to photonics [5] and beyond, topological invariants were searched and their physical effects studied. In this thesis, one specific invariant and its effects are meaningful, but many more have been found [71]. Just as in mathematics, the topological invariants of physical systems come in a variety of forms, and identifying them (which is often the hard part) and exploring their physical consequences is still an ongoing effort.

1.4.4 Symmetry and topology

While the question how to construct topological invariants is far from clear, the matter of their existence is better understood. It turns out that it is possible, based on symmetry constraints for the Hamiltonian, to predict whether a system should have a topological invariant or not. Moreover, it is even possible to make some limited statements over what this invariant should look like. However, a method to systematically identify what the invariant looks like is yet to be found, with contemporary efforts often aiming at using machine learning to spot them [72].

To gain information on the existence of a topological invariant in a system, one must consider three types of symmetry a Hamiltonian may or may not have. In the following, these symmetries are briefly presented from two perspectives - an intuitive physical and a rigorous mathematical one. From the physics perspective, a symmetry is any change that can be made to a system with no meaningful change in any of its observable behaviour. Mathematically, a symmetry may be defined as a mathematical property of the Hamiltonian. A system possesses a symmetry, written as an operator $\mathcal{S}$, if and only if the Hamiltonian stays invariant under a similarity transformation with it, i.e.:

$$\mathcal{S}^{-1}\mathcal{H}\mathcal{S} = \pm\mathcal{H}. \tag{1.50}$$

Hence, different types of symmetries are often classified by the mathematical properties of $\mathcal{S}$. First, there is time-reversal symmetry. Very generally speaking, this means that there is some anti-unitary operator $\mathcal{T}$ such that

$$\mathcal{T}^{-1}\mathcal{H}\mathcal{T} = \mathcal{H}. \tag{1.51}$$

Anti-unitarity is the composition of a unitary operator together with a complex conjugation, i.e. $\mathcal{T} = \mathcal{U}\mathcal{K}$ for some unitary matrix $\mathcal{U}$ and the complex conjugation operator $\mathcal{K}$. Hence, the perhaps simplest example of time-reversal symmetry is if the Hamiltonian is purely real, choosing $\mathcal{T} = \mathcal{K}$. In words and not mathematics, this condition formalises that reversing the flow of time in the system leads to the same dynamics. The prototypical of breaking this condition in electromagnetism is through gyrotropy, as magnetic fields are inherently not time-reversal invariant.

The second symmetry is the particle-hole symmetry $\mathcal{P}$. As the name implies, it originates from semiconductor physics, where it was found that certain systems possess a symmetry whereby the system behaves the same even if electrons and holes are swapped. More generally, this means that the physics of systems with particle-hole symmetry behave the same when swapping eigenmodes belonging to the lower band with their counterparts belonging to the upper band and *vice versa*. As a corollary, this also immediately implies that the band structure must be symmetric about some constant frequency which separates upper and lower bands. Mathematically, $\mathcal{P}$ is again anti-unitary but now

$$\mathcal{P}^{-1}\mathcal{H}\mathcal{P} = -\mathcal{H} \tag{1.52}$$

should hold.

The third symmetry carries two names that are quite often used interchangeably: chiral or sublattice symmetry. This symmetry applies to systems where sublattices can be defined, e.g. where all atoms can be grouped into two sets that only couple to the

Tab. 1.1: Physical systems may be grouped into symmetry classes according to symmetries that their Hamiltonian has. Together with the dimensionality of the system, this class serves as a predictor of whether the system may have a topological invariant and if it is a whole number ($\mathbb{Z}$), an even whole number ($2\mathbb{Z}$) or a whole number modulo two ($\mathbb{Z}_2$). The dimensionalities are written in the form (N+1)D, where N denotes the number of spatial dimensions.

symmetry class	$\mathcal{C}$	$\mathcal{P}$	$\mathcal{T}$	(0+1)D	(1+1)D	(2+1)D	(3+1)D
A				$\mathbb{Z}$		$\mathbb{Z}$	
AI			1	$\mathbb{Z}$			
AII			−1	$2\mathbb{Z}$		$\mathbb{Z}_2$	$\mathbb{Z}_2$
AIII	1				$\mathbb{Z}$		$\mathbb{Z}$
BDI	1	1	1	$\mathbb{Z}_2$	$\mathbb{Z}$		
C		−1				$2\mathbb{Z}$	
CI	1	−1	1				$2\mathbb{Z}$
CII	1	−1	−1		$2\mathbb{Z}$		$\mathbb{Z}_2$
D		1		$\mathbb{Z}_2$	$\mathbb{Z}_2$	$\mathbb{Z}$	
DIII	1	1	−1		$\mathbb{Z}_2$	$\mathbb{Z}_2$	$\mathbb{Z}$

other set. In terms of a mathematical formulation, chiral symmetry is a unitary operator for which

$$\mathcal{C}^{-1}\mathcal{H}\mathcal{C} = -\mathcal{H} \tag{1.53}$$

holds. Additionally, it should be noted that $\mathcal{C}^2 = 1$, $\mathcal{P}^2 = \pm 1$ and $\mathcal{T}^2 = \pm 1$ holds for these symmetries.

Based on these symmetries, a classification into ten symmetry classes can be made, which are shown in Table 1.1. These classes are often called Altland-Zirnbauer classes after their discoverers [73, 74]. Depending on the dimensionality of the system, the existence (or non-existence) of topological invariants for these systems was shown. This result is also sometimes called the periodic table of topological invariants. An empty entry in Table 1.1 implies no topological invariant, $\mathbb{Z}$ indicates an invariant that is a whole number, $2\mathbb{Z}$ one that is an even whole number and $\mathbb{Z}_2$ one that is a whole number modulo 2, i.e. an invariant that can assume two values only. While the question of existence has a fairly clear answer, the bigger and still unsolved challenge is the construction of such invariants for a given physical system in general. It does however give some insight into certain properties of systems belonging to one of these classes, as they

are less robust against perturbations breaking one of the symmetries that put them into their class. In the course of this work, this phenomenon will be encountered as well.

Finally, it is important to emphasise that the Altland-Zirnbauer classification as shown here only covers a subset of all possible Hamiltonians, namely static and Hermitian ones. In recent time, intense theoretical efforts have been dedicated to extending this classification to time-dependent Hamiltonians [75] as well as non-Hermitian ones [76].

2

Topology of magnetoinductive waves

Equipped with a formalism to describe magnetoinductive metamaterials as well as a degree of understanding of topology and some intuition of how it may be found in physics, the open problem until now used to be the link between the two.

The aim of this chapter is, for the first time, to establish and formalise a link between topological physics and magnetoinductive waves, to allow for the discussion and utilisation of topological physics in magnetoinductive metamaterials, forming the basis for the applications discussed in the ensuing chapters to be discussed in the framework of magnetoinductive wave theory, which is a well-established tool for the description of metamaterials. To make this connection, a formal mapping between the language of topological physics, typically in terms of Hamiltonians, and the language of magnetoinductive wave theory is required but, so far, was not available.

In the following, such a mapping is derived for the first time by showing that a suitable *analogon* of the Hamiltonian exists for magnetoinductive waves. Based on that, the topology of magnetoinductive waves is made accessible and discussed for the specific example of a diatomic magnetoinductive line, for which a topological invariant may be calculated explicitly. Further, it is shown how the topology of the diatomic magnetoinductive line results in observable consequences, namely the existence of topological edge states. These states are shown to exist in diatomic magnetoinductive lines and their properties are discussed and derived in detail.

The following chapter presents results that in parts were also published in Refs. [77], [78], [79] and [80].

2.1 Circuit Hamiltonian

Firstly, an *analogon* of a Hamiltonian is needed for magnetoinductive waves. Specifically, the aim is to find an eigenvalue problem for the eigenfrequencies of the system, which reads

$$\mathcal{H}\psi = F(\omega)\psi. \tag{2.1}$$

This problem mirrors the time-independent Schrödinger equation in Equation (1.42). Strictly speaking, $\mathcal{H}$ in Equation (2.1) is not necessarily a Hamiltonian, hence the terminology of calling it an *analogon* or, alternatively, a circuit Hamiltonian. The reason is that magnetoinductive waves theory is not a quantum theory. As such, it lacks a de Broglie relation that relates the energy of the system E to the frequency, as this is a consequence of particle-wave duality and hence a property of quantum systems only. Instead, the amplitude of the magnetoinductive wave determines the energy in the system and $F(\omega)$ is not related to the energy. Further, there is a "proper" Hamiltonian of the system which corresponds to its total energy, but it does not admit an eigenvalue problem for the eigenfrequencies of the system. Nonetheless, the behaviour of ψ as a wave is fully equivalent to a quantum wave function, meaning any effect that quantum mechanics predicts as a wave theory may also be observed for a classical system. Only if the particle-wave duality of quantum mechanics were essential or entanglement played a role, this equivalency would break down. In the course of this work, and throughout most of topological physics in fact, this is not needed and the equivalency holds.

In order to derive $\mathcal{H}$ for magnetoinductive waves, consider the generalised Kirchhoff's law of Equation (1.19) without an applied voltage

$$Z(\omega)\mathbf{I} = 0. \tag{2.2}$$

The vector of currents makes for a suitable choice of wave function, i.e.

$$\psi \equiv \mathbf{I}. \tag{2.3}$$

To find an eigenfrequency problem for the current, the frequency ω needs to isolated. Currently the frequency dependence of the system is contained in the impedances in the impedance matrix $Z(\omega)$. To isolate them, the explicit form of this dependence and hence the impedance matrix must be considered. Written out, it reads

$$Z(\omega) = \sum_{n=1}^{N} Z_0(\omega)\mathbf{e}_n \otimes \mathbf{e}_n + \frac{1}{2}\mathrm{j}\omega L \sum_{n\neq m}^{N}\sum_{m=1}^{N} \kappa_{n,m}\mathbf{e}_n \otimes \mathbf{e}_m, \tag{2.4}$$

where $\mathbf{e}_n \otimes \mathbf{e}_m$ denotes the outer product between two unit vectors $\mathbf{e}_n$ and $\mathbf{e}_m$, i.e. a matrix with a 1 in position (n, m) and 0 everywhere else. $\kappa_{n,m}$ denotes the coupling coefficient between the n^{th} element and the m^{th} element. Neglecting losses for the sake of simplicity, the self-impedance, which also depends on the frequency has the form

$$Z_0(\omega) = \frac{1}{\mathrm{j}\omega C} + \mathrm{j}\omega L. \tag{2.5}$$

Due to the different frequency dependencies of the terms for capacitance and inductance, the frequency cannot be isolated straight away. A multiplication of Equation (2.2) with $\mathrm{j}\omega C$ helps resolve that yielding

$$\left[\sum_{n=1}^{N}\left(1 - \frac{\omega^2}{\omega_0^2}\right)\mathbf{e}_n \otimes \mathbf{e}_n - \frac{1}{2}\frac{\omega^2}{\omega_0^2}\sum_{n\neq m}^{N}\sum_{m=1}^{N}\kappa_{n,m}\mathbf{e}_n \otimes \mathbf{e}_m\right]\mathbf{I} = 0. \tag{2.6}$$

where the resonant frequency of an individual element $\omega_0^2 = 1/LC$ was used. Sorting the terms by their frequency dependence then results in

$$\left[\sum_{n=1}^{N}\frac{\omega^2}{\omega_0^2}\mathbf{e}_n \otimes \mathbf{e}_n - \frac{1}{2}\frac{\omega^2}{\omega_0^2}\sum_{n\neq m}^{N}\sum_{m=1}^{N}\kappa_{n,m}\mathbf{e}_n \otimes \mathbf{e}_m\right]\mathbf{I} = \left[\sum_{n=1}^{N}\mathbf{e}_n \otimes \mathbf{e}_n\right]\mathbf{I}. \tag{2.7}$$

Noting that the right-hand side of this equation is equal to $\mathbf{I}$, division by the frequency yields

$$\left[\sum_{n=1}^{N}\mathbf{e}_n\otimes\mathbf{e}_n-\frac{1}{2}\sum_{n\neq m}^{N}\sum_{m=1}^{N}\kappa_{n,m}\mathbf{e}_n\otimes\mathbf{e}_m\right]\mathbf{I}=\frac{\omega_0^2}{\omega^2}\mathbf{I}, \tag{2.8}$$

which is in fact the desired eigenvalue problem for the eigenfrequencies of the system. Recalling Equation (2.1), the *analogon* of the Hamiltonian can thus be identified as

$$\mathcal{H}=\sum_{n=1}^{N}\mathbf{e}_n\otimes\mathbf{e}_n-\frac{1}{2}\sum_{n\neq m}^{N}\sum_{m=1}^{N}\kappa_{n,m}\mathbf{e}_n\otimes\mathbf{e}_m, \tag{2.9}$$

as well as

$$F(\omega)=\frac{\omega_0^2}{\omega^2}. \tag{2.10}$$

Note that this relation differs from the relation for electrons, where the de Broglie relation dictates $F(\omega)=E(\omega)=\hbar\omega$. The fact that $F(\omega)$ is different for electrons and magnetoinductive waves means that the dispersion relations of these two different types of wave are going to be different even when $\mathcal{H}$ is the same for both, but they are still connected by a continuous transformation. Hence, the topological properties of the system are not affected.

Comparing Equation (2.9) to the Hamiltonian of the tight-binding model in Equation (1.45), which written out reads

$$\mathcal{H}=\sum_{n=1}E_n\mathbf{e}_n\otimes\mathbf{e}_n+\sum_{n\neq m}^{N}\sum_{m=1}^{N}t_{n,m}\mathbf{e}_n\otimes\mathbf{e}_m \tag{2.11}$$

a mapping between the two can be found by identifying the on-site energies

$$E_n=1 \tag{2.12}$$

as well as the hopping strengths as

$$t_{n,m}=-\frac{1}{2}\kappa_{n,m}. \tag{2.13}$$

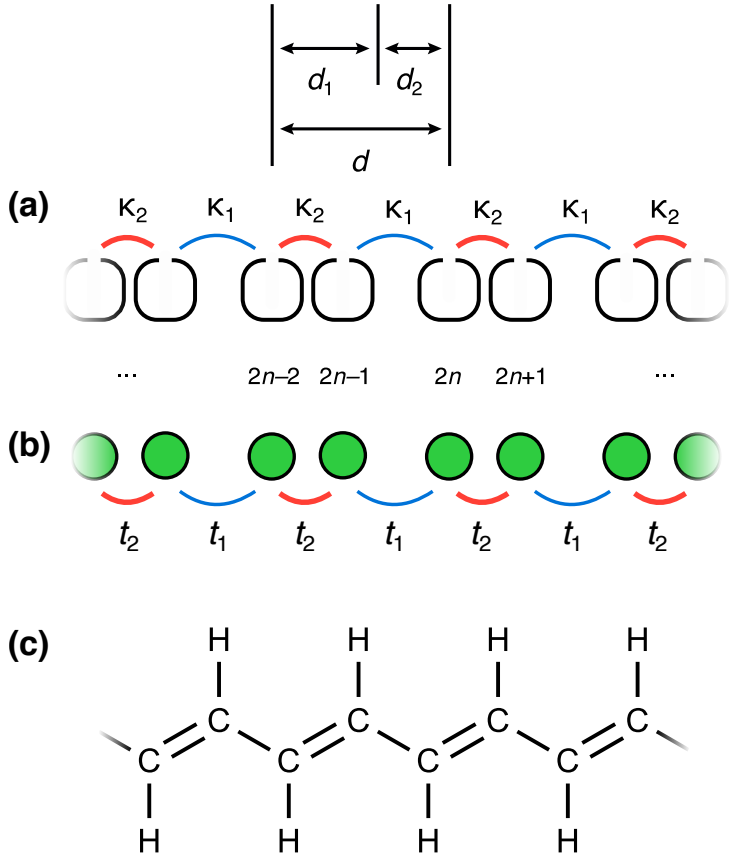


Fig. 2.1: Illustrations of diatomic models. **(a):** Diatomic magnetoinductive line with staggered coupling coefficients κ_1 and κ_2. **(b):** Diatomic tight-binding model with staggered hopping strengths t_1 and t_2. **(c):** The diatomic polymer polyacetylene, which was studied by Su, Schrieffer and Heeger [81].

Hence, magnetoinductive waves implement a tight-binding model with a distorted dispersion (or *vice versa*). Correspondingly, any (classical) result found for tight-binding models should also be valid for magnetoinductive waves.

2.2 Diatomic magnetoinductive lines

The least complex system supporting the propagation of magnetoinductive waves, the monoatomic line discussed in the previous section, while being an instructive example, is not topological. However, constructing a topological system by adding sublattices to the line and endowing it with chiral symmetry requires only a few modifications: The simplest model with sublattices is a diatomic chain. It may be created by using two

staggered nearest-neighbour couplings κ_1 and κ_2 in the system instead of just one, increasing the size of the unit cell to two elements. If it has only these two couplings, the system also has chiral symmetry as then each meta-atom is only coupled to meta-atoms on the other sublattice. In practice, this may be implemented through moving the elements around as the magnitude of the coupling changes with the spacing of the resonators.

Before moving to the topology of this system, it is instructive to gain an understanding for its wave physics by examining its dispersion, which was first derived by Sydoruk *et al.* [82]. To that end, the wave *ansatz* needs to be made to account for the now increased size of the unit cell. There are now two Bloch amplitudes, meaning the appropriate form of the solution for the currents according to the Bloch theorem must read

$$\begin{bmatrix} I_{2n-1} \\ I_{2n} \end{bmatrix} = \begin{bmatrix} Ae^{-\mathrm{j}kn(d_1+d_2)} \\ Be^{-\mathrm{j}kn(d_1+d_2)} \end{bmatrix}, \tag{2.14}$$

where d_1 and d_2 are the two spacings in the structure. An illustration of the diatomic magnetoinductive line is shown in Figure 2.1(a). Likewise, Kirchhoff's equations for the system must also be formulated separately for each atom in the unit cell, reading

$$\begin{aligned} Z_0 I_{2n-1} + \mathrm{j}\omega M_2 I_{2n-2} + \mathrm{j}\omega M_1 I_{2n} &= 0 \\ Z_0 I_{2n} + \mathrm{j}\omega M_1 I_{2n-1} + \mathrm{j}\omega M_2 I_{2n+1} &= 0. \end{aligned} \tag{2.15}$$

where $M_i = \kappa_i L/2$ are the two mutual inductances. Utilising the Bloch *ansatz* and inserting it into Equations (2.15) yields

$$\begin{aligned} Z_0 A + \mathrm{j}\omega M_2 B\mathrm{e}^{\mathrm{j}k(d_1+d_2)} + \mathrm{j}\omega M_1 B &= 0 \\ Z_0 B + \mathrm{j}\omega M_1 A + \mathrm{j}\omega M_2 A\mathrm{e}^{-\mathrm{j}k(d_1+d_2)} &= 0. \end{aligned} \tag{2.16}$$

Equations (2.16) are a system of equations for the Bloch amplitudes A and B. Correspondingly, it will only have a non-trivial solution if the determinant of the system

vanishes, which is the condition than can be used to find the dispersion relation for the waves. To extract it, said determinant is calculated to be

$$-\omega^2 \left(M_1 + M_2 \mathrm{e}^{-\mathrm{j}k(d_1+d_2)}\right)\left(M_1 + M_2 \mathrm{e}^{\mathrm{j}k(d_1+d_2)}\right) = Z_0^2. \tag{2.17}$$

After some algebra, denoting $d = d_1 + d_2$, Equation 2.17 may be solved for the wave number k as

$$\cos kd = \frac{-Z_0^2 - \omega^2(M_1^2 + M_2^2)}{2\omega^2 M_1 M_2}. \tag{2.18}$$

Additionally, solutions for the Bloch amplitudes A and B may also be determined by solving the system of Equations (2.16). Their ratio reads

$$\frac{B}{A} = -\frac{1}{2}\frac{\kappa_1 + \kappa_2 e^{-\mathrm{j}kd}}{1 - \dfrac{\omega_0^2}{\omega^2} - \dfrac{\mathrm{j}}{Q}\dfrac{\omega_0}{\omega}}. \tag{2.19}$$

Using Equations (2.18) and (2.19), it is possible to get a look at the qualitative behaviour of magnetoinductive waves on an (infinite) diatomic line, Figure 2.2 shows the dispersion for realistic example parameters in both the lossless and the lossy case with a quality factor of $Q = 250$. Firstly, turning to Figure 2.2(a), which displays the real and imaginary part of the wave number, it is clear that the diatomic line has two bands. Around the resonant frequency of the single element ω_0, the wave number turns complex and the waves are attenuated. This frequency range is called the bandgap or the (central) stopband. The edges of the passbands may be found by examining Equation (2.18) in the lossless case and determining where the right-hand side equals ±1, i.e. where the cosine turns complex. For the bottom edge of the lower passband and for the top edge of the upper passband at $kd = 0$, this results in

$$\frac{\omega}{\omega_0} = \sqrt{1 \pm \frac{|\kappa_1 + \kappa_2|}{2}}, \tag{2.20}$$

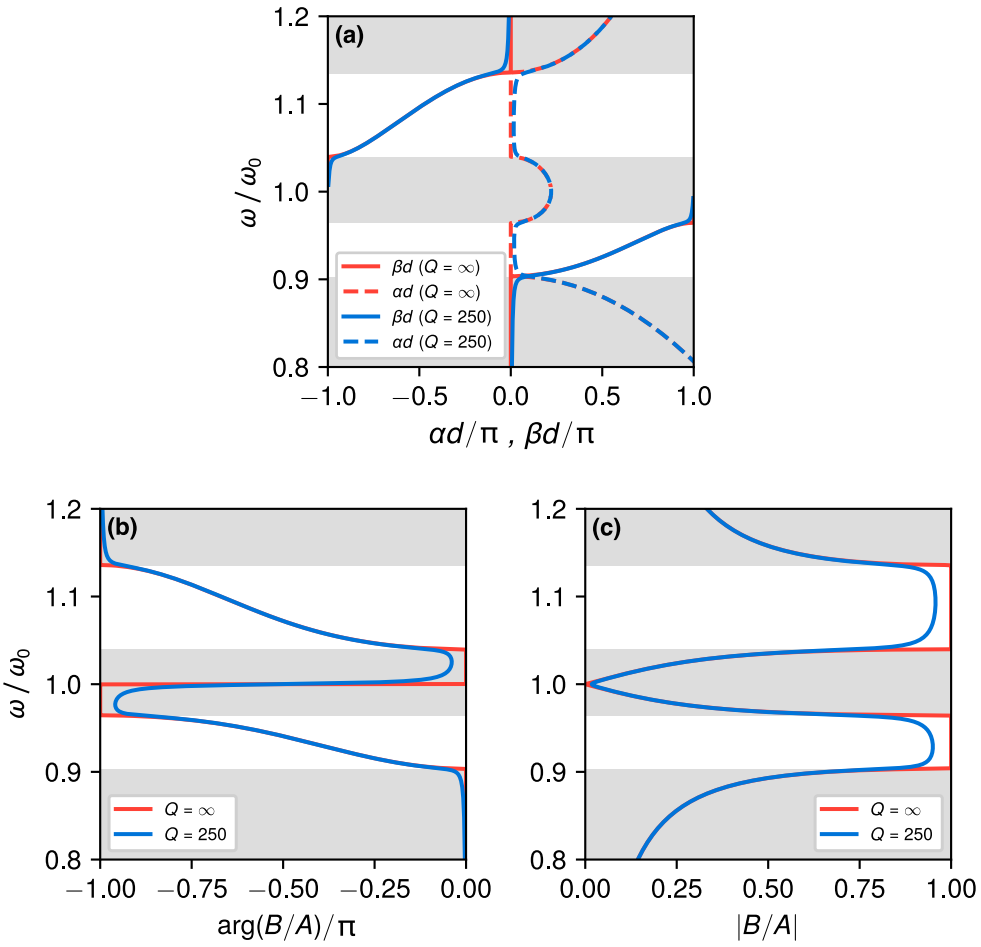


Fig. 2.2: Dispersion characteristics of an infinite diatomic magnetoinductive line, here with $\kappa_1 = 0.15$ and $\kappa_2 = 0.3$ for lossless and lossy ($Q = 250$) case. The frequency ranges shaded in grey indicate the stopbands. **(a):** Dispersion diagram for the real part β and imaginary part α of the wave number k. **(b):** Phase ratio between neighbouring sites $\arg(B/A)$. **(c):** Amplitude ratio between neighbouring sites $|B/A|$.

whereas for the top edge of the lower passband and for the bottom edge of the upper passband at $kd = \pi$, it yields

$$\frac{\omega}{\omega_0} = \sqrt{1 \pm \frac{|\kappa_1 - \kappa_2|}{2}}. \tag{2.21}$$

Correspondingly, the size of the bandgap is determined by the difference of the two couplings. As expected, in the case $\kappa_1 = \kappa_2$, the bandgap closes, merging the two passbands into a single one and reducing the system to the monoatomic case. Note that these statements are true for the lossless case only. In the lossy case, as also shown in Figure 2.2(a), the transitions around the edges of the bands become less sharp, with

propagation allowed even outside of what are the passbands in the lossless case. Crucially though, in the case shown here, the waves are strongly attenuated such that the bands are still very well defined. Lastly, it can be seen that the lower branch of the dispersion is a forward wave whereas the upper branch is a backward wave.

2.3 Topology of diatomic magnetoinductive lines

2.3.1 Bloch Hamiltonian

In order to simplify the identification of a topological invariant, it is most often the easiest way to consider the system in reciprocal space, i.e. to treat the Bloch Hamiltonian instead of the Hamiltonian. As such, this subsection is dedicated to the presentation of results on deriving the (circuit) Bloch Hamiltonian of a diatomic magnetoinductive line. In a first step, the circuit Hamiltonian in Equation (2.9) may be simplified by only considering nearest-neighbour couplings. It then reads

$$\mathcal{H} = \sum_{n=-\infty}^{\infty} \mathbf{e}_n \otimes \mathbf{e}_n - \frac{1}{2} \sum_{n=-\infty}^{\infty} \kappa_{n,n+1} (\mathbf{e}_n \otimes \mathbf{e}_{n+1} + \mathbf{e}_{n+1} \otimes \mathbf{e}_n), \tag{2.22}$$

meaning it is now a tridiagonal matrix of infinite size (for an infinite line). The $\kappa_{n,m}$ are just the two couplings κ_1 and κ_2 introduced above, leading to the full expression for the circuit Hamiltonian of the diatomic line in the following form:

$$\mathcal{H} = \sum_{n=-\infty}^{\infty} \mathbf{e}_n \otimes \mathbf{e}_n - \frac{1}{2} \sum_{n=-\infty}^{\infty} \kappa_1 (\mathbf{e}_{2n-1} \otimes \mathbf{e}_{2n} + \mathbf{e}_{2n} \otimes \mathbf{e}_{2n-1}) + \kappa_2 (\mathbf{e}_{2n} \otimes \mathbf{e}_{2n+1} + \mathbf{e}_{2n+1} \otimes \mathbf{e}_{2n}). \tag{2.23}$$

Further, recalling the Bloch *ansatz* made in the previous section reading

$$\mathbf{I} = (\dots, A\mathrm{e}^{-\mathrm{j}kd(n-1)}, B\mathrm{e}^{-\mathrm{j}kd(n-1)}, A\mathrm{e}^{-\mathrm{j}kdn}, B\mathrm{e}^{-\mathrm{j}kdn}, A\mathrm{e}^{-\mathrm{j}kd(n+1)}, B\mathrm{e}^{-\mathrm{j}kd(n+1)}, \dots), \tag{2.24}$$

reveals a large amount of redundancy in the Schrödinger equation (2.1). Specifically, as mentioned previously, the number of independent variables and thus the dimensionality of the system is reduced to the number of Bloch amplitudes, hence here to two. The equations for the n^{th} unit cell have the form

$$\begin{bmatrix} 1 & -\frac{\kappa_1}{2} - \frac{\kappa_2}{2}\mathrm{e}^{\mathrm{j}kd} \\ -\frac{\kappa_1}{2} - \frac{\kappa_2}{2}\mathrm{e}^{-\mathrm{j}kd} & 1 \end{bmatrix} \begin{bmatrix} A \\ B \end{bmatrix} \mathrm{e}^{-\mathrm{j}kd} = \frac{\omega_0^2}{\omega^2} \begin{bmatrix} A \\ B \end{bmatrix} \mathrm{e}^{-\mathrm{j}kd}. \tag{2.25}$$

As Equation (2.25) is just an eigenfrequency problem for the Bloch amplitudes, the Bloch Hamiltonian can directly be identified as

$$\mathcal{H}(k) = \begin{bmatrix} 1 & -\frac{\kappa_1}{2} - \frac{\kappa_2}{2}\mathrm{e}^{\mathrm{j}kd} \\ -\frac{\kappa_1}{2} - \frac{\kappa_2}{2}\mathrm{e}^{-\mathrm{j}kd} & 1 \end{bmatrix}. \tag{2.26}$$

A form of the Bloch Hamiltonian that is more amenable to the following analysis is if it is written in terms of Pauli matrices [83], i.e.

$$\mathcal{H}(k) = \sigma_0 - \frac{1}{2}\left[\kappa_1 + \kappa_2 \cos(kd)\right]\sigma_x - \frac{1}{2}\kappa_2 \sin(kd)\sigma_y, \tag{2.27}$$

where

$$\sigma_0 = \begin{bmatrix} 1 & 0 \\ 0 & 1 \end{bmatrix} \tag{2.28}$$

is the identity matrix and

$$\sigma_x = \begin{bmatrix} 0 & 1 \\ 1 & 0 \end{bmatrix} \text{ and } \sigma_y = \begin{bmatrix} 0 & \mathrm{j} \\ -\mathrm{j} & 0 \end{bmatrix} \tag{2.29}$$

are Pauli matrices.

2.3.2 Topological invariant

Based on the Bloch Hamiltonian just derived, it is now possible to identify a topological invariant for magnetoinductive waves to understand their topology. In fact, the topological invariant of the system under discussion here is precisely the one mentioned in the previous chapter: a winding number. While here the model is considered with magnetoinductive waves in mind, the first application and identification of the winding number was due to a study of polyacetylene [81], a molecule with a similarly staggered structure as the diatomic magnetoinductive line. It is shown in Figure 2.1(c). Hence, models like this are often broadly referred to as Su-Schrieffer-Heeger (SSH) models, named after the authors of the 1979 study on polyacetylene that ultimately led to the discovery of this topological model.

To identify the topological invariant of the diatomic magnetoinductive line, one may first rewrite the Bloch Hamiltonian with a vector of Pauli matrices $\boldsymbol{\sigma} = (\sigma_x, \sigma_y)$.

$$\mathcal{H}(k) = \sigma_0 - \frac{1}{2}\boldsymbol{\sigma} \cdot \mathbf{n}, \tag{2.30}$$

where

$$\mathbf{n} = \begin{bmatrix} \kappa_1 + \kappa_2 \cos(kd) \\ \kappa_2 \sin(kd) \end{bmatrix} \tag{2.31}$$

The keen eye will already notice that this vector looks a lot like the parametrisation of a curve, if kd is taken as the curve parameter. Hence, looking for a winding number is the natural next step. Before calculating the winding number, a brief look at a few illustrative cases is helpful. In Figure 2.3, the curve defined by $\mathbf{n}$ is shown for three distinct cases. On the left, where $0.15 = \kappa_1 < \kappa_2 = 0.3$, the winding number with respect to the origin as reference point is $w = 1$. On the other hand, with inverted couplings of $0.3 = \kappa_1 < \kappa_2 = 0.15$, the winding number becomes zero. The transition point happens at $\kappa_1 = \kappa_2$, where the winding number is ill-defined as the curve contains the reference point. Thus, the winding number is not defined in the monoatomic case.

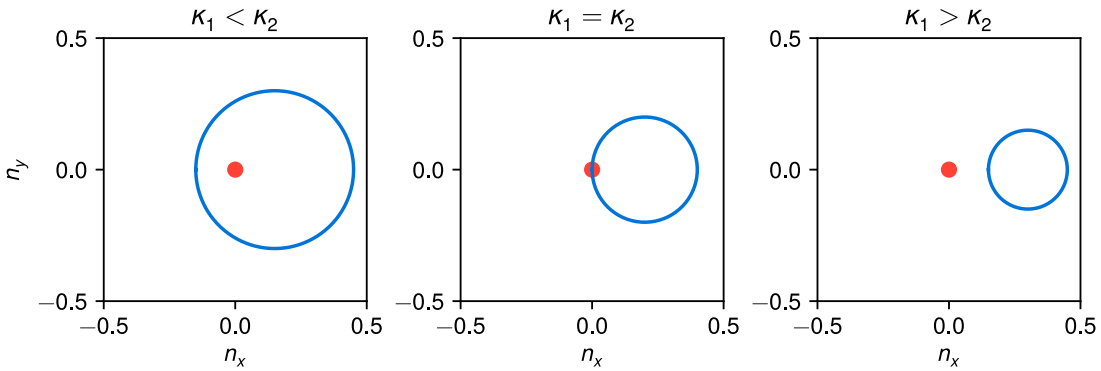


Fig. 2.3: The topological invariant for the diatomic chain is a winding number determined from the Bloch Hamiltonian. Shown here are three distinct cases. On the left, where $0.15 = \kappa_1 < \kappa_2 = 0.3$, the winding number with respect to the origin is $w = 1$. In the middle ($\kappa_1 = 0.2 = \kappa_2$) corresponding to a monoatomic chain shows that when the passbands merge into one, the winding is ill-defined as the curve passes the origin. On the right, where $0.3 = \kappa_1 > \kappa_2 = 0.15$, the winding number is $w = 0$.

In order to calculate the winding number, it is helpful to consider the coordinates of the curve as real and imaginary part of a complex number, i.e.

$$\gamma(kd) = n_x + \mathrm{j}n_y = \kappa_1 + \kappa_2 \cos(kd) + \mathrm{j}\kappa_2 \sin(kd) = \kappa_1 + \kappa_2 \mathrm{e}^{\mathrm{j}kd}. \tag{2.32}$$

The winding number of this curve may now be calculated using Equation (1.37), in this case reading

$$w = \frac{d}{2\pi\mathrm{j}} \int_{-\pi/d}^{\pi/d} \frac{\mathrm{d}}{\mathrm{d}k} \ln \gamma(kd)\, \mathrm{d}k. \tag{2.33}$$

Inserting the formula for the parametrisation of the curve yields

$$w = \frac{d}{2\pi\mathrm{j}} \int_{-\pi/d}^{\pi/d} \frac{\kappa_2 \mathrm{e}^{\mathrm{j}kd}}{\kappa_1 + \kappa_2 \mathrm{e}^{\mathrm{j}kd}}\, \mathrm{d}k = \begin{cases} 1, & |\kappa_2| > |\kappa_1| \\ 0, & |\kappa_1| > |\kappa_2| \end{cases}, \tag{2.34}$$

which confirms the observations made based on the illustration in Figure 2.3.

Overall, this confirms that diatomic magnetoinductive lines have a winding number as their topological invariant which is determined by their coupling ratio which groups them into two homotopy classes. Additionally, the transition point (where the topological invariant is ill-defined) coincides with the vanishing of the bandgap, im-

plying that the circuit Hamiltonians of diatomic magnetoinductive lines with different topological invariants cannot be continuously transformed into each other without the bandgap closing. In the following section, it will be shown that this results in clear physical effects caused by the topology of this system.

2.4 Topological edge states

All considerations so far have been made for lines with a continuously defined wave number and hence infinite length, leading to an at least superficially paradoxical question: Since the winding number depends on which coupling is greater but for an infinite line, there is no meaningful rule prohibiting a simple shift of the unit cell by one element and thus swapping the two couplings. Continuing this line of thought, this means that for the infinite line just considered the topological invariant is inconsequential with regards to the physics of the system. A quick look at the dispersion relation of the diatomic line in Equation (2.18), which is also derived for the infinite line confirms this: It is also invariant under swaps of the two mutual inductances. Hence, there is only one remaining option when looking for physical signatures of the topology of the line, namely moving from infinite lines to finite ones. While in that case, at the boundaries of the line the choice of unit cell becomes meaningful, it is not immediately obvious why the topological invariant, which is only defined for the infinite system, should in any way be relevant to the finite line. Indeed, this result is a highly nontrivial one known as the bulk-edge correspondence [84]. The detailed proof is rather lengthy and hence not shown here, but the bulk-edge correspondence is a general rule for topological systems which rigorously shows that the topological properties of the (infinite) bulk of the system remain meaningful at the edge where the system is truncated.

Such a relation between the topology of the system in the bulk, where it remains physically inconsequential, and at the edge, calls for an investigation of the behaviour with an edge. As the coupling ratio κ_2/κ_1 shows where the topological invariant and

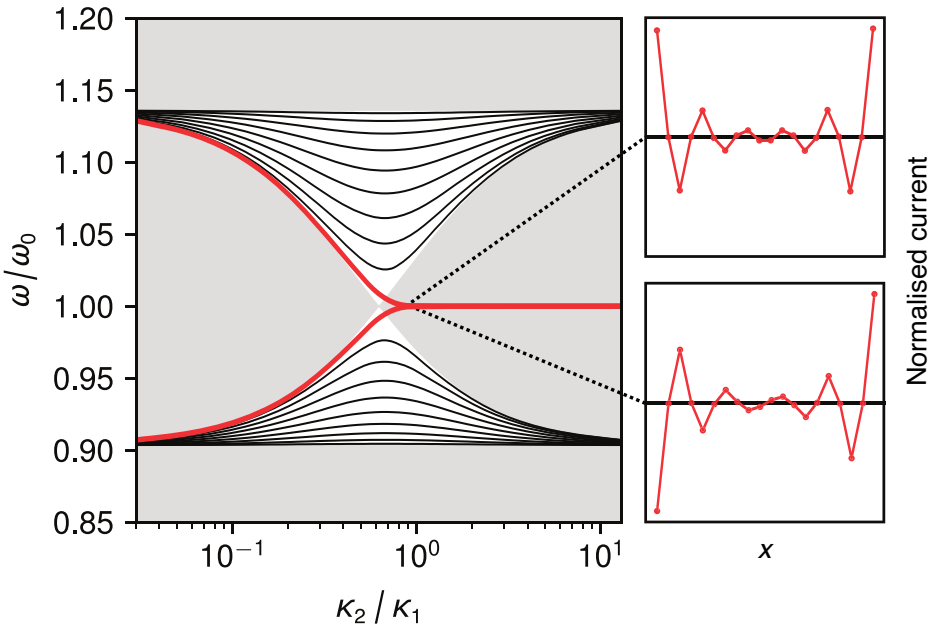


Fig. 2.4: Resonances of a diatomic magnetoinductive line with $N = 20$ and varying coupling ratio κ_2/κ_1. For $\kappa_2/\kappa_1 > 1$ the system acquires a non-zero winding number and thus enters the topological phase. This causes two of the resonances to move into the centre of the stopband, which is indicated by the grey shading. These so-called topological edge states are resonances localised at the edges of the line, decaying into the bulk, as shown on the right. The insets show the current distribution along the line for the case $\kappa_2/\kappa_1 = 2$.

thus the topological phase changes, the simplest way to spot topology-related behaviour is to look for changes in any properties of the system as the invariant changes by sweeping over κ_2/κ_1. In Figure 2.4, the resonances of a diatomic magnetoinductive line are shown. As expected, there are a multitude of resonances confined to the two passbands of the line, with the passbands narrowing as the structure becomes more strongly dimerised, i.e. the two coupling coefficients become more and more different. However, there are two resonances (highlighted in red) that behave very differently to the others. Starting out as resonances inside the passband for $\kappa_1 > \kappa_2$ (where the winding number is zero), as the winding number changes they merge and from then on reside stably around the resonant frequency of a single element. Remarkably, for the diatomic line that frequency is also the centre of the bandgap, meaning that counter the expectation rearing from the dispersion of the infinite line, there are resonances inside the bandgap, which further only occur when the winding number is nonzero. The two

modes become arbitrarily close in frequency to each other with increasing coupling ratio and increasing length of the chain, though they never fully merge. The reason for this small frequency split will be discussed in more detail later in this section. However, even for modest couplings ratios such as the one used here, the difference in resonant frequency for the modes is less than 0.1% of the resonant frequency of a single element, so identical for almost all practical purposes due to the finite resonance linewidth introduced by any losses. Looking at the current profile of the modes shown in the insets of Figure 2.4, they exhibit strongly localised high amplitudes on the (weakly coupled) edge elements, decaying away from these. Due to the symmetry of the line, there are two of them, one symmetric and one antisymmetric resonance. Due to their characteristic localisation on the edge of the system and their physical origin these resonances are called topological edge states, a term first introduced in the context of the quantum Hall effect [85].

To understand how topology causes these resonances to occur, it is instructive to consider what happens to the bands in a simplified model with a topological invariant. Topological edge states occur at interfaces between systems with different topological invariants. Note that such an interface may also be an edge, which can be considered an interface with vacuum. Where a system has a topological invariant of zero and thus no edge states at its open boundaries, it is called topologically trivial [1]. Conversely, all other systems are called topologically non-trivial. To understand why topological edge states must occur, interfaces between combinations of topologically trivial and non-trivial media, as illustrated in Figure 2.5, need to be considered. The corresponding bands of the systems are sketched along the spatial dimension x. First, considering an interface between two topologically trivial systems (on the left of Figure 2.5), the two bands separated by a stopband approach the interface, but while there may be some distortion the two bands may smoothly transform into each other as the winding number does not change across the interface. However, the second case (on the right of Figure 2.5), where a topologically trivial system interfaces with one that is topologically non-

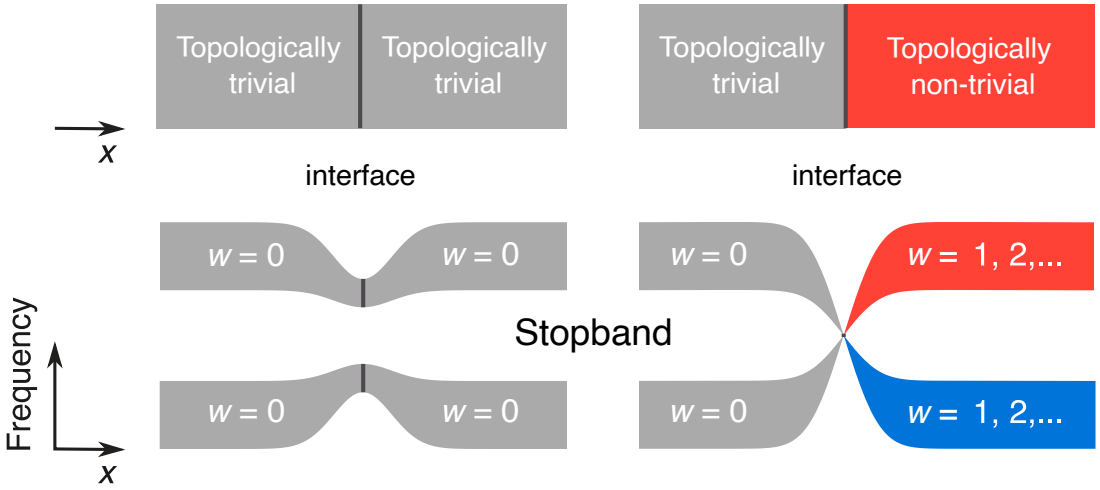


Fig. 2.5: Topology has a significant influence on the bands at the interface with other systems: While smooth transitions between systems with identical topological invariants are possible, at interfaces between systems with different topological invariants, such as topologically trivial and topologically non-trivial systems, the change of the topological invariant requires the bandgap to close.

trivial, is different: Recalling the conclusion of the previous section, the Hamiltonian of a system cannot be continuously transformed into one with a different topological invariant without a closing of the bandgap. Hence, the only possible solution is that at an interface of two systems with different topological invariants, the bandgap must close at the interface to allow for the transition from one topological invariant to the other. Correspondingly, at the interface, resonances occur at frequencies that in the bulk would be inside the stopband. These are the topological edge states also seen in Figure 2.4, where at the edge crossing into vacuum the bandgap had to close. Topological edge states are a general hallmark of topological systems [1]. They have been observed in a variety of systems, such as ones with higher dimensionality [5], with periodic driving [86] or with gain and loss [87]. Nevertheless, even though the aforementioned systems have other topological invariants than the one here, the mechanism giving rise to the topological edge states is the same. Additionally, and perhaps a prime reason why topological edge states are of such interest technologically as well, is their robustness. Recalling Section 1.4, whether a system has a topological invariant is determined by its symmetries. If an external perturbation does not break these symmetries globally or cause the bandgap

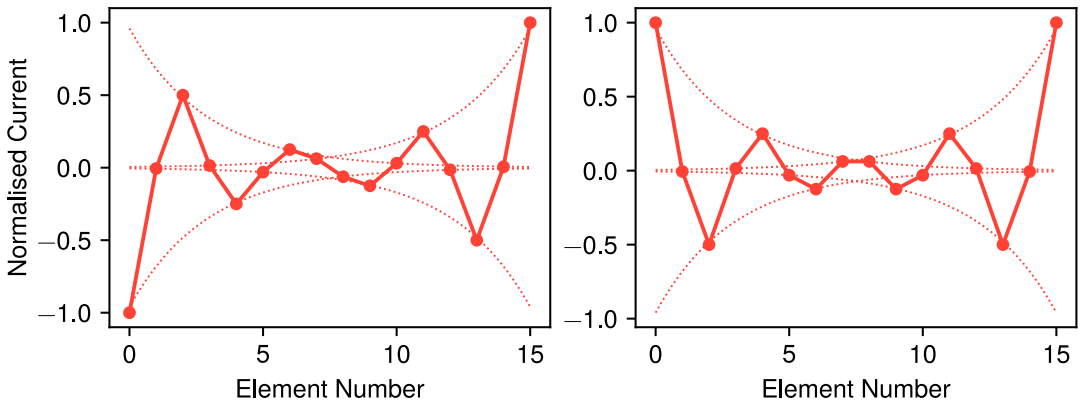


Fig. 2.6: Example of the two edge states and their shape for $\kappa_1 = 0.15$ and $\kappa_2 = 0.3$. There are two edge states, a symmetric and an antisymmetric one at $\omega \approx 0.995\omega_0$ and $\omega \approx 1.001\omega_0$, respectively. Their decay into the bulk is accurately described by an exponential law, shown by the dotted lines.

to close, the topological invariant remains unchanged and the topological edge state persists [1]. However, if any symmetries of the system are broken such that the system changes to a symmetry class that lacks a topological invariant or if the perturbations are so large that the bandgap closes and thus the invariant becomes ill-defined, the existence of the topological edge state is not mandated anymore. Otherwise, topological protection makes edge states robust against perturbations of the system [8].

In terms of some more detailed analysis of magnetoinductive topological edge states, Figure 2.6 shows the edge states of a diatomic chain with eight elements for example couplings of $\kappa_1 = 0.15$ and $\kappa_2 = 0.3$. The decay of the edge states into the bulk, as indicated by the dotted lines in Figure 2.6, follows an exponential law. There is a decay away from both edges. The asymmetric mode localised on each edge overlaps with the mode on the other edge. Hence, they hybridise [63], forming the antisymmetric and symmetric mode profiles seen here. The frequency split between these two modes mentioned earlier is caused by the hybridisation and its magnitude is increases with the amount of overlap, which reduces with increasing coupling ratio and chain length.

The decay rate of the edge states can be determined analytically (at least to a very good approximation). To this end, consider the dispersion in Equation (2.18) at the

centre of the stopband (i.e. $\omega = \omega_0$) in the lossless case (i.e. $Q = \infty$). In that case, $Z_0 = 0$ and Equation (2.18) may hence be simplified to read

$$\cos(kd) = -\frac{\kappa_1^2 + \kappa_2^2}{2\kappa_1\kappa_2}. \tag{2.35}$$

Splitting the wave number into the propagation and attenuation constant $k = \beta - \mathrm{j}\alpha$ means that the previous equation can also be written as

$$\cos(\beta d)\cosh(\alpha d) + \mathrm{j}\sin(\beta d)\sinh(\alpha d) = -\frac{\kappa_1^2 + \kappa_2^2}{2\kappa_1\kappa_2}. \tag{2.36}$$

As the coupling constants are assumed to be real in the context of this work,

$$\sin(\beta d)\sinh(\alpha d) = 0 \tag{2.37}$$

must hold. Equation (2.37) has only two possible solutions, either $\alpha = 0$ or $\beta = p\pi$ with $p \in \mathbb{Z}$. The solution $\alpha = 0$ can be excluded, which may be seen by considering Equation (2.36) under the assumption that $\alpha = 0$, leading to

$$\cos(\beta d) = -\frac{\kappa_1^2 + \kappa_2^2}{2\kappa_1\kappa_2}. \tag{2.38}$$

Examining the right-hand side of Equation (2.38), it can be seen that as $\kappa_1^2 + \kappa_2^2 \geq 2|\kappa_1\kappa_2|$ holds for all κ_1 and κ_2, the absolute value of this term is always equal or greater than 1. However, it follows that β is not real, which constitutes a contradiction to the initial assumption that it is the real part of k. Hence, $\beta = p\pi$ with $p \in \mathbb{Z}$ is the only remaining solution. The signs of κ_1 and κ_2 determine whether p needs to be even or odd, with p being odd when $\kappa_1\kappa_2 > 0$ and even otherwise. Then, Equation (2.36) takes the form

$$\cosh(\alpha d) = \frac{\kappa_1^2 + \kappa_2^2}{2\kappa_1\kappa_2}, \tag{2.39}$$

which in turn can be rewritten as

$$e^{\alpha d} + e^{-\alpha d} = \frac{\kappa_1}{\kappa_2} + \frac{\kappa_2}{\kappa_1}. \tag{2.40}$$

Since $\alpha > 0$, it follows from the previous equation (for $|\kappa_2| > |\kappa_1|$) that

$$e^{-\alpha d} = \frac{\kappa_1}{\kappa_2}, \tag{2.41}$$

a relationship that describes the decay behaviour of topological edge states in diatomic magnetoinductive lines. An exponential decay of the form shown in Equation (2.41), taken to point away from the boundary and into the bulk, is used to plot the dotted lines in Figure 2.6. A very good match with the numerically calculated eigenmode profiles can be observed. The topological edge states thus follow the profile of evanescent waves, which is also governed by the attenuation coefficient inside the stopband. In effect, these topological edge states could be considered "evanescent standing waves" that may occur only because the topology of the system mandates the existence of resonances inside the bandgap.

2.5 Conclusions

In this chapter, a formal connection between quantum and magnetoinductive wave theory was newly developed and topology of magnetoinductive waves was investigated for the first time. To this end, a mapping was constructed mathematically bridging magnetoinductive wave theory and the language of quantum theory by introducing a circuit Hamiltonian, the eigenvalues and eigenvectors of which are the eigenfrequencies and current eigenvectors of the magnetoinductive metamaterial, respectively. This fact is in analogy to the time-independent Schrödinger equation for the quantum mechanical Hamiltonian.

Due to the formal equivalency between tight binding models and magnetoinductive waveguides with nearest-neighbour coupling that was shown with the help of the circuit Hamiltonian, this mapping allowed for the study of the topology of diatomic magnetoinductive waveguides based on the established theory of the Su-Schrieffer-Heeger model. The Bloch Hamiltonian of the magnetoinductive line was constructed and used to derive the winding number as the topological invariant of the system. Based on this, the occurrence of topological edge states residing at the centre of the stopband of the line was shown and their mode profile was analysed using the dispersion of magnetoinductive waves in diatomic lines.

3 Topological wireless power transfer

With the topology of magnetoinductive lines formalised and the physics arising from it understood, the next question to ask is the one of applications. Magnetoinductive metamaterials were found to be of use in various ways since their conception, but one application particularly springs to mind: wireless power transfer.

For wireless power transfer, a magnetoinductive line is excited on one edge, typically by a voltage of constant amplitude applied to the resonator, and then the line is loaded with a load impedance on the opposite edge, representing a receiver of power in circuit theory [44], as illustrated in Figure 3.1. Consequently, for efficient wireless power transfer, it is desirable to have a high current amplitude on the loaded element to maximise the delivery of power, which is precisely what a topological edge state does. Nonetheless, from a point of view of conventional wave theory, it appears rather strange to attempt transferring power at a frequency which lies in the centre of the stopband. After all, as its name already suggests, little to no power may typically pass through the system in the stopband.

In this chapter, it is shown for the first time that despite going against common intuition, wireless power transfer may indeed occur efficiently in the stopband of diatomic magnetoinductive lines by harnessing their topological edge states. Moreover, due to the unique properties of the edge states such as their characteristic current profile and their inherent robustness against external perturbations, such a topological wireless power transfer holds several advantages over the conventional approach using propagating waves in the passband.

Part of the work presented in this chapter was published in Refs. [77] and [78].

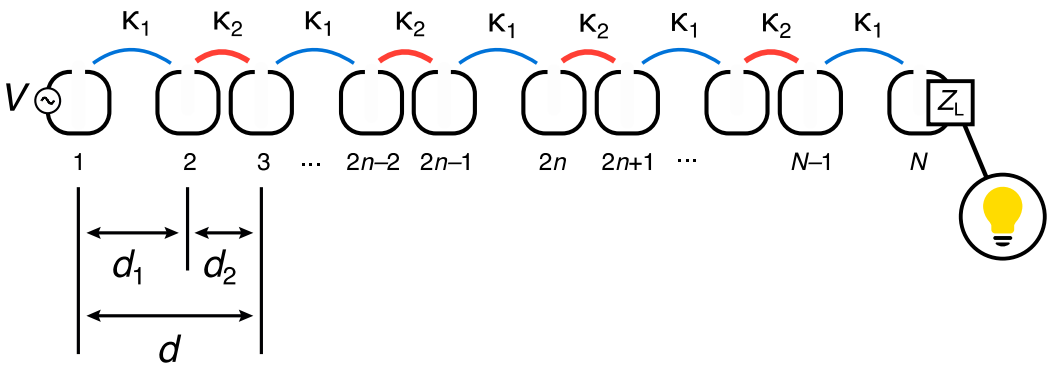


Fig. 3.1: Sketch of a wireless power transfer system based on a diatomic magnetoinductive line with coupling coefficients κ_1 and κ_2. The source of a voltage V excites the chain with N elements on one edge. The power delivered to the other edge is dissipated by a load impedance Z_L, which is the circuit theory representation of the power-receiving device.

3.1 Wireless power transfer: Introduction

Before getting into the discussion and analysis of harnessing the topology of magnetoinductive lines for wireless power transfer, this section shall start with a brief introduction to wireless power transfer to put the work presented here into the relevant context.

There are two classes of wireless power transfer mechanisms: radiative and non-radiative ones [88]. The former aims to harness the power carried by electromagnetic waves propagating through free space, whereas the latter is focused on using the non-propagating near field. This work, due to its reliance on near-field magnetic coupling as the mechanism concerns itself with non-radiative power transfer. Historically, the first attempts at wireless power transfer are typically attributed to Nikola Tesla, who towards the end of the 19$^{\text{th}}$ century worked on using high-voltage transformers, nowadays often called Tesla coils, to transfer power non-radiatively [92], as shown in Figure 3.2(a). The vision at the time was to rid power transmission of the use of wires entirely. While some progress was made towards such a goal, including the demonstration of wireless transfer of power over short distances, the filing of several patents relating to

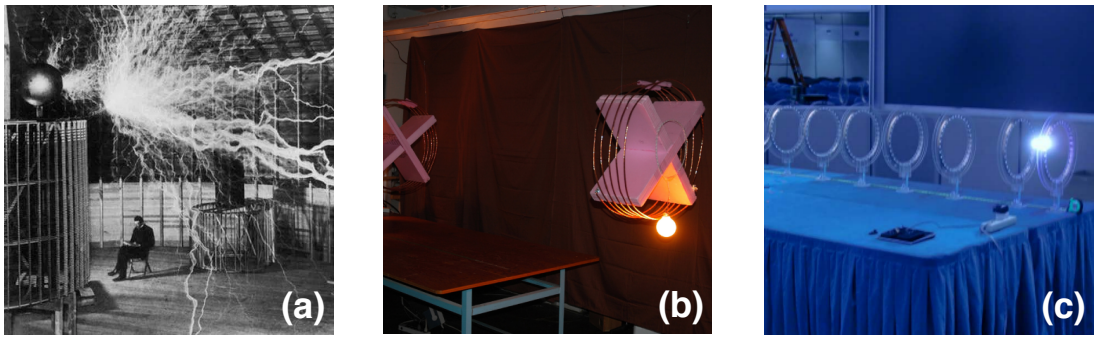


Fig. 3.2: **(a):** Nikola Tesla in his laboratory in Colorado Springs, where he researched wireless power transfer, in 1899 (adapted from [89]). **(b):** In 2007, Kurs *et al.* [90] demonstrated efficient non-radiative wireless power transfer in the midrange through magnetically coupled resonances (adapted from [90]). **(c):** Extending the system into a magnetoinductive waveguide by using relay resonators extends the power transfer range significantly (adapted from [91]).

this [93–95] and even the construction of an experimental transmission station called the Wardenclyffe plant [96], the project was ultimately abandoned, not least because both the feasibility and the safety of the approach was in question. Recently however, wireless power transfer has had somewhat of a renaissance, especially in the mid- and short range, where the scale of the transmission apparatus is not much smaller than the transfer distance. In 2007, it was shown by Kurs *et al.* [90] that two resonant coils coupled through magnetic induction provide a way of transferring power wirelessly in the midrange far more efficiently than non-resonant systems. An image of the system used to achieve this is shown in Figure 3.2(b). At the same time, the rapid advances in the field of metamaterials allowed for this concept to be picked up and developed quickly, leading to the realisation that the addition of further resonators as relay elements - i.e. using a magnetoinductive waveguide to transfer power wirelessly - allows for a significantly extended transfer distance [91], an example of which is shown in Figure 3.2(c). On top of that, the utilisation of a magnetoinductive metamaterial opens up entirely new avenues in the design of wireless power transfer systems [44], allowing for the engineering of the bands of the magnetoinductive line, the implementation of elements such as directional couplers or splitters [48], or the extension of the dimensionality

of the metamaterial beyond one spatial dimension [46]. Finally, lately significant advances in the control and shaping of fields and resonances have spawned a variety of advanced approaches to wireless power transfer [97]. This includes recent works on nonlinear parity-time symmetric circuits [98], bound states in the continuum [99], as well as the work shown here and ones that followed it [100–102].

Note that in this section, values of $\omega_0 = 2\pi \times 10^9$ rad/s for the resonant frequency of a single element, $L = 20$ nF, $\kappa_1 = 0.15$ and $\kappa_2 = 0.3$ for the coupling coefficients are used for the purpose any illustration of the results.

3.2 Asymmetric topological edge states

As noted in Section 3.1, the unique feature of topological edge states to exhibit a high amplitude localised on the edge of the magnetoinductive line where the load impedance is placed appears to be useful for delivering power to it. However, for the typical topological edge state, there is also a high amplitude localised on the opposite edge of the system, where the excitation is applied. This appears problematic, as due to the high amplitude and ohmic losses power would be dissipated at this location before it even has a chance to arrive at the loaded element. Ideally, the current distribution should be asymmetric with a high amplitude only on the edge where the load is located, with a profile looking like a growing evanescent wave. This section is dedicated to discussing two complimentary approaches of how that objective may be achieved and how an asymmetric "growing" edge state may be engineered.

3.2.1 Asymmetry through superposition

To engineer an asymmetric edge state, one possible approach is to rely on the symmetry properties of the symmetric and the antisymmetric topological edge state: As shown in Figure 3.3, the sum and the difference of these states lead to an asymmetric

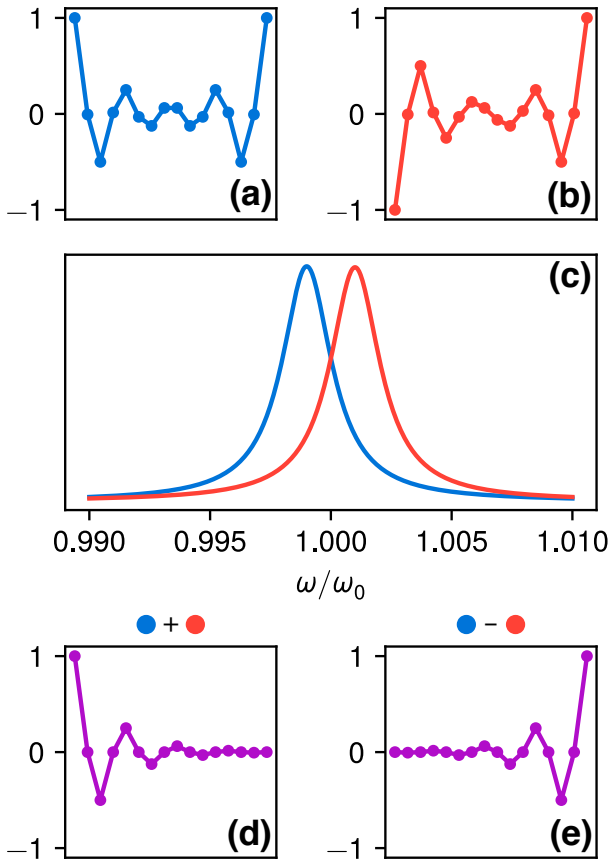


Fig. 3.3: The superposition of the symmetric and antisymmetric topological edge state shown in **(a)** and **(b)**, results in asymmetric shapes with a decaying and growing profile shown in **(d)** and **(e)**. These are not eigenmodes of the system, but may be excited at ω_0 due to the finite linewidth of the edge states in lossy systems causing the resonances to spectrally overlap, as sketched here in **(c)**.

cancellation of the amplitude, resulting in the desired current distribution along the structure, either with a decaying or with a growing amplitude. Nonetheless, as shown in Figure 2.4, due to hybridisation the antisymmetric and symmetric edge states are not at the same frequency, which means that the asymmetric edge states are not eigenmodes of the system. Yet, it was also noted in the previous chapter that with increasing length of the line as well as coupling ratio, the two resonances converge and may become arbitrarily close. In addition, the calculation of eigenfrequencies does not capture that in any lossy system (and hence any real system), the resonances acquire a finite linewidth. The lineshape, typically a Lorentzian, becomes wider as the losses in the system increase, to a point where there is significant overlap between the two resonances,

as illustrated in Figure 3.3, where a Lorentzian with a linewidth typical for edge states of the structures discussed here is shown, sometimes even making them indistinguishable if the lines are close enough. Because of this overlap, the desired asymmetric superposition states, may indeed be excited.

Curiously, this situation of two resonant branches approaching the resonant frequency as the coupling ratio tends to infinity is reminiscent of a different physical situation that mathematically is similar, namely the excitation of surface plasmon polaritons at surfaces of a silver slab [103]. Each of the surfaces can independently support a surface wave, with field amplitude decaying exponentially away from the surface, with a dispersion curve approaching the surface plasma frequency as the wave number along the surface tends to infinity. If, however, a slab is sufficiently thin, two surface plasmon polariton modes couple, which results in splitting of the dispersion curve into two branches due to hybridisation, one still approaching the surface plasma frequency from below and the other from above. Right at the surface plasma frequency, the resulting fields are actually also a superposition of the contributions from these two modes, which may result in an exponentially growing solution within the silver slab. Another analogy well known to the metamaterial community is the hypothetical case of a metamaterial with the refractive index $n = -1$, which quite miraculously results in growing evanescent modes within a metamaterial slab, though not because the frequency at which $n = -1$ corresponds to a resonant surface plasmon polariton mode, but because it is right between two surface plasmon polariton resonances, a symmetric and an antisymmetric mode, with one being just above the frequency at which $n = -1$ and the other being just below it [62].

It is important to be noted that the asymmetric edge state created through superposition is not a resonant mode of the structure. The shape of the asymmetric currents shown in Figure 3.3(d) and (e) relies on equal superposition of two modes at the resonant frequency where they spectrally overlap, with deviations from the equal superposition resulting in a higher amplitude on the opposing edge as well, which in the case

of power transfer would be disadvantageous as it would result in additional dissipation there.

3.2.2 Asymmetry through tuning

Besides the excitation of asymmetric edge states by relying on the asymmetry through superposition, there is a second useful way of selective excitation of an asymmetric edge state on one edge only. This is done by utilising the load impedance as an asymmetry-inducing element. Contrary to the prior method, which relies on the operation frequency of the system being the resonant frequency of a single element, in this case the asymmetry becomes a feature of the system itself which is also reflected in the shape of the resonances as shown in the following.

In order to break the mirror symmetry of the diatomic magnetoinductive line without relying on the excitation, the load impedance comes to mind as natural asymmetry in a wireless power transfer setup. In general, the load impedance is a complex quantity

$$Z_\mathrm{L} = R_\mathrm{L} + \mathrm{j}X_\mathrm{L}, \tag{3.1}$$

where the real parameters R_L and X_L are the load resistance and the load reactance, respectively. They act as an additional (useful) loss in the case of the load resistance but also as an additional reactance for the last element. The effect of the additional reactance can be quantified by considering an element loaded with a purely reactive load, i.e.

$$Z_0(\omega) + Z_\mathrm{L} = \mathrm{j}\omega L + \frac{1}{\mathrm{j}\omega C} + \mathrm{j}X_\mathrm{L} \tag{3.2}$$

The detuned resonant frequency $\omega_{0,\mathrm{X}}$ of such a reactively loaded element can be calculated from

$$0 = \mathrm{j}\omega_{0,\mathrm{X}} L + \frac{1}{\mathrm{j}\omega_{0,\mathrm{X}} C} + \mathrm{j}X_\mathrm{L}. \tag{3.3}$$

Rearranging Equation (3.3) yields

$$\frac{\omega_{0,\mathrm{X}}^2}{\omega_0^2} - 1 + \frac{\omega_{0,\mathrm{X}}}{\omega_0^2} X_\mathrm{L} C = 0. \tag{3.4}$$

Solving this for the detuned resonant frequency under the assumption of small detuning ($\omega_{0,\mathrm{X}}/\omega_0 \approx 1$) results in

$$\frac{\omega_{0,\mathrm{X}}}{\omega_0} = \sqrt{1 - \frac{X_\mathrm{L}}{\omega_0 L}}, \tag{3.5}$$

where again for small detuning ($|X_\mathrm{L}| \ll \omega_0 L$) can be approximated by a Taylor expansion of the square root, resulting in

$$\omega_{0,\mathrm{X}} \approx \omega_0 - \frac{X_\mathrm{L}}{2L}, \tag{3.6}$$

which shows that for small detuning, the resonant frequency shifts approximately linearly with the detuning reactance X_L.

To show that this load reactance does indeed also tune the edge state, Figure 3.4 shows a comparison of the resonances without detuning (just as in Figure 2.4), with a negative load reactance of $X_\mathrm{L} = -10\,\Omega$ as well as a positive load reactance of $X_\mathrm{L} = 10\,\Omega$. For both detuned cases, it can clearly be seen that the edge states were moved to a higher and a lower frequency in the case of positive and negative load reactance, respectively. Moreover, only the edge state that resided on the loaded element was moved, while the edge state on the other edge was not noticeably influenced, showing that they may indeed by controlled independently. Lastly, looking at the resonance shapes shown in the insets in Figure 3.4, the shapes of the resonances in the detuned cases shown in Figure 3.4(d) and (e) are inherently asymmetric as opposed to the symmetric and antisymmetric edge states in Figure 3.4(a) and (b), which marks a change from the case without detuning. Despite their asymmetry though, these current profiles are still following the characteristic shape of the edge states seen so far, as shown by the exponential envelopes plotted in Figure 3.4, just being genuinely asymmetric resonances now. This shows that, as expected from a topological signature of the system, the edge states

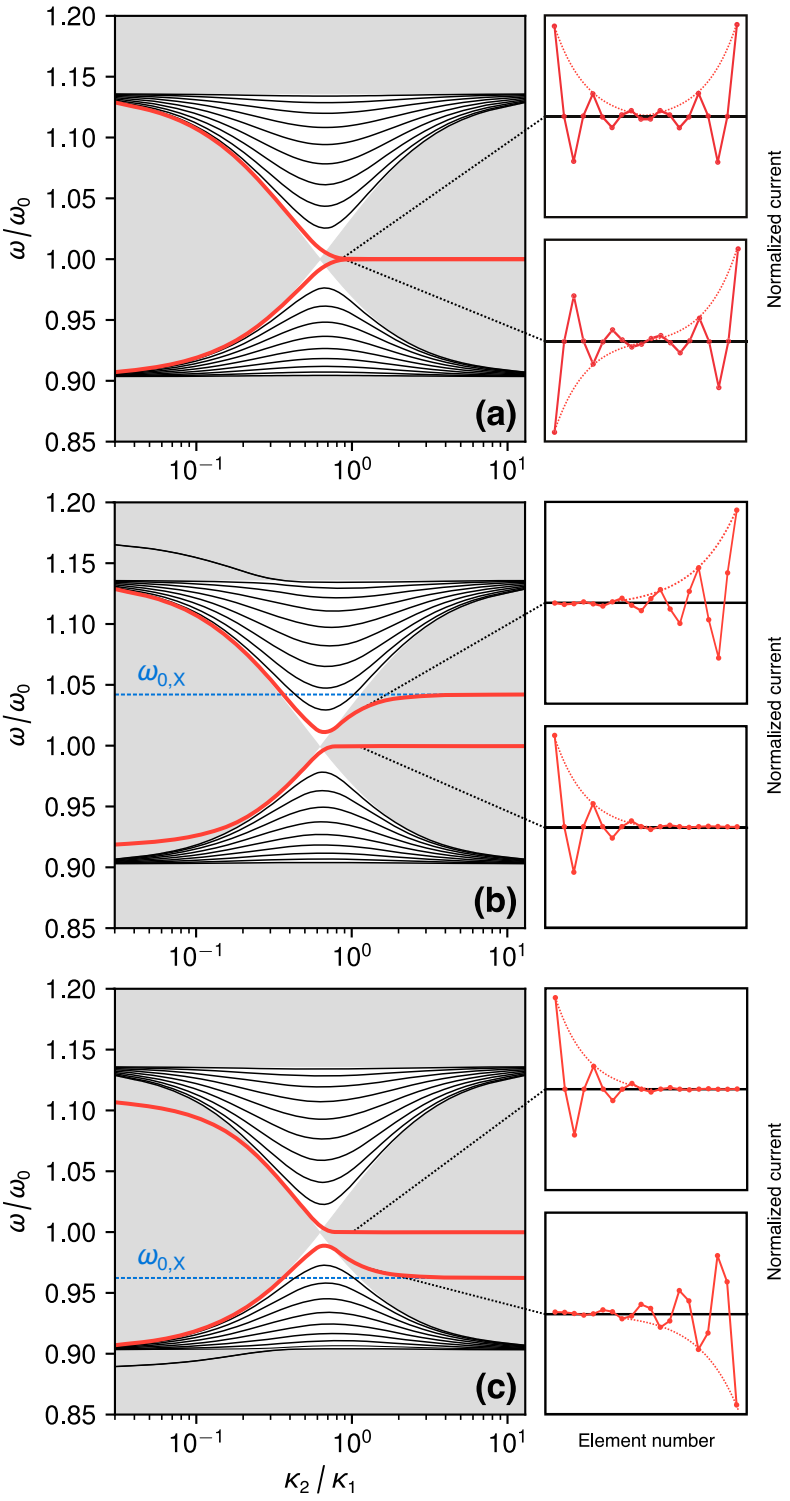


Fig. 3.4: Effect of edge element detuning on frequencies of the topological edge states. It is possible by virtue of adding a detuning reactance to the loaded edge to move away an asymmetric edge state localised at the loaded end to a different frequency. **(a):** Case without detuning. **(b):** Detuning with a negative load reactance $X_\mathrm{L} = -10\,\Omega$ of moves the edge state localised at the loaded end to a higher frequency. **(c):** Detuning with a positive load reactance $X_\mathrm{L} = 10\,\Omega$ of moves the edge state localised at the loaded end to a lower frequency.

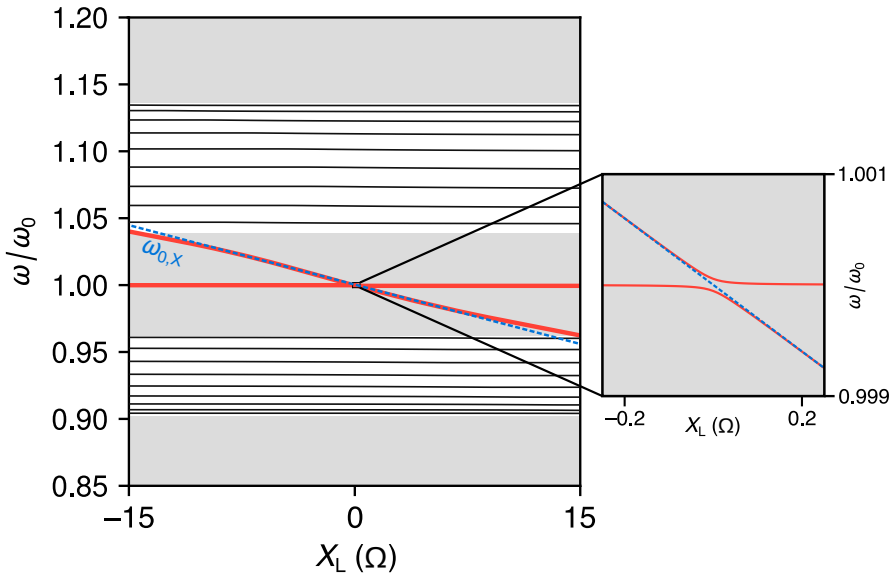


Fig. 3.5: The frequencies where the topological edge states occur depend on the detuning reactance X_L. The edge state on the edge where the load impedance is located shows an approximately linear dependency, with the edge state frequency moving to the detuned resonant frequency of the edge element.

are quite robust to such a perturbation as it does not globally break any symmetry of the line but only very locally.

Additionally, in Figure 3.5, the dependence of the frequencies where the edge states lie on the detuning reactance is shown. The dependence is nearly linear and the detuned frequency of the edge state approximately corresponds to the detuned frequency of the edge element as given by Equation (3.6). This approximation fails for very large detuning reactances but also in the vicinity of no detuning, as shown in the inset of Figure 3.5, as the frequencies of the edge states get close enough for both modes to hybridise, leaving a small frequency gap as expected from the results shown and discussed in Section 3.1 and Chapter 2.

In summary, it was demonstrated that it is also possible to generate an asymmetry in the edge state through detuning. Moreover, this approach also makes it possible to move the asymmetric edge states away from the centre of the stopband at ω_0 to a desired frequency inside the stopband, which is useful as it allows for a precise tuning of

the operation frequency of the system for power transfer without having to tune ω_0 in every single element of the diatomic line.

3.3 Analysis of topological wireless power transfer

Equipped with a qualitative understanding, it is now time to put the proposal for wireless power transfer based on topological edge states to a quantitative test. In the following, it will be investigated if this method does actually allow for efficient transfer as well as discussed where potential advantages and disadvantages may lie.

For the system studied here, the parameters were chosen to be $\omega_0 = 2\pi \times 10^9$ rad/s for the resonant frequency of a single element, $Q = 200$ for the quality factor, $L = 20\,\mathrm{nF}$ and $N = 6$. The coupling coefficients were chosen as $\kappa_1 = 0.15$ and $\kappa_2 = 0.3$. These numerical values were chosen according to previous experimental realisations [44, 104]. Ultimately, though, the magnetoinductive wave theory which this discussion relies on was shown to be highly scalable, meaning the results shown here may readily be generalised to other systems.

3.3.1 Optimal load for efficient power transfer

With the parameters for the power transfer system largely locked in, the question of efficient wireless power transfer becomes an optimisation problem. The figure of merit that is to be optimised is the power transfer efficiency

$$\eta = \frac{P_{\mathrm{out}}}{P_{\mathrm{in}}}, \tag{3.7}$$

where

$$P_{\mathrm{out}} = \frac{1}{2}\mathrm{Re}(Z_{\mathrm{L}})\,|I_N|^2 \tag{3.8}$$

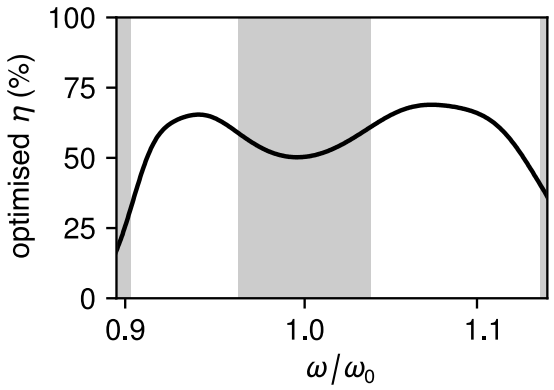


Fig. 3.6: Optimised efficiency η, with the optimal load chosen for every frequency point. The stopbands are indicated by grey shading. Due to the excitation of a topological edge state on the loaded element, the efficiency remains high in the stopband.

is the output power and

$$P_{\text{in}} = \frac{1}{2}\text{Re}(I_1 U_1^*) \tag{3.9}$$

is the input power. The efficiency η is a measure for how much power is delivered to the termination load compared to how much power is put in, with the efficiency limit (which is unattainable in structures with any Ohmic loss) being $\eta = 100\%$.

To determine η, an excitation for the structure is defined using a voltage vector

$$\mathbf{U} = \begin{bmatrix} 1 \\ 0 \\ \vdots \\ 0 \end{bmatrix} \text{V}, \tag{3.10}$$

and then the currents are calculated by using the inversion of the generalised Kirchhoff's equations

$$\mathbf{I} = Z^{-1}\mathbf{U}, \tag{3.11}$$

i.e. by inverting the impedance matrix numerically at every frequency point.

The optimisation parameter is the load impedance Z_{L}. The resulting efficiency may depend strongly on the choice of load impedance, hence the optimal load needs to be determined accurately by an optimisation algorithm in order to calculate the best

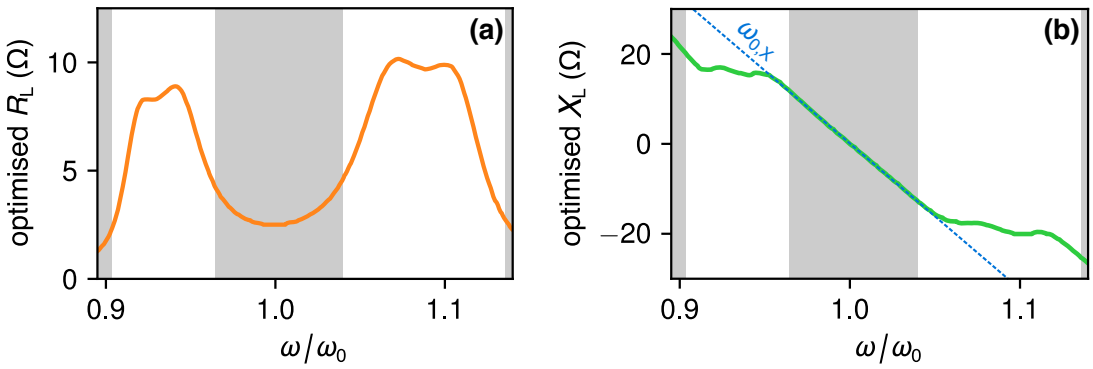


Fig. 3.7: **(a):** Load resistance $R_L = \mathrm{Re}(Z_L)$ for optimised power transfer efficiency at every frequency point. **(b):** Load reactance $X_L = \mathrm{Im}(Z_L)$ for optimised power transfer efficiency at every frequency point. The blue line shows the reactance needed to tune a single resonator to each frequency. The stopbands are indicated by grey shading.

possible transfer efficiency.

The result of this optimisation is illustrated with Figure 3.6 displaying the optimum efficiency and Figure 3.7 showing the load impedance required to achieve this optimum efficiency. Figure 3.6 shows the best possible transfer efficiency as determined by the optimisation. The load was optimised separately for every frequency point, meaning that this is the best attainable efficiency for each frequency. It can clearly be seen that, apart from the outer stopbands, the efficiency remains high including inside the central stopband. A quick look at the current profile for example at $\omega = \omega_0$, which is displayed in Figure 3.8, confirms that a growing asymmetric edge state is indeed excited there. While a decaying edge state localised on the left edge is weakly excited as well, the growing edge state localised on the right edge is dominant, leading to efficient power transfer onto the loaded element. For such topological power transfer through the edge states, the maximum efficiency is greater than 50%. On the other side, the maximum possible efficiency of power transfer by virtue of propagating waves, is approximately 65% in the lower passband at $\omega = 0.942\omega_0$ with optimal load $Z_L = (8.87 + 15.4\mathrm{j})\,\Omega$ and approximately 69% in the upper passband at $\omega = 1.075\omega_0$ with optimal load $Z_L = (10.12 - 17.6\mathrm{j})\,\Omega$. Although the efficiency is somewhat lower in the stopband than it is in the passbands, it is still comparable and usefully large. This

observation is interesting, as the stopband was conventionally thought to, as the name suggests, stop power passing through the structure at frequencies in it. Nonetheless, here it is clearly shown that power may indeed efficiently pass through the structure in the stopband of this line at realistic system parameters. Additionally, while efficient power transfer through the edge states is possible right at $\omega = \omega_0$, this is the minimum efficiency inside the stopband. A look at the optimal load reactance in Figure 3.7, shows that to leave this minimum, the last element should be detuned linearly with frequency. As observed in Section 3.2 and shown in Figure 3.5, the linear detuning of the last element to the operation frequency creates an asymmetric edge localised on the right edge and thus suitable for power transfer at that frequency. This in turn allows for the efficiency to be increased.

Lastly, it should be noted that the choice of parameters here was made to mirror a realistic system and thus is not optimal: There is no finite optimum for the quality factor and the coupling coefficients, as fewer losses always correspond to higher efficiencies. As wireless power transfer using propagating waves exhibits comparable yet slightly higher efficiencies than topological wireless power transfer, the ratio of the coupling coefficients also has no well-defined optimum inside the band gap.

3.3.2 Electromagnetic pollution and safety

One very striking advantage of wireless power transfer based on topological edge states lies in the different mode shape of the resonances in the stopband. As can be seen for example in Figure 3.8, the highest current amplitudes are found at the edges of the line. Conversely, in the bulk of the line, currents remain relatively low. This may be quantified by defining a measure ρ for the average ratio of the magnitude of the currents on the bulk elements to the current on the loaded edge element as

$$\rho = \frac{1}{(N-2)|I_N|} \sum_{n=2}^{N-1} |I_n|. \tag{3.12}$$

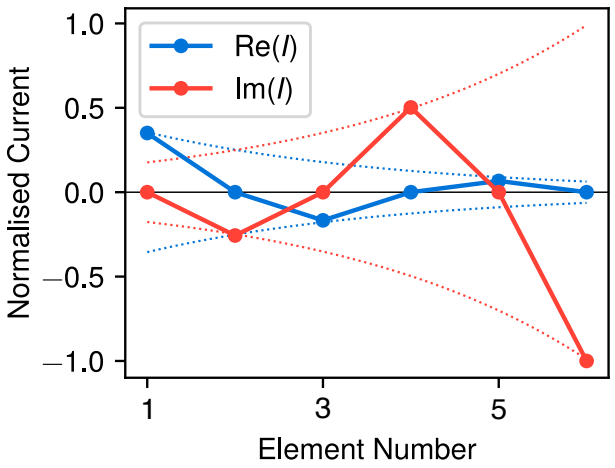


Fig. 3.8: Current profile for diatomic magnetoinductive line excited at the first element and loaded optimally at the last element for optimal efficiency at $\omega = \omega_0$. The dotted lines show the exponential law for the shape edge states. While there are some weak amplitudes on the left-hand edge, the overall amplitude clearly grows asymmetrically towards a high amplitude on the loaded element on the right-hand edge, enabling topological wireless power transfer to be efficient. Additionally, the amplitudes in the bulk remain comparatively low.

In Figure 3.9, the bulk current ratio is plotted for the set of load impedances shown in Figure 3.7 optimised for maximum efficiency. In the centre of the stopband at $\omega = \omega_0$ the bulk current ratio is only $\rho = 0.46$ whereas in the passbands it may exceed $\rho = 1.2$ with the value $\rho = 1.11$ at $\omega = 1.075\omega_0$ where the highest efficiency for propagating wave power transfer was found. Thus, topological wireless power transfer allows for an approximately 2.5-fold reduction in the bulk current ratio.

Since the bulk current translates directly to the magnetic field strength around the mediating elements as well as to heating losses, the use of edge states may be of considerable potential interest for applications where electromagnetic pollution and safety play a role, such as wireless power transfer in the presence of devices particularly sensitive to electromagnetic interference ranging from pacemakers [105] to sensitive metrological tools [106] as well as when transferring power through heat-sensitive media such as biological tissue [107] or cryogenic environments [108].

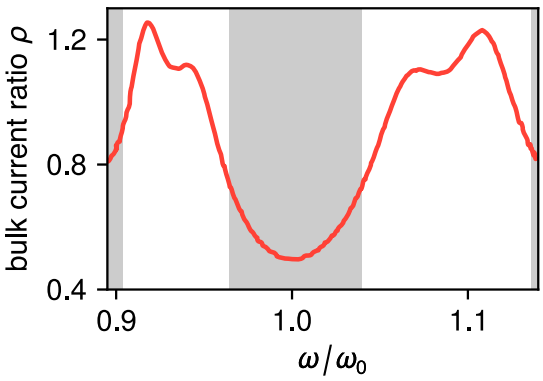


Fig. 3.9: Bulk current ratio ρ for a line optimised for maximum efficiency at every frequency. The stopbands are indicated by grey shading. For the power transfer *via* edge states in the central stopband, a very significant drop in bulk current can be seen, despite comparable transfer efficiencies, implying that topological wireless power transfer may operate at lower currents offering potential advantages with regards to electromagnetic pollution and safety.

3.3.3 Robustness against disorder

The property that has perhaps garnered topological states the most attention is their remarkable robustness in the face of external perturbations. While the term robustness quite often remains a qualitative description, for wireless power transfer it is possible to quantify it in terms of the efficiency of the magnetoinductive line when it is subjected to increasingly large perturbations. Less impact of external perturbations then implies superior stability of the wireless power transfer. First though, it is important to specify precisely which perturbations are under investigation here. There are two main types of random perturbations that can occur, namely on-site disorder as well as coupling disorder. In terms more suited to magnetoinductive theory, these two correspond to random perturbations of the self-impedance and random perturbations of the mutual impedance, respectively.

Considering perturbations of the mutual impedance, it can be assumed that most perturbations of the coupling will arise from random variations of the distance between

the elements. As shown in Equation (1.13), the mutual inductance obeys an inverse cubic law with respect to that distance, i.e.

$$\kappa_{n,m} \propto \frac{1}{d_{n,m}^3}, \tag{3.13}$$

where d_{nm} denotes the distance between elements n and m of the line. Hence, random disorder in the distance between them can be expressed as

$$d_{n,m} = (1 + \delta_{n,m})\bar{d}_{n,m}, \tag{3.14}$$

where $\bar{d}_{n,m}$ is the nominal distance, i.e. without any perturbations applied to the system, and $\delta_{n,m}$ is the disorder parameter, which quantifies the local strength of the disorder. This disorder parameter is a random value distributed uniformly and bounded by the disorder strength δ according to

$$|\delta_{n,m}| < \delta, \tag{3.15}$$

meaning it may assume any value in the interval $(-\delta, \delta)$. To quantify the behaviour of a quantity X (either the efficiency or the bulk current in this work) calculated from a set of N_{samples} random settings each resulting in its own X_n, the mean

$$\langle X \rangle = \frac{1}{N_{\text{samples}}} \sum_{n}^{N_{\text{samples}}} X_n \tag{3.16}$$

as well as the positive and negative semideviations defined as

$$\sigma_{\pm}(X) = \sqrt{\frac{1}{N_{\text{samples}}} \sum_{X_n \gtrless \langle X \rangle} \left(\langle X \rangle - X_n\right)^2} \tag{3.17}$$

are used. The reason for using semideviations as opposed to the more commonly used standard deviation is that the semideviations quantify the expected upward and downward fluctuation around the mean [109]. Additionally, by definition, the sum of mean and semideviation of X adheres to the same bounds as X itself, meaning implied values

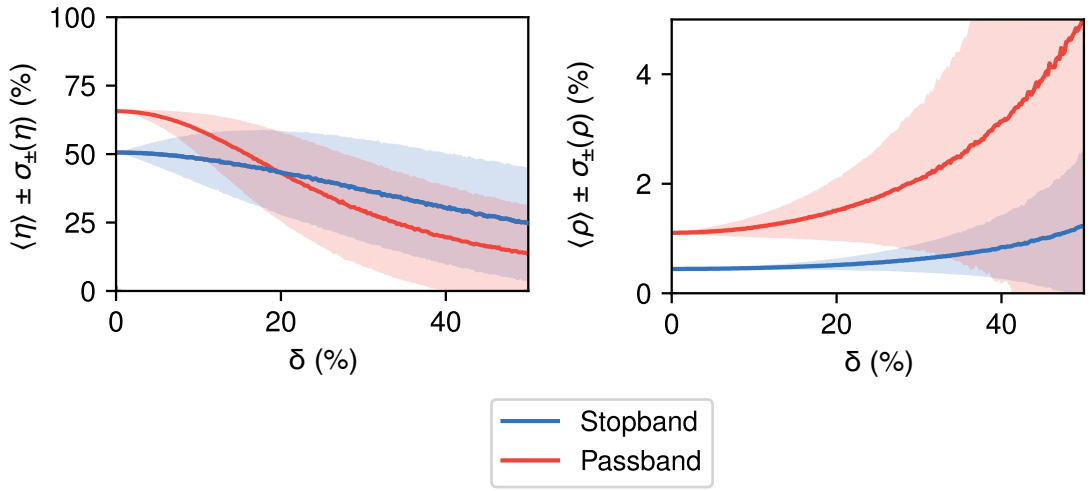


Fig. 3.10: Fluctuation of efficiency $\langle\eta\rangle \pm \sigma_{\pm}(\eta)$ (left) and fluctuation of bulk current $\langle\rho\rangle \pm \sigma_{\pm}(\rho)$ (right) under perturbations of the mutual impedance due to disorder in the element distance. The red curves are for power transfer in the passband *via* propagating waves at $\omega = 0.942\omega_0$, the blue curves for power transfer in the stopband *via* topological edge states at $\omega = 0.98\omega_0$. For smaller perturbations, power transfer via propagating waves provides a higher efficiency on average, while for larger perturbations, power transfer via the edge state exhibits superior stability. Crucially, the edge state mode is more robust in terms of the bulk current, which always remains low.

of the efficiency beyond its physical limits may be avoided.

In Figure 3.10, the fluctuations of both the efficiency and the bulk current under mutual impedance disorder are shown for the case of power transfer in the stopband using topological edge states (at e.g. $\omega = 0.98\omega_0$) as well as conventional wireless power transfer in the passband using propagating waves (at $\omega = 0.942\omega_0$). Turning to the efficiency first, as expected from the unperturbed case discussed earlier, at sufficiently small disorder strengths power transfer in the passband is more efficient. However, as the disorder strength increases, at $\delta \approx 20\%$, the mean efficiency expected from power transfer in the stopband surpasses the mean efficiency expected from power transfer in the passband. Hence, the topological power transfer has superior stability compared to power transfer using propagating waves for mutual impedance perturbations, which rears from the fact that the topological edge states are very robust against this type of perturbation. Additionally, on the right side of Figure 3.10, the fluctuations in the bulk current are shown. The disorder clearly increases the bulk current for both power trans-

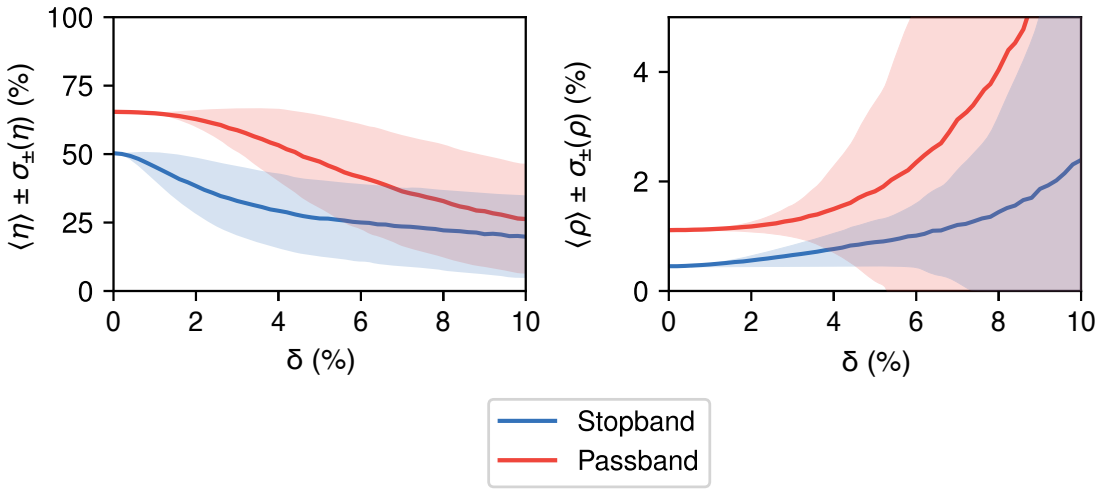


Fig. 3.11: Fluctuation of efficiency $\langle\eta\rangle \pm \sigma_{\pm}(\eta)$ (left) and fluctuation of bulk current $\langle\rho\rangle \pm \sigma_{\pm}(\rho)$ (right) under perturbations of the self-impedance due to disorder in the element capacitance. The red curves are for power transfer in the passband *via* propagating waves at $\omega = 0.942\omega_0$, the blue curves for power transfer in the stopband *via* topological edge states at $\omega = 0.98\omega_0$. This type of perturbation causes very rapid deterioration of the efficiency, for both propagating-wave and topological wireless power transfer.

fer in the stopband and in the passband, but this increase is far less significant for the stopband for which the bulk current on average does not just remain below the average bulk current for the passband but their ratio actually further increases. Thus, the advantage in terms of electromagnetic pollution and safety is expected to become even more pronounced when faced with setting where external perturbations play a significant role.

The second type of perturbation to consider is disorder in the self-impedance. As the geometry of magnetic resonators can typically be reproduced rather accurately, the main source of perturbation in the self-impedance is the capacitance of the elements. Hence, the perturbation is introduced through a variation of the capacitance C_n of each element according to

$$C_n = (1 + \delta_n)\bar{C}_n, \tag{3.18}$$

where $\bar{C}_n$ is the nominal capacitance of element, i.e. in the system without perturbations. Once again, the disorder parameter δ_n introduces the local strength of disorder and is bounded by the disorder strength

$$|\delta_n| < \delta, \tag{3.19}$$

being chosen randomly and uniformly from the interval $(-\delta, \delta)$. In terms of the resonant frequency, this perturbation results in random perturbations of ω_0 according to

$$\omega_{0,n} = \frac{\bar{\omega}_{0,n}}{\sqrt{1+\delta_n}}, \tag{3.20}$$

where $\bar{\omega}_{0,n}$ denotes the nominal resonant frequency of the element. Just as in the first case, the mean value and the semideviations are used to quantify the resulting fluctuations.

The results are illustrated in Figure 3.11. On the left, it can be seen that in contrast to the case of mutual impedance perturbations, the mean efficiency for power transfer drops off rather rapidly for the passband but also for the stopband. There is also no crossover of the two mean efficiencies, at least not anywhere where the efficiency would still be reasonably high. Thus, it appears that for this type of disorder, the topological states are far less robust. This is indeed the case, as the mutual impedance or coupling perturbation keeps the chiral symmetry, which protects the topology, remains intact whereas for self-impedance or on-site perturbation the chiral symmetry is broken, leading to a diminished robustness against it [110]. Nonetheless, it is important to keep in mind that the self-impedance is far easier to control by increased care in the manufacturing of the resonators. Correspondingly, this type of perturbation may be mitigated and should typically occur less.

3.4 Conclusions

In this chapter, for the first time, an important application of the topological physics of diatomic magnetoinductive chain for wireless power transfer was investigated, nicknamed topological wireless power transfer. To this end, it was shown that asymmetric edge states may be engineered either at the centre of the stopband by virtue of superposition or elsewhere in the stopband by virtue of detuning the edge element. Such an asymmetric edge state may exhibit a localised high amplitude only in the vicinity of the loaded last element of a diatomic chain of coupled resonators. Consequently, this high amplitude on the load then allows for wireless power transfer to take place in the stopband at efficiencies comparable to power transfer using propagating waves in the passband, despite conventional intuition implying that in the stopband waves are stopped and little to no power may pass through the structure. Furthermore, the current profile of the topological edge states, which exhibits low amplitudes in the bulk of the line, allows for far lower average currents in the bulk compared to the passband, decreasing electromagnetic pollution and increasing the safety of this mechanism for power transfer. Lastly, it was seen that the inherent robustness of topological edge states, which are protected by the global symmetries of the system, means that topological wireless power transfer offers superior stability in the face of random coupling disorder over its conventional propagating wave-based counterpart, making it an ideal choice for applications where large perturbations to the wireless power transfer system are expected but minimal fluctuations are desired, such as flexible wireless power transfer lines [97] or wireless power transfer through media with unknown inhomogeneities [111].

4 Topological wireless communication

Wireless systems may not just transfer energy, but, and perhaps more commonly, also information. Wireless communication based on magnetoinductive waveguides was shown to be both feasible and useful [45, 46]. The following section discusses a few of its most prominent uses, leading to the natural question if, considering the advantages of topological wireless power transfer, it is also possible to use topological edge states advantageously for wireless communication.

A positive answer is provided in this chapter showcasing the uses of topological wireless communication. To this end, the magnetoinductive line hosting topological edge states is examined for its properties regarding wireless communication for the first time. Specifically, figures of merit important for communications channels, namely the signal power and the Shannon capacity are analysed. It is shown that topological wireless communication may outperform its conventional counterpart based on propagating waves in both. Additionally, the robustness of topological wireless communication against disorder is discussed, demonstrating that the robustness of the topological edge states also increases the robustness of the signal power enhancement.

The work shown here was also published in Refs. [77] and [78].

4.1 Wireless communication: Introduction

In this section, prior to the discussion and analysis of topological wireless communication, a brief review of and introduction to wireless communication with a particular focus on the context of magnetoinductive wave communication shall be given.

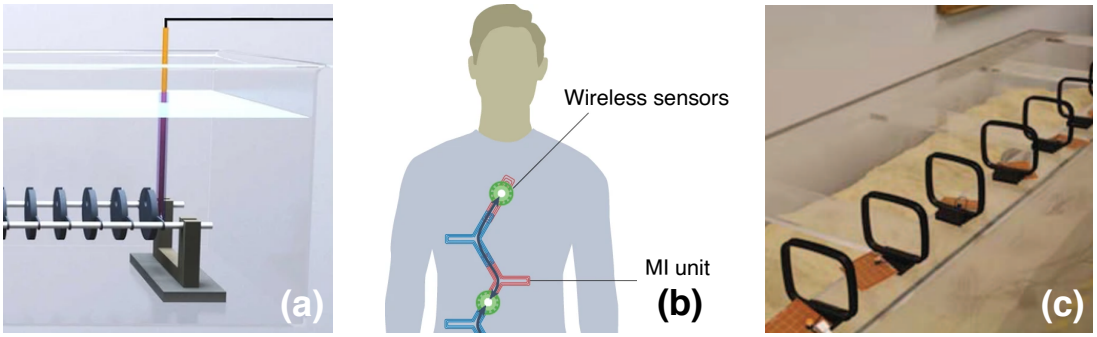


Fig. 4.1: Magnetoinductive wave communication has a wide range of proposed use cases, such as **(a)** underwater communication (adapted from [60]), **(b)** flexible, wearable communication lines (adapted from [112]), **(c)** underground communication (adapted from [113]).

The purpose of communication systems is to provide a communication channel, i.e. a range of frequencies with sufficient signal power to transmit information with. Wireless communication methods, meaning the transmission of information without a continuous conductive path, may be grouped into far-field and near-field communication methods [88]. Magnetoinductive wave communication is based on near-field coupling and hence belongs to the latter category. The roots of near-field wireless communication are commonly traced back to radio-frequency identification (RFID), a technology based on the work by Harry Stockman in 1948 [114], where passive tags are activated and read by means of radio signals. It led to the development of a standard for communication based on near-fields, which is also known by the same name of near-field communication or more commonly NFC [115]. Despite its origination from an identification method, near-field communication has a wide range of uses beyond that. Magnetoinductive wave communication, meaning the use of magnetoinductive waveguides as communication lines [45, 46], sometimes equivalently termed magnetic induction communication, has attracted attention as a method for wireless communication in settings where other platforms such as far-field antennas underperform. This includes communication through lossy or heterogeneous media such as water [60, 116, 117] or underground [118–120] (see Figure 4.1(a) and (c), respectively), where the magnetic coupling mechanism of such systems enables greatly reduced perturbation by said me-

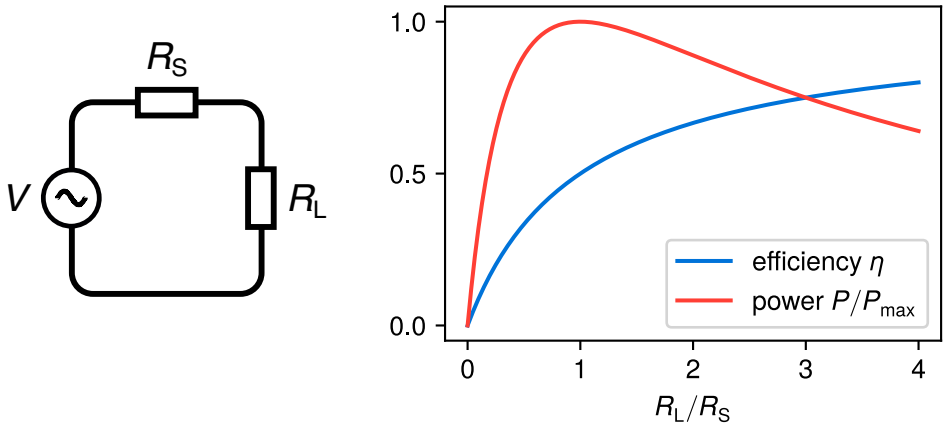


Fig. 4.2: Simplified model for power dissipation by a receiving load resistance R_L in the presence of a source resistance R_S (left). The power delivered to the receiver is greatest when the load resistance is matched, i.e. $R_L = R_S$. Crucially, the efficiency is not optimal in this scenario but always equal or less than 50%.

dia and the magnetic resonators are deployed more easily and thus more cheaply than for example a wired connection [121]. Further, magnetoinductive communication has also been shown to be a promising candidate for wearable communications systems (see Figure 4.1(b)), where waveguides have to transmit through textiles or skin as well as conform to their shape and thus flexibility is key [112, 122]. In summary, a whole range of potential applications of magnetoinductive communication links exist, motivating their further development.

4.2 Impedance matching

An important concept in the transmission of signals and hence in wireless communication is impedance matching. The key question in communications systems with regard to determining the load impedance is which impedance maximised the signal power transmitted to the load. An understanding of this can be gained from a simple circuit model for a signal transmission system, which is shown in Figure 4.2 on the left. In this model, the current flowing through the load resistance according to Ohm's law

is

$$I = \frac{V}{R_S + R_L}. \tag{4.1}$$

Correspondingly, the power P delivered to the load is

$$P = \frac{1}{2} R_L |I|^2 = \frac{1}{2} \frac{V^2 R_L}{(R_S + R_L)^2} \tag{4.2}$$

The function $P(R_L)$ has a maximum, which may be calculated from

$$0 = \frac{\mathrm{d}}{\mathrm{d}R_L} \left[\frac{V^2 R_L}{(R_S + R_L)^2} \right] = |V|^2 \frac{R_S - R_L}{(R_S + R_L)^3}. \tag{4.3}$$

Clearly, the power is maximised when

$$R_L = R_S, \tag{4.4}$$

a condition known as impedance matching. The derivation for circuits which are not purely resistive but where a source and a load reactance are involved is largely analogous to the simpler case shown here. In that case, the impedance matching condition is found to be

$$Z_L = Z_S^*, \tag{4.5}$$

where Z_L denotes the load impedance and Z_S the source impedance. Physically, this translates to the choice of load impedance for which there is no discontinuity in the transmission system, so that reflections are suppressed and all of the power is absorbed by the load.

The efficiency in the case of matched impedances turns out to be

$$\eta = \frac{P}{P_{\text{in}}} = \frac{R_L |I|^2}{(R_L + R_S)|I|^2} = \frac{R_L}{(R_L + R_S)} = 50\%. \tag{4.6}$$

Thus, as the maximum possible efficiency in passive systems is 100%, systems with matched impedance remain significantly below this limit with efficiencies of at best 50%.

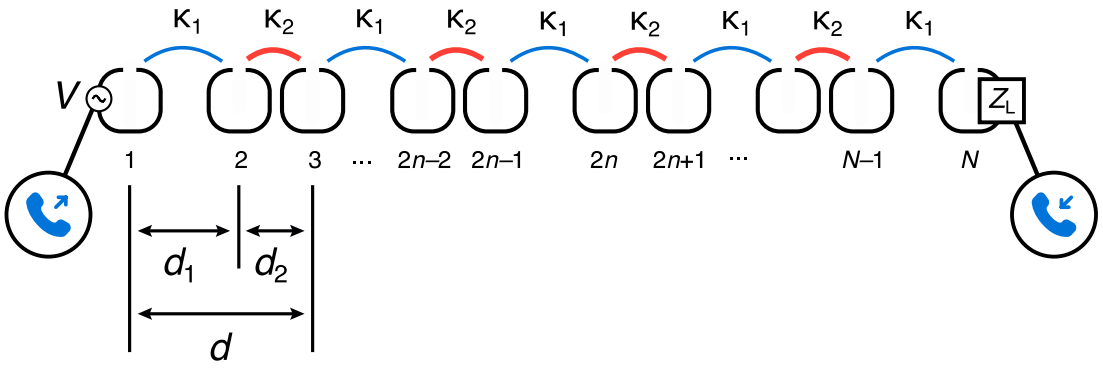


Fig. 4.3: Sketch of a wireless communication system based on a diatomic magnetoinductive line with coupling coefficients κ_1 and κ_2.

However, this does not mean that the efficiency may not exceed 50%, merely that systems with optimum efficiency and systems with optimum power are clearly distinct from each other. Correspondingly, the results for wireless power transfer as elaborated on in the previous chapter are not transferable to the application of wireless communication as discussed in this chapter.

4.3 Analysis of topological wireless communication

In the following section, topological wireless communication shall be analysed in detail. The system under investigation is a diatomic magnetoinductive waveguide, as sketched in Figure 4.3. Such a configuration was already shown to host topological edge states, which may also be engineered to be asymmetric, as discussed in Chapters 2 and 3. Now, these topological edge states shall be harnessed for the purpose of wireless communication.

From here on, to make all calculations definite, realistic fixed parameters are chosen for the resonant frequency $\omega_0 = 10$ MHz, the quality factor of $Q = 250$ as well as the inductance of $L = 7$ µH. Once again though, the scalability of most results is implicit.

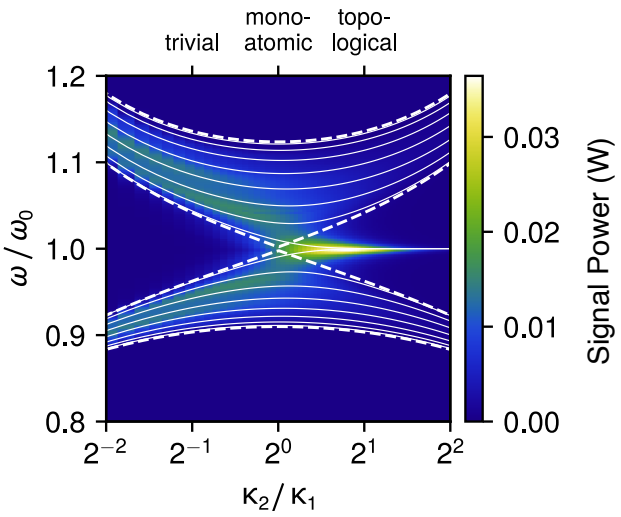


Fig. 4.4: Optimisation of the signal power for different ratios of the coupling coefficients κ_2/κ_1, where the load impedance is matched for every configuration at every frequency. The transmission distance is kept constant. Dashed lines show the edges of the passbands and solid lines indicate the eigenfrequencies of the system.

4.3.1 Power enhancement

A key figure of merit for any wireless communication link is the signal power P seen by the receiving load impedance. In this system, it reads

$$P = \frac{1}{2}\mathrm{Re}\left(Z_\mathrm{L}\right)\left|I_N\right|^2, \tag{4.7}$$

where I_N is the current in the last element of the link, where the load impedance is located. Both the coupling coefficients κ_1 and κ_2 as well as the load impedance Z_L are presently free parameters for which the configuration yielding the maximum signal power may be determined by an algorithmic optimisation. In order to optimise the coupling, a benchmarking procedure needs to be defined for this type of near-field communication platform. Whether and how well a platform is suitable for transmitting signals is determined by two interlinked factors, namely its transmission distance and the signal strength it manages to transmit over this distance. Clearly, they are related, as typically signal power decreases with increasing transmission distance, to which this system is no exception. For antenna systems, the signal decay is due to radiation that

does not reach the receiver [61]. In a transmission line like a coaxial cable, the main source of losses is heat dissipation due to Ohmic losses and in the dielectric [123]. In the present case of near-field coupling, the losses are due to Ohmic and dielectric losses as well as the vanishing of the coupling coefficients between neighbouring elements [60, 62]. Correspondingly, when comparing different realisations of magnetoinductive waveguides operating at the same frequency, it is necessary to compare chains suited for equal transmission distance. When the meta-atoms are small and thus do not take up much space themselves, which is the case here, they do not contribute to the length of the chain noticeably. Then, the transmission distance of the chain is exclusively determined by the coupling (or *vice versa*). The coupling of any two meta-atoms here approximately scales as

$$\kappa \propto \frac{1}{d^3}, \tag{4.8}$$

where d is the spacing between the two resonant elements. Equation (4.8) may be inverted to calculate the distance between two elements from their coupling coefficient as

$$d \propto \frac{1}{\kappa^{1/3}}, \tag{4.9}$$

which directly implies that the total transmission distance D for a chain with N elements and a set of coupling coefficients κ_i is

$$D \propto \sum_i^N \frac{1}{\kappa_i^{1/3}}. \tag{4.10}$$

Thus, the condition to ensure equal chain length and hence transmission distance can be written as

$$\sum_i^N \frac{1}{\kappa_i^{1/3}} = \sum_i^N \frac{1}{\tilde{\kappa}_i^{1/3}}, \tag{4.11}$$

where the κ_i and $\tilde{\kappa}_i$ are the coupling coefficients of two possibly different chains.

With this in mind, the optimal signal power may now be calculated. The transmission distance is fixed such that $\kappa_1^{-1/3} + \kappa_2^{-1/3} \approx 3.38$, ensuring comparability of the chains

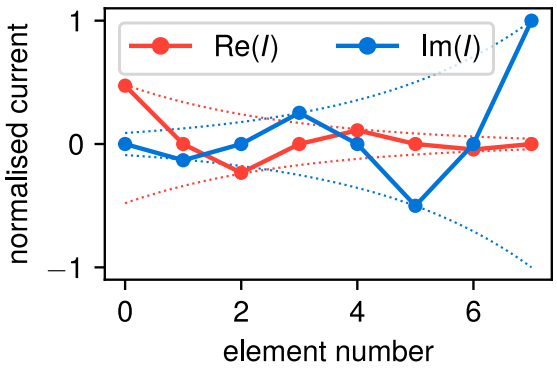


Fig. 4.5: Normalised real and imaginary part of current I for optimal signal transmission (at $\omega = \omega_0$ for $\kappa_2/\kappa_1 = 2$) *via* topological edge states. The dotted lines show the exponential functions according to Equation (2.41) enveloping the real and imaginary parts of the current, displaying the exponential nature of the amplitude decay away from the edges of the chain.

even when the coupling coefficients vary. Figure 4.4 shows the optimised signal power for a chain with a number of elements of $N = 8$. At every frequency, the optimal, i.e. matched, load impedance is determined numerically. Two passbands of higher signal power which are separated by a bandgap that widens with increasing deviation from the monoatomic case, i.e. equal coupling coefficients, can be observed. The dashed lines showing the analytically determined edges of the passbands in Equations (2.20) and (2.21) confirm this. Further, there is a pronounced spike in signal power in the centre of the stopband for $\kappa_2 > \kappa_1$ due to the topological edge states. Crucially, the signal power due to the edge state exceeds the signal power due to the propagating waves in the passbands, with the global maximum of the signal power being located at $\omega = \omega_0$ and $\kappa_2/\kappa_1 \approx 2$.

Figure 4.5 displays the current profile for this maximum, as expected showing an asymmetric edge state with its maximum located right on the loaded element, confirming the topological edge states as responsible for the enhancement in signal power. For a detailed look at the signal power profile, Figure 4.6 shows the frequency dependency of the signal power for representative choices of the coupling ratio κ_2/κ_1. The topological case giving the global maximum of signal power with $\kappa_2/\kappa_1 = 2$ can now be compared to the monoatomic case with $\kappa_2/\kappa_1 = 1$ as well as to the topologically triv-

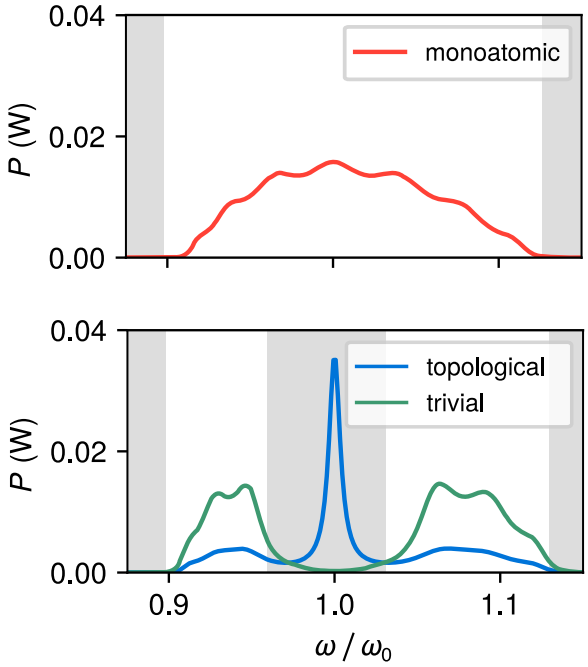


Fig. 4.6: Optimal signal power profiles for the monoatomic ($\kappa_2/\kappa_1 = 1$, blue), topological ($\kappa_2/\kappa_1 = 2$, blue) and trivial case ($\kappa_2/\kappa_1 = 1/2$, green). The shaded frequency ranges indicate the passbands. It can be seen that the peak signal power transmitted by the topological exceeds the signal power supplied by both the trivial as well as the monoatomic chain.

ial case with inverse coupling ratio of $\kappa_2/\kappa_1 = 1/2$: It can be seen that the peak signal power transmitted by the topological chain exceeds both the peak power given by the monoatomic chain as well as the peak power supplied by the topologically trivial chain with inverse coupling ratio significantly. Compared to the monoatomic case, the signal power is enhanced by a factor of more than 2.5 when using the topological chain. Remarkably, this enhancement persists even when a fixed transmission distance is not required: Even when the coupling coefficients of the monoatomic chain are increased, corresponding to a reduction in its transmission distance, this does not lead to a maximum signal power exceeding that of a longer topological chain.

As dictated by the maximum power transfer theorem, the power transfer efficiency is comparatively poor at around 40%. Interestingly, while for wireless power transfer the performance of the approach based on topological edge states in the absence dis-

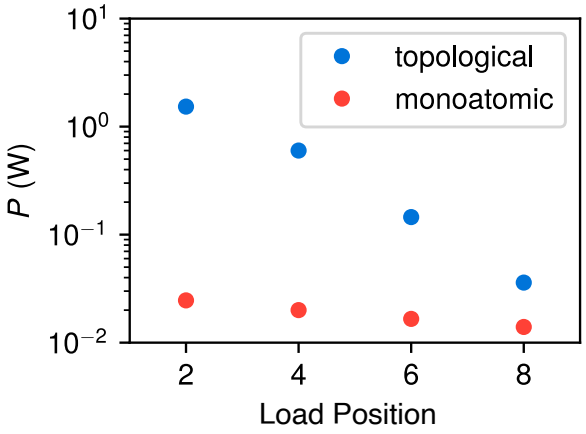


Fig. 4.7: A highly useful property of magnetoinductive waveguides is random accessibility, i.e. the possibility to take out power from different elements along the waveguide. This property persists for topological chains, as shown here, where the variation of the signal power for the topological chain as well as the monoatomic chain with varying position of the load on one sublattice from the unit cell adjacent to excitation to the end of the chain is displayed. For any position of the load, the topological chain supplies a higher signal power than the monoatomic chain.

order was shown to be comparable to the conventional option employing propagating waves, the topological chain actually significantly outperforms all available options in terms of peak signal power.

Before moving to further discussion of the details of topological wireless communication based on edge states, another useful property of magnetoinductive waveguides should be pointed out here, namely, random accessibility [44, 113]. With the term random accessibility, it is specifically meant that the power may be taken out of every unit cell by moving the load, implying a significant advantage in flexibility and reconfigurability compared to, for instance, a conventional wire-based transmission setup. The load for magnetoinductive waveguides is often a movable loaded element, meaning that in most cases, this flexibility should indeed prove useful. While this advantage is established for conventional magnetoinductive waveguiding using propagating waves, it needs to be verified for the topological approach. In Figure 4.7, it is shown that the random accessibility persists also for transmission based on topological edge states. It can be seen that even when the load impedance is moved along the chain, albeit here with the restriction of placing the load on the same element of the unit cell every time,

the signal power transmitted by the topological chain remains consistently higher than that of the conventional monoatomic chain. As a matter of fact, the closer the load is to the excitation, the more strongly enhanced the output power is, which can be understood in terms of the evanescent coupling to the edge state, which vanishes more rapidly as the number of elements and thus the distance between load and excitation is increased. This phenomenon ultimately places a limit on the applicability of topological chains: for a sufficiently long chain where the precise length is determined by the losses, both efficiency and power transmitted through the topological chain become smaller than through the conventional chain as the evanescent coupling to the edge state becomes exceedingly small. The next chapter will discuss a strategy how to mitigate this effect.

In terms of applications at this point, the significant enhancement in power output due to the topological edge states should prove useful in systems where raw power is most important, such as, for example, radio frequency identification (RFID), where exceeding a threshold power level is essential to activate a passive transponder and ultimately determines the distance over which it may be used [124]. In a different but nonetheless interesting direction for applications, it should be pointed out the proposed system may also be of use for localised microwave heating, since as shown in Figure 4.5 the increase in output power is due to the localised maximum in current at the end of the chain. Hence, the maximum heat dissipation occurs in that element while the other elements dissipate considerably less heat, which is desirable for instance for certain biomedical applications [125–127]. However, primary application of the signal power enhancement as envisioned here and discussed in more detail in the latter sections of this chapter, is wireless communication, where stronger signals are amongst the foremost optimisation targets for the construction of any communication link [128].

4.3.2 Robustness against disorder

As the signal power enhancement discussed in Section 4.3.1 was shown to be due to topological edge states, the natural question that arises is whether said enhancement benefits from the robustness of topological edge states against disorder as well. Therefore, random variations of the distance $d_{n,m}$ between any elements n and m

$$d_{n,m} = (1 + \delta_{n,m})\bar{d}_{n,m}, \tag{4.12}$$

where $\bar{d}_{n,m}$ denotes the nominal distance, i.e. the without any perturbations applied to the system. The disorder parameter $\delta_{n,m}$ quantifies the local strength of the disorder and is bounded by the disorder strength δ according to

$$|\delta_{n,m}| < \delta. \tag{4.13}$$

For this perturbation, it is assumed that the coupling coefficients $\kappa_{n,m}$ are proportional to the inverse cube of the distance $d_{n,m}$. From the mean values of the signal power transmitted by the topological chain $P_{\text{topological}}$ as well as the monoatomic chain $P_{\text{monoatomic}}$ over a large number N_{samples} of randomly perturbed realisations, the average signal enhancement

$$\left\langle \frac{P_{\text{topological}}}{P_{\text{monoatomic}}} \right\rangle = \frac{\langle P_{\text{topological}} \rangle}{\langle P_{\text{monoatomic}} \rangle} \tag{4.14}$$

can be calculated. The mean value of a random variable X here is defined as

$$\langle X \rangle = \frac{1}{N_{\text{samples}}} \sum_{n=1}^{N_{\text{samples}}} X_n. \tag{4.15}$$

Additionally, the standard deviation, which measures the average fluctuation of the random quantity is defined as

$$\sigma(X) = \sqrt{\frac{1}{N_{\text{samples}}} \sum_{n=1}^{N_{\text{samples}}} (\langle X \rangle - X_n)^2}. \tag{4.16}$$

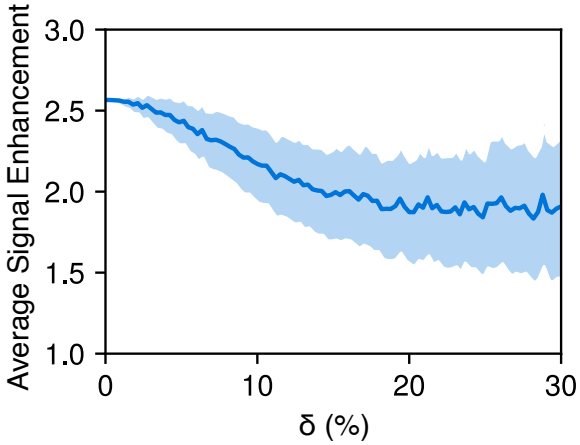


Fig. 4.8: Average signal power enhancement factor achieved by the topological chain compared to the monoatomic chain as a function of disorder strength of coupling disorder. The area shaded in blue indicates the standard deviation of the enhancement factor. Due to the protection of the topological edge state against this disorder in the coupling coefficients, the enhancement remains robust against it.

The semideviations used in Chapter 3 are not needed here, as the sum and difference of standard deviation and mean do not exceed any physical limits. In Figure 4.8, the resulting average signal enhancement and its standard deviation are shown. The number of samples was chosen to be $N_{\text{samples}} = 10^4$, which is sufficiently large to see the tendency of the averaged quantity. It can be seen that the average signal enhancement, while dropping from its high initial value, persists even in the face of significant disorder introduced into the coupling coefficients. Thus, it can be concluded that the robustness of the topological edge states to this type of disorder also causes the signal enhancement to be robust to disorder.

4.3.3 Shannon capacity enhancement

For the purpose of wireless communication schemes, considering only the enhancement of signal power is insufficient. As a second variable, the bandwidth plays an important role in determining the suitability and performance of a given wireless communications link. Most commonly, the bandwidth is defined as the full width at half maximum of the signal power spectrum [128]. To determine the bandwidth of the sys-

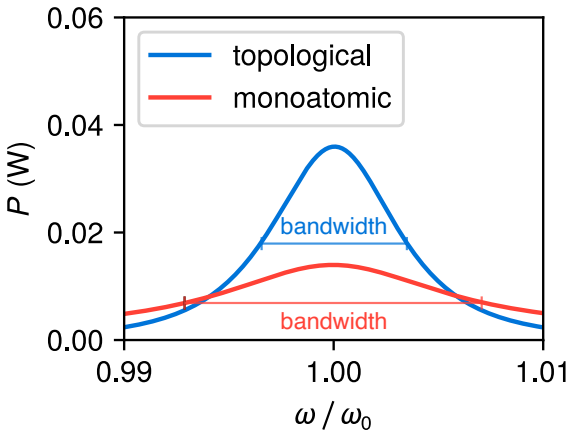


Fig. 4.9: Signal power spectrum for a constant load impedance optimised for maximum signal power at $\omega = \omega_0$. The signal power drops off away from this central operating frequency, with the bandwidth for the monoatomic being slightly higher than the bandwidth for the topological chain.

tems under consideration here, a fixed optimised receiving load, i.e. one that is matched for the central operating frequency, which in this case would optimally be $\omega = \omega_0$ for both the topological and the monoatomic chain. This load is $Z_L = (10 + 0.5j)\ \Omega$ for the topological and $Z_L = (150 - 0.5j)\ \Omega$ for the monoatomic chain. In Figure 4.9, the resulting signal power spectrum is shown. In both cases, the power drops off away from the central operating frequency. The bandwidth is plotted for both cases, indicating that the bandwidth for the monoatomic case is higher than for the topological case, whereas the signal power transmitted by the topological chain exceeds the signal power of the monoatomic chain significantly. Moreover, neither the relative bandwidths nor the signal power enhancement is constant when considering different losses for the individual resonators, i.e. when allowing for a variation in the quality factor Q. As can be seen in Figure 4.10, while the bandwidth advantage of the monoatomic chain is greater for lower Q, this changes as the losses are decreased due to a fairly rapid initial drop in the bandwidth of the monoatomic chain. At the same time, as shown in Figure 4.11, the signal power scales far more favourably with the quality factor for the topological system than for its monoatomic counterpart, leading to an increase in signal power enhancement due to the topological chain when decreasing the losses in the system. The insets show the current profile associated with each chain for a low quality factor as well

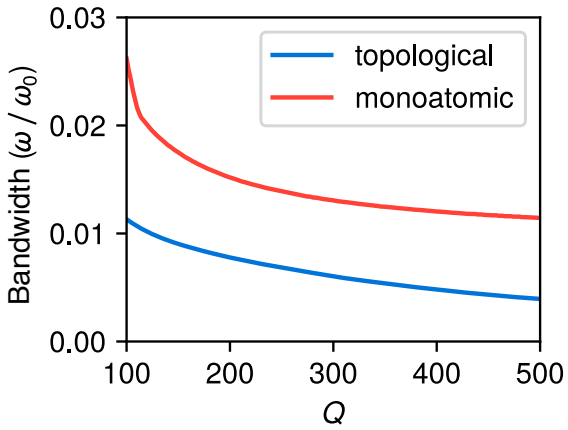


Fig. 4.10: Scaling of the bandwidth with losses. For a low quality factor, i.e. high losses, the bandwidth advantage of the monoatomic chain is larger whereas it shrinks for higher quality factors.

as a high quality factor. While, for the monoatomic chain, the current profile remains flat and thus essentially qualitatively independent from the amount of loss, we can see that for the topological chain, there is a significant increase in current on the receiving element hosting the topological edge state, correspondingly also leading to an increase in signal power.

Hence, as the advantage in terms of the bandwidth lies with the monoatomic chain while the signal power is greater for the topological chain and neither is constant with respect to the losses in the system, it is not yet possible to draw conclusions about their relative performance for wireless communication yet. The relevant figure of merit that is suited to answer this question is the Shannon capacity c. According to the Shannon-Hartley theorem, it derives from both the signal power as well as the bandwidth of a communication system and gives a formalised measure for the information rate which may be transmitted through a the communication channel reliably. In the simplest case, it reads

$$c = B \log_2 \left[1 + \frac{P}{N_0} \right]. \tag{4.17}$$

Here, B is the bandwidth, P the signal power and N_0 is the noise power. This formula holds for a completely flat signal power spectrum and white noise, i.e. no frequency-dependency at all in either P or N_0 for the channel. More generally, this is of course

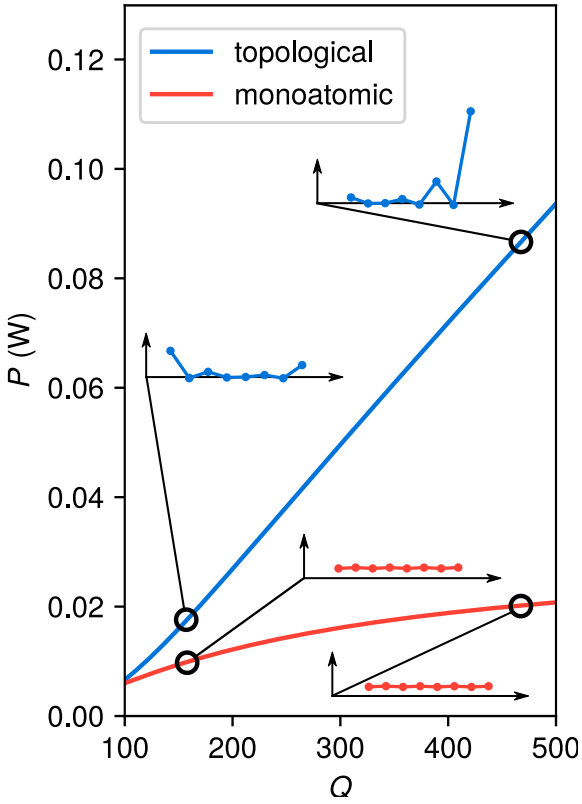


Fig. 4.11: Scaling of the optimum signal power with losses. With an increasing quality factor Q, the topological chain clearly outscales the conventional one, leading to a larger enhancement of the signal power for lower losses in the system. The inset sketches the behaviour of the currents as the quality factor is increased.

not the case, as typically the signal power spectrum may not be flat or the noise may be coloured, meaning both P and N_0 somehow depend on the frequency. This is also the case here, where the signal power spectrum does have a non-negligible dependency on the frequency. However, Equation (4.17) may be generalised by first making the typically valid assumption that when looking at a sufficiently small frequency interval inside the channel, the signal power spectrum looks approximately flat and the noise also becomes frequency-independent. Considering this interval as its own channel of in principle infinitesimal bandwidth $\mathrm{d}\omega$, the infinitesimal Shannon capacity $\mathrm{d}c$ then reads

$$\mathrm{d}c = \log_2\left[1 + \frac{P(\omega)}{N_0}\right]\mathrm{d}\omega. \tag{4.18}$$

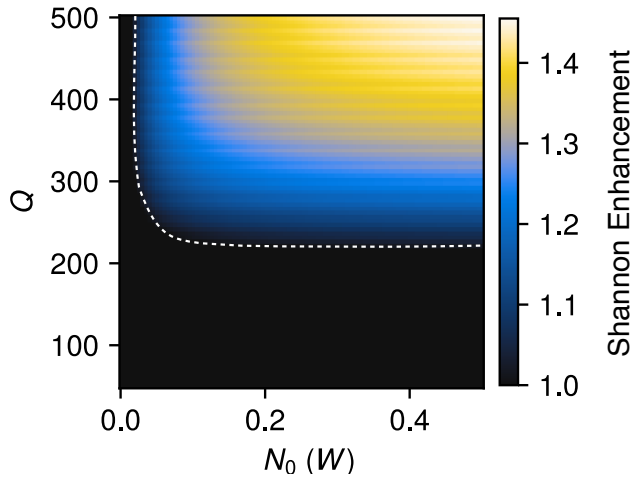


Fig. 4.12: Enhancement of the Shannon capacity by employing the topological chain instead of the conventional monoatomic chain for varying quality factor Q and noise power level N_0 for chains of length $N = 8$. The colour scale is limited with a lower limit of 1, where the Shannon capacity for the topological chain is equal or less than for the monoatomic chain. The dashed line separates the area where the topological chain outperforms the monoatomic chain and *vice versa*.

As the Shannon capacity for multiple channels combined into a wider channel is additive [128], the infinitesimal Shannon capacity can be integrated, which yields

$$c = \int_{\omega_0 - B/2}^{\omega_0 + B/2} \log_2 \left[1 + \frac{P(\omega)}{N_0} \right] \mathrm{d}\omega, \tag{4.19}$$

arriving at a generalised formula for the Shannon capacity with frequency-dependent signal power and noise power.

For the calculation of the Shannon capacity in this work, the noise is assumed to be white, as many dominant sources of noise in metamaterials such as thermal noise are [129]. Correspondingly, the noise level N_0 becomes a constant free parameter quantifying the amount of noise in the channel. As a result, two degrees of freedom remain that may change the Shannon capacity, namely the quality factor and the noise level. In Figure 4.12, the enhancement of the Shannon capacity, i.e. $c_{\text{topological}}/c_{\text{monoatomic}}$ where $c_{\text{topological}}$ and $c_{\text{monoatomic}}$ are the Shannon capacities for the topological and the monoatomic chain, respectively, is shown as a function of quality factor and noise power level. Firstly, it can be seen that below a quality factor of $Q \approx 180$, the Shan-

non capacity is not enhanced. This is to be expected as the power advantage of the topological chain is not significant enough there to make up the bandwidth disadvantage. Secondly, the monoatomic chain performs better also for lower noise power levels. The reason for that is the scaling behaviour of the Shannon capacity that with lower noise power levels c is limited more by the bandwidth than by the signal power. This behaviour in turn favours the conventional monoatomic system. However, for a sufficiently high noise power level and above a certain quality factor, the topological chain is indeed outperforming the conventional chain in terms of the Shannon capacity. The higher the noise or the lower the losses in this regime, the more pronounced this enhancement becomes, ranging in the limits chosen here up to almost 50% enhancement. Correspondingly, this shows that in a regime of high noise and given reasonably though realistically low losses magnetoinductive wave communication links may indeed be improved by employing a topological chain instead of the conventionally used monoatomic one.

4.4 Conclusions

In this chapter, topological wireless communication, i.e. the use of topological edge states of magnetoinductive lines for the purpose of wireless communications was investigated. To this end, the optimised signal power spectrum of a topological, a trivial and a monoatomic chain was studied and compared. It is demonstrated that peak signal power of the topological chain exceeds the peak signal power of the trivial and even the monoatomic chain significantly, in the example studied here by a factor of around 2.5, and that the global maximum of the signal power for all distributions of the coupling coefficient for chains of constant length is indeed due to the topological edge state. Additionally, it is shown that like the conventional monoatomic system, the topological chain also has the desirable property of random accessibility, where the load may be placed flexible on different elements, while maintaining the advantage in signal

power. Moreover, due to the robustness of the topological edge state against disorder in the coupling coefficients, the enhancement of the signal power was also seen to be resistant against this type of perturbation. As the monoatomic chain provides a slightly higher bandwidth than the topological chain but employing the topological chain results in a signal power advantage, the Shannon capacity was studied as the decisive figure of merit for the suitability and performance of a system for wireless communication. Losses have a strong impact on both the bandwidth advantage of the monoatomic chain, which shrinks for higher quality factors, as well as the signal power, for which the topological chain outscales the monoatomic chain resulting in even higher signal power enhancement factors for lower losses. Hence, the Shannon capacity was calculated as a function of both the white noise power level as well as the system losses. Below a threshold of the quality factor, the monoatomic chain provides the higher Shannon capacity mainly due to its increased bandwidth advantage. Additionally, for lower noise power levels the conventional system also performs better as the Shannon capacity becomes limited by the bandwidth and not by the signal power. However, for systems with lower losses in environments with higher noise, the Shannon capacity was seen to be enhanced due to the topological chain by up to about 50%. Hence, in high-noise and low-loss scenarios, topological wireless communication with magnetoinductive links offers an improvement over the conventional monoatomic magnetoinductive line.

5 Topological relay interfaces

In this final chapter, an issue already alluded to in Chapter 4 shall be addressed: the inherent range limitations of topological wireless links. Due to the exponential decay of both the evanescent excitation and the localised mode profile of the topological edge states, the scalability of topological wireless links towards higher element numbers and hence longer transfer ranges is impeded.

In the following a new approach addressing these issues is presented and discussed, namely the introduction of additional topological interfaces acting as relays to counter the range limitation. It will be shown that this method may benefit both topological wireless power transfer as well as topological wireless communications towards larger element numbers and longer transfer distances.

The work shown here also forms part of Refs. [80] and [130].

5.1 Range limitations

As a motivation for the proposal presented in the following sections, a simple study of the scaling behaviour of topological wireless power transfer is quite instructive. To this end, one may calculate the optimal efficiency at $\omega = \omega_0$ and $\omega = 1.07\omega_0$, where the wireless power transfer is due to the topological edge state and due to propagating waves, respectively, versus the length of the link. In the following, realistic fixed parameters are chosen for the resonant frequency $\omega_0 = 10\,\mathrm{MHz}$, the quality factor of $Q = 240$ the inductance of $L = 7\,\mu\mathrm{H}$, as well as the coupling coefficients $\kappa_1 = 0.15$ and $\kappa_2 = 0.3$, though as before all the results presented here can in principle be scaled to different values. As in Chapter 4, where applicable, the transmission distance is held equal to the chain with the aforementioned coupling coefficients according to Equation (4.11). The

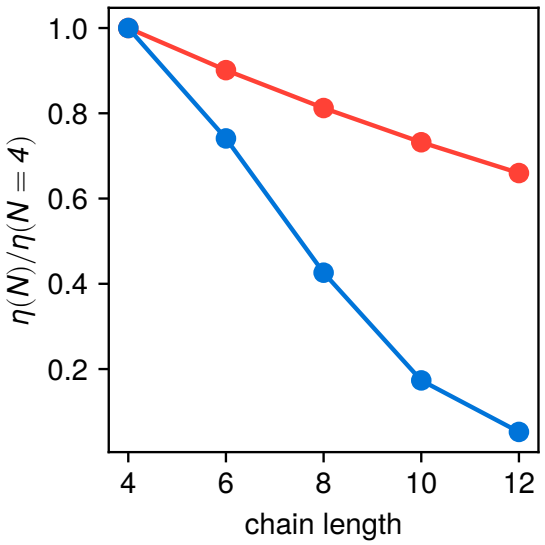


Fig. 5.1: Scaling of the optimised transfer efficiency of topological (blue, $\omega = \omega_0$) and conventional (red, $\omega = 1.07\omega_0$) wireless power transfer with increase in chain length. Clearly, there is a notable decrease in efficiency for longer chains, as the overlap between the exciting current and the asymmetric topological edge state decreases, which imposes a range limitation on this mechanism to construct wireless links.

resulting scaling of the efficiency with the number of elements and thus chain length is shown in Figure 5.1. It can be seen that, as the number of elements in the link is increased, the efficiency of the topological wireless power transfer drops significantly, whereas the efficiency for wireless power transfer using propagating waves drops off less. The reason for this undesirable scaling behaviour is the exponential drop-off of both the excitation and the topological edge state. More formally, the scaling is primarily limited by a vanishing overlap between any excitation exponentially decaying from the left of the structure and the asymmetric edge state on the right edge of the structure, which is exponentially localised on this edge. An illustration of this is shown in Figure 5.2(a). More formally, this can be written down as

$$\lim_{N\to\infty} \sum_{n=1}^{N} (\mathbf{I}_{\text{left}})_n (\mathbf{I}_{\text{right}})_n = 0, \tag{5.1}$$

where $\mathbf{I}_{\text{left}}$ is the excitation current exponentially decaying from the left due to the fact that the operating frequency is in the stopband. The current profile of the asymmet-

ric edge state localised on the right edge of the chain is $\mathbf{I}_{\text{right}}$, which is also exponentially decaying into the bulk from the right. Now, crucially, as the excitation efficiency scales with the magnitude of the overlap of excitation and mode to be excited, it is not possible to excite the growing asymmetric edge state efficiently anymore. Ultimately, this fact translates to the aforementioned limitation in range: Magnetoinductive waveguides designed for longer transmission ranges require an increase in the number elements due to the unfavourable inverse cubic scaling of the coupling coefficient with inter-element distance. Conversely, though, waveguides with too many elements suffer from the vanishing overlap and correspondingly low efficiency in the excitation of the growing asymmetric topological edge state localised at the end of the line. Because of this, the range of topological wireless links as discussed in the previous chapters is inherently limited.

5.2 Topological interfaces as relays

To overcome the limitation imposed by the finite localisation length of the topological edge states, it is instructive to note the similarity to an issue in the early day of near field wireless power transfer: In the initial proposals for wireless power transfer based on magnetic coupling [90], two resonators were coupled using their magnetic near fields. Just like the profile of the topological edge state, these near fields also decay exponentially and their overlap strongly influences the coupling efficiency. The solution are magnetoinductive waveguides, or in very plain terms, the addition of passive relay resonators, which serve as intermediate points between the excitation and the field of the resonator with the receiving load. The relay resonators are closer to either the excited resonator or the previous relay resonator and thus enable a far greater overlap of their magnetic fields. Hence, the effective coupling between the excitation and the load may be increased as the bottleneck of vanishing overlap would be removed by the introduction of the relay resonators. The sketches in Figure 5.2(a) visualise this. One may

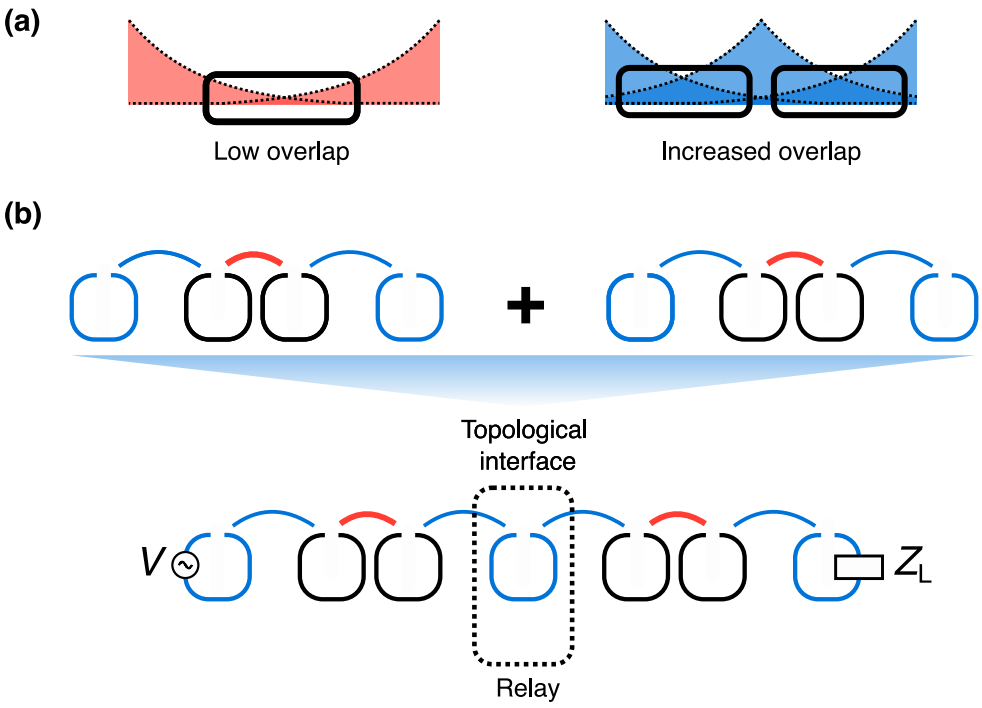


Fig. 5.2: **(a):** Illustration of the vanishing overlap for exponentially decaying mode profiles (left). The overlap may be increased by the introduction of a relay mode (right). **(b):** Sketch of the construction of a topological diatomic magnetoinductive waveguide with a topological relay interface.

now think how to apply this concept to topological wireless links: Instead of just relying on the coupling between the excitation and a distant asymmetric topological edge state, it is possible to introduce one or more additional interfaces hosting topological modes. Just like the relay resonators in the previous example, they serve as relay resonances providing a significantly increased overlap to either the previous topological mode or to the excitation. By virtue of these increased overlaps, the effective coupling to the edge state localised on the receiving load may be improved. Interfaces that host topological edge states may be constructed from two (or more) topological chains of some length by taking the last element of one chain and using it as the first element of the next chain, as illustrated in Figure 5.2(b). As a result, an element is introduced with weak couplings to both its neighbours. Said element hosts a topological edge state, as it constitutes an interface between a topologically trivial and a topologically non-trivial phase. This is the case because, if the element is included with one of the chains, this

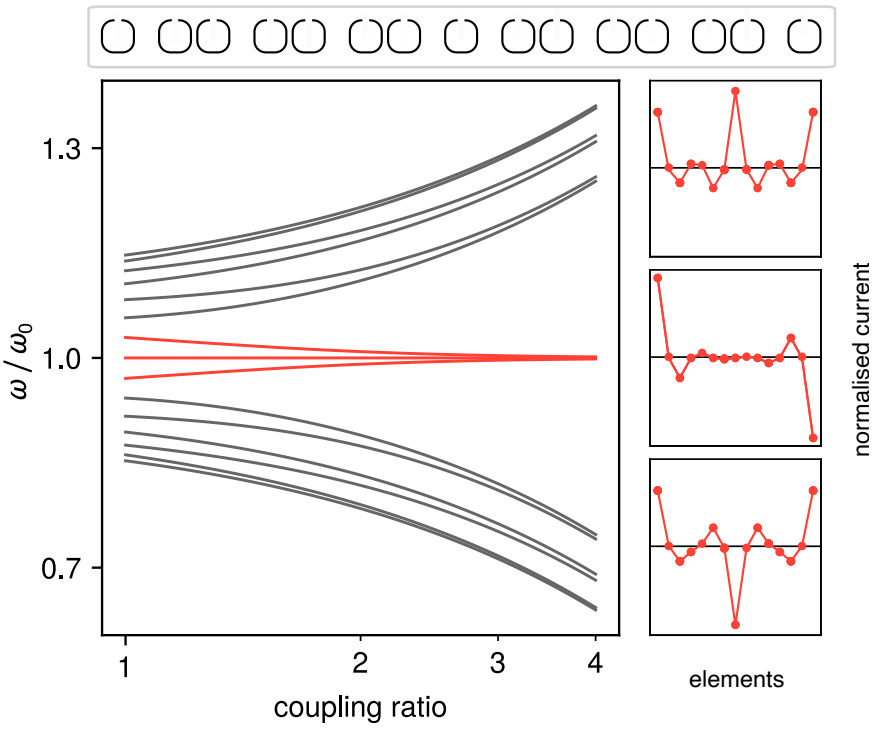


Fig. 5.3: Resonances of a topological magnetoinductive waveguide ($N = 15$) with a topological relay interface at its centre for varying coupling ratio κ_2/κ_1. The three eigenmodes highlighted in red belong to the topological edge states and the topological relay resonance localised at the interface. Its presence is confirmed by the current profiles belonging to these eigenmodes, as shown on the right where a high current amplitude at the interface on element 8 is clearly visible.

chain looks like the topologically non-trivial chain with a weakly coupled last element, whereas the other chain has a strongly coupled first element and is thus looks topologically trivial. In Figure 5.3, the resonances of a magnetoinductive line with a topological relay interface are shown as a function of the coupling ratio κ_2/κ_1. Clearly, most resonances are grouping into passbands again, with three of them remaining separate inside the stopband around the resonant frequency ω_0, suggesting the potential presence of topological resonances. The current profiles of these eigenmodes are shown on the right in Figure 5.3. For the central mode ($\omega = \omega_0$), there is an antisymmetric edge state at the interface, which immediately implies a solution with zero current at the interface. However, for the current profiles for the higher and for the lower of the resonant modes shown in red, there is a high amplitude at the interface belonging to a symmetric topological resonance localised there as desired.

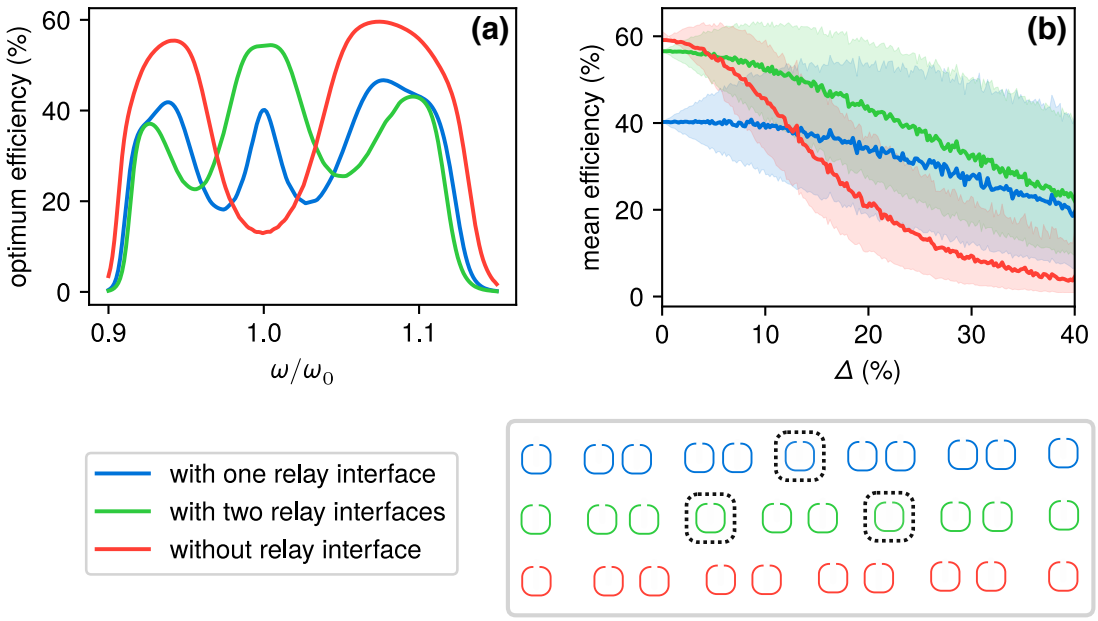


Fig. 5.4: **(a):** Optimum wireless power transfer efficiency spectrum for topological diatomic magnetoinductive lines without, with one and with two relay interfaces. **(b):** Impact of disorder on power transfer efficiencies for propagating waves in a line without relay interfaces (at $\omega \approx 1.07\omega_0$) and for topological wireless power transfer in the lines with relay interfaces (at $\omega = \omega_0$). The illustrations of the chains show the location of the relay interfaces (dotted line). The sketched distances of the resonators are not to scale.

5.3 Topological wireless links with relay interfaces

With the concept of using topological interfaces as relays in mind, this section will revisit some of the aspects of the previous chapters to investigate the use of topological relay interfaces in the application of both wireless power transfer and wireless communications.

5.3.1 Wireless power transfer

First, the usefulness of topological relay interfaces for the purpose of topological wireless power transfer shall be investigated. The relevant figure of merit is the power transfer efficiency as defined in Equation (3.7). As in Chapter 3, the optimal

load impedance to achieve the maximum possible efficiency may be determined numerically. The resulting efficiency is shown in Figure 5.4(a). For the case of topological wireless power transfer without relay interfaces, it can clearly be seen that the increased length of the structure at $N = 10$ leads to a notable decrease in efficiency in comparison to the case of $N = 6$ considered in Chapter 3, meaning that where the stopband transfer efficiency used to be comparable to its conventional counterpart relying on propagating waves, it is now quite significantly less efficient. With the addition of a topological relay interface, however, the transfer efficiency in the stopband recovers noticeably to a level comparable with power transfer based on propagating waves, despite the fact that the chains with relay interfaces contain an additional element. Hence, for the purpose of topological wireless power transfer it is clearly advantageous to introduce relay interfaces. Furthermore, Figure 5.4(b) shows the impact of coupling coefficient disorder as introduced in Section 3.3.3. Specifically, the mean efficiency with its semideviations is shown for the frequency with the largest efficiency in the case without disorder, i.e. for propagating waves in the passband ($\omega \approx 1.07\omega_0$), in the case without a relay interface and the topological resonances in the stopband at $\omega = \omega_0$ in the cases with one or two relay interfaces. While the propagating waves are initially the most efficient way to transfer power, for larger disorder strengths Δ the topological wireless power transfer using relay interfaces becomes more efficient, implying that as expected the benefits of topological protection persist for the power transfer efficiency through magnetoinductive waveguides with relay interfaces.

5.3.2 Wireless communication

With a view of using topological modes for the purpose of wireless communication, the signal power as a key figure of merit may be revisited. Its definition is given in Equation (4.7). With numerically determined matching impedances, the optimised power spectrum may be calculated. It is shown in Figure 5.5 for the same three scenarios as in Figure 5.4. Firstly, opposed to the case of topological wireless power transfer,

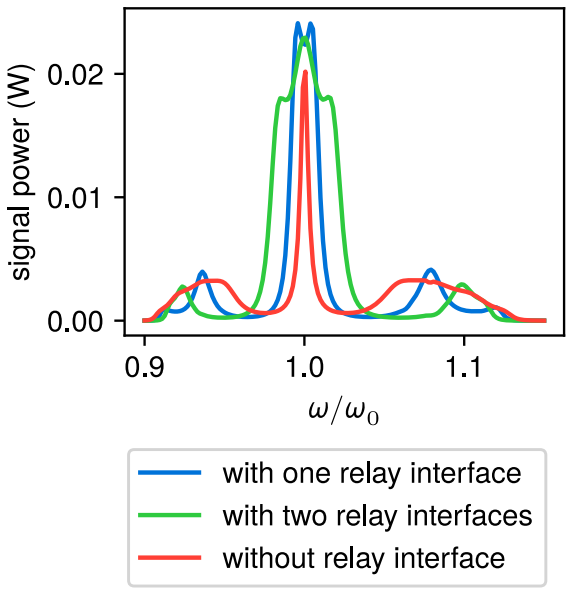


Fig. 5.5: Optimum signal power spectrum for topological diatomic magnetoinductive lines without, with one and with two relay interfaces.

the peak power spike around the resonant frequency which is due to the fact that topological edge states is still well pronounced even in the case without a relay interface. It should be noted that why exactly the signal power is less affected by the vanishing overlap than the efficiency is an open question. Nonetheless, the introduction of one or two relay interfaces is still advantageous and results in an increase in the maximum signal power. It should be noted that due to the symmetry of the chain in the case of one relay interface, or more generally an odd number of relay interfaces, there is a split in the central signal power peak, resulting in a slight shift of the maximum signal power away from the resonant frequency ω_0. However, in both cases considered, with one and with two relay interfaces, the signal power at the resonant frequency benefits from the introduction of relay interfaces improving the signal power enhancement and hence the applicability of topological wireless communication.

5.4 Conclusions

In this chapter, the concept of topological relay interfaces was introduced and analysed. Due to the vanishing overlap between excitation current and the eigenmode profile of the asymmetric edge state, the efficiency and signal power for topological wireless links scales badly with an increase in the number of elements and hence larger transfer distances. By introducing additional topological interfaces, the modes that are localised at these interfaces may be used as relays due to their greater overlap with the excitation, the edge state on the load impedance as well as each other. Hence, the coupling between excitation and load can effectively be increased.

It was shown that, for topological wireless power transfer, the introduction of topological relay interfaces to a longer chain leads to a recovery of the efficiency in the stopband, which was diminished for a chain without relay interfaces, to a level once again comparable to wireless power transfer in the passband. Additionally, the impact of coupling coefficient disorder on the efficiency was investigated for both topological and conventional wireless power transfer based on propagating waves. It was demonstrated that due to the topological protection, the efficiency remains robust against such disorder.

Furthermore, for the purpose of topological wireless communication, the signal power spectrum was studied with and without employing topological relay interfaces. While the impact of the increased chain length was less critical than in the case of wireless power transfer, the signal power was still increased by the introduction of relay interfaces, suggesting that their use is also beneficial to magnetoinductive lines used for wireless communication.

Overall, in this chapter, topological relay interfaces were proposed as a new design tool for wireless links and shown to be a useful addition to the toolbox for the design of topological magnetoinductive wireless links for applications both in wireless power transfer and wireless communications.

6 Conclusions & Outlook

The field of topological physics and its rich phenomenology has grown rapidly in recent times. Aided by the advances in the design and fabrication of electromagnetic metamaterials a plethora of avenues for employing topological effects to engineer the properties and behaviour of electromagnetic waves have opened. Despite great promise, particularly in the radio frequency and microwave regime most of the progress so far was of fundamental nature rather than focused on engineering challenges, with those often being confined to qualitative outlooks. To address this, this thesis has investigated topological metamaterials, specifically topological magnetoinductive metamaterials, with a focus on engineering applications in the radio and microwave frequency ranges.

To briefly recapitulate, Chapter 1 offered an introductory look at the fundamentals of metamaterials and topological physics. Based on this, Chapter 2 unearthed the topological properties of magnetoinductive metamaterials by establishing a link between magnetoinductive wave theory and quantum theory. A magnetoinductive metamaterial equivalent to the Su-Schrieffer-Heeger model was investigated, deriving its topological invariant as well as proving that it may host topological edge states. Future work will likely focus on extending the range of topological models studied in magnetoinductive metamaterials. Progress in the realm of topological physics has been vast, with more complex but also richer topological models found, for examples by increasing the dimensionality of the structure leading to propagating edge states [3] and higher-order topology [131], applying time modulations introducing Floquet topology [132] or, most recently, adding gain and loss to the system to arrive at non-Hermitian topology [133]. On the one hand, there is still plenty of fundamental research to be carried out in this direction, where magnetoinductive metamaterials may provide a platform for the implementation of novel topological models. On the other hand, more complex topological models may also provide additional benefits to the applications of wireless

power and communication discussed here as well as unlock further options for novel applications. For instance, non-Hermitian topological structures have been discussed as candidates for highly sensitive sensors, whose sensitivity grows exponentially with the size of the structure [10], which may enable a new class of microwave sensing devices based on non-Hermitian topological magnetoinductive metamaterials.

In Chapter 3, the concept of topological wireless power transfer was introduced, showcasing how the topological properties of magnetoinductive waves may be harnessed to benefit wireless power transfer systems. It was found that topological wireless power transfer is efficient and, compared to its conventional counterpart based on propagating waves, offers superior robustness against external disorder and results in a significant decrease in electromagnetic pollution. Continuing in this direction, a worthwhile extension of this study would be to go from one-dimensional to two-dimensional metamaterials. Magnetoinductive waves in particular have been shown to allow for efficient power transfer in such settings, enabling the construction of charging mats [134]. It would be very interesting to see if topology can offer any benefits here. As power routing is an important task in these higher-dimensional applications, it seems possible that a topological waveguide could be employed to improve it, although this would probably require an active component allowing a switching between two topological phases to move the topological interface guiding the wave on demand. Additionally, even for one-dimensional power transfer, stepping beyond one dimension could be of use, as quasi-one-dimensional structures, e.g. ribbons of a two-dimensional metamaterials, would support propagating topological edge states [8], though the question whether the increased loss and cost introduced by the use of additional elements in this setting would need to be addressed. Furthermore, on a more technical side, it would also be appealing to see if more complex magnetoinductive devices, such as power splitters or directional couplers [48], could benefit from employing topological resonances to transfer power. In terms of experimental future work, while works following the publication of the results in this thesis [77] have presented important proof-of-principle

experiments [16, 97, 100], a more in-depth study with the aim of optimising the experimental parameters as well as implementations of the aforementioned advancements of the concept of topological wireless power transfer would be highly worthwhile. A key challenge for such experiments is the fabrication of resonators with well-controlled resonant frequencies and low losses, an avenue in which progress was made recently by utilising low-loss filaments to 3D print substrates for highly repeatable manufacturing of capacitively loaded coils [135].

Chapter 4 applied the topological physics of magnetoinductive metamaterials to wireless communication. It was demonstrated that topological wireless communication does indeed offer advantages over conventional magnetoinductive communication links operating using propagating waves. Specifically, it allows for a strong enhancement in signal power and, in scenarios with sufficiently low loss and high noise, a significant increase in the Shannon capacity of the channel. Further investigations could generalise this approach from a single channel to multiple channels by employing elements with multiple resonances coupled together leading to additional edge states at other frequencies. Such an extension would enable a further increase of the amount of information that could be transferred through the link. Alternatively, instead of elements with multiple resonances a time modulation could also be implemented, as periodically driven systems with edge states would also exhibit higher harmonic copies of these, which could allow for the implementation of multiple channels. For an extension of the model to for example the aforementioned driven systems or non-Hermitian topological systems, it would be interesting to see how the noise introduced by such external drives would modify the performance of the system as a communication link. Lastly, the high powers involved in the topological link may suggest the possibility of introducing nonlinearities potentially allowing for the engineering of a self-tuning mechanism, which may help with impedance matching. Besides the aforementioned routes to advance topological wireless communication conceptually, ultimately an experimental implementation of the approach is highly important. While an experimental platform

is available [116], particularly a verification of measures such as the transmission rate would require additional work. As the Shannon capacity discussed in this thesis constitutes a theoretical limit to the information rate that may be reliably transmitted through a channel, further details such as optimal encoding scheme would have to be fleshed out to enable a full experimental study of a topological wireless communication channel.

In Chapter 5, the range limitations of topological wireless links were discussed and addressed by the introduction of topological relay interfaces. It was demonstrated that the impact of the vanishing overlap limiting the scalability of both topological wireless communication as well as power transfer may be successfully mitigated that way. Next steps in this direction may consider topological relay interfaces at different spacings as opposed to the examples with equal spacings considered here, introducing an additional degree of freedom which would need to be optimised. Perhaps a general rule which configurations are best for which parameters of the wireless link can be found. Such an endeavour may prove highly interesting even beyond the appeal for the applications shown here, as different effective couplings between the topological states localised at these interfaces would lead to a dispersion of the interface states. With sufficiently many interfaces, a band of interface states would form inside stopband, which itself could be investigated and engineered. On a more technical side, beyond the optimisation of the spacings of the interfaces, additional degrees of freedoms such as the quality factors, the coupling coefficients or others have also not been chosen optimally yet. Ultimately, such an optimisation task is a high-dimensional problem and machine learning algorithms may provide a promising approach to finding a globally optimal solution in scenarios where conventional algorithms are likely to fail. An experimental investigation of topological relay interfaces is within close reach, as the experimental toolkit is available [58, 60, 72] and should be readily adaptable to realise topological chains with relay interfaces, though particularly for longer chains with multiple relay interfaces minimising the loss of the resonators will be an important task.

In conclusion, this thesis has shown the very concrete benefits that topological physics holds for applications, specifically for applications in the radio and microwave frequency regimes. Nonetheless, this is only the beginning of the journey of realising the full potential of topological physics, which itself is still progressing at high speed, with a plethora of promising research avenues wide open, only some of them mentioned in this outlook, and many more waiting to be discovered.

Bibliography

[1]J. K. Asbóth, L. Oroszlány, and A. Pályi, "A short course on topological insulators", Lecture Notes in Physics **919**, 166 (2016) (cit. on pp. 1, 47–49).

[2]S. Raghu and F. D. M. Haldane, "Analogs of quantum-hall-effect edge states in photonic crystals", Physical Review A **78**, 033834 (2008) (cit. on p. 1).

[3]Z. Wang, Y. Chong, J. D. Joannopoulos, and M. Soljačić, "Observation of unidirectional backscattering-immune topological electromagnetic states", Nature **461**, 772–775 (2009) (cit. on pp. 1, 105).

[4]L. Lu, J. D. Joannopoulos, and M. Soljačić, "Topological photonics", Nature Photonics **8**, 821–829 (2014) (cit. on p. 1).

[5]T. Ozawa, H. M. Price, A. Amo, N. Goldman, M. Hafezi, L. Lu, M. C. Rechtsman, D. Schuster, J. Simon, O. Zilberberg, et al., "Topological photonics", Reviews of Modern Physics **91**, 015006 (2019) (cit. on pp. 1, 28, 48).

[6]M. Bandres, S. Wittek, G. Harari, M. Parto, J. Ren, M. Segev, D. Christodoulides, and M. Khajavikhan, "Topological insulator laser: experiments", Science **359**, eaar4005 (2018) (cit. on p. 1).

[7]Y. Gong, S. Wong, A. J. Bennett, D. L. Huffaker, and S. S. Oh, "Topological insulator laser using valley-hall photonic crystals", ACS Photonics **7**, 2089–2097 (2020) (cit. on p. 1).

[8]M. Hafezi, E. A. Demler, M. D. Lukin, and J. M. Taylor, "Robust optical delay lines with topological protection", Nature Physics **7**, 907–912 (2011) (cit. on pp. 1, 49, 106).

[9]C. He, X. Ni, H. Ge, X.-C. Sun, Y.-B. Chen, M.-H. Lu, X.-P. Liu, and Y.-F. Chen, "Acoustic topological insulator and robust one-way sound transport", Nature Physics **12**, 1124–1129 (2016) (cit. on p. 1).

[10]J. C. Budich and E. J. Bergholtz, "Non-Hermitian topological sensors", Physical Review Letters **125**, 180403 (2020) (cit. on pp. 1, 106).

[11] V. Peri, Z.-D. Song, M. Serra-Garcia, P. Engeler, R. Queiroz, X. Huang, W. Deng, Z. Liu, B. A. Bernevig, and S. D. Huber, "Experimental characterization of fragile topology in an acoustic metamaterial", Science **367**, 797–800 (2020) (cit. on p. 1).

[12] J. C. Maxwell, *A Treatise on Electricity and Magnetism*, Vol. 1 (Clarendon Press, 1873) (cit. on p. 3).

[13] L. Rayleigh, "LVI. on the influence of obstacles arranged in rectangular order upon the properties of a medium", The London, Edinburgh, and Dublin Philosophical Magazine and Journal of Science **34**, 481–502 (1892) (cit. on p. 3).

[14] V. G. Veselago, "The electrodynamics of substances with simultaneously negative values of ε and μ", Soviet Physics Uspekhi **10**, 509 (1968) (cit. on p. 3).

[15] R. A. Shelby, D. R. Smith, and S. Schultz, "Experimental verification of a negative index of refraction", Science **292**, 77–79 (2001), (Top left image in Figure 1.1(b) used with permission of the AAAS, from this reference; permission conveyed through Copyright Clearance Center, Inc.) (Cit. on pp. 4, 6).

[16] Y. Yang, Z. Gao, H. Xue, L. Zhang, M. He, Z. Yang, R. Singh, Y. Chong, B. Zhang, and H. Chen, "Realization of a three-dimensional photonic topological insulator", Nature **565**, 622–626 (2019), (Top centre image in Figure 1.1(b) reproduced from this reference with permission from Springer Nature.) (Cit. on pp. 4, 107).

[17] J. K. Gansel, M. Thiel, M. S. Rill, M. Decker, K. Bade, V. Saile, G. von Freymann, S. Linden, and M. Wegener, "Gold helix photonic metamaterial as broadband circular polarizer", Science **325**, 1513–1515 (2009), (Top right image in Figure 1.1(b) used with permission of the AAAS, from this reference; permission conveyed through Copyright Clearance Center, Inc.) (Cit. on p. 4).

[18] M. Khorasaninejad, W. T. Chen, R. C. Devlin, J. Oh, A. Y. Zhu, and F. Capasso, "Metalenses at visible wavelengths: diffraction-limited focusing and subwavelength resolution imaging", Science **352**, 1190–1194 (2016), (Bottom left image in Figure 1.1(b) used with permission of the AAAS, from this reference; permission conveyed through Copyright Clearance Center, Inc.) (Cit. on p. 4).

[19] A. J. Kollár, M. Fitzpatrick, and A. A. Houck, "Hyperbolic lattices in circuit quantum electrodynamics", Nature **571**, 45–50 (2019), (Bottom centre image in Figure 1.1(b) reproduced from this reference with permission from Springer Nature.) (Cit. on p. 4).

[20] T. Frenzel, M. Kadic, and M. Wegener, "Three-dimensional mechanical metamaterials with a twist", Science **358**, 1072–1074 (2017), (Bottom right image in Figure 1.1(b) used with permission of the AAAS, from the cover of this reference; permission conveyed through Copyright Clearance Center, Inc.) (Cit. on p. 4).

[21] D. R. Smith, "Analytic expressions for the constitutive parameters of magnetoelectric metamaterials", Physical Review E **81**, 036605 (2010) (cit. on p. 5).

[22]A. Alù, "First-principles homogenization theory for periodic metamaterials", Physical Review B **84**, 075153 (2011) (cit. on p. 5).

[23]L. D. Landau, E. M. Lifšic, L. P. Pitaevskij, and L. D. Landau, *Electrodynamics of Continuous Media*, Course of Theoretical Physics 8 (Elsevier Butterworth-Heinemann, 2009) (cit. on pp. 5, 11, 12).

[24]N. Engheta and R. W. Ziolkowski, *Metamaterials: Physics and Engineering Explorations* (John Wiley & Sons, 2006) (cit. on pp. 5, 6).

[25]K. Mnasri, A. Khrabustovskyi, C. Stohrer, M. Plum, and C. Rockstuhl, "Beyond local effective material properties for metamaterials", Physical Review B **97**, 075439 (2018) (cit. on p. 5).

[26]J. Feis, K. Mnasri, A. Khrabustovskyi, C. Stohrer, M. Plum, and C. Rockstuhl, "Surface plasmon polaritons sustained at the interface of a nonlocal metamaterial", Physical Review B **98**, 115409 (2018) (cit. on p. 5).

[27]J. B. Pendry, "Negative refraction makes a perfect lens", Physical Review Letters **85**, 3966 (2000) (cit. on p. 5).

[28]E. Shamonina, V. Kalinin, K. Ringhofer, and L. Solymar, "Magneto-inductive waveguide", Electronics Letters **38**, 371–373 (2002) (cit. on pp. 6, 17).

[29]C. Enkrich, M. Wegener, S. Linden, S. Burger, L. Zschiedrich, F. Schmidt, J. Zhou, T. Koschny, and C. Soukoulis, "Magnetic metamaterials at telecommunication and visible frequencies", Physical Review Letters **95**, 203901 (2005) (cit. on p. 6).

[30]S. A. Cummer, J. Christensen, and A. Alù, "Controlling sound with acoustic metamaterials", Nature Reviews Materials **1**, 1–13 (2016) (cit. on p. 6).

[31]E. Barchiesi, M. Spagnuolo, and L. Placidi, "Mechanical metamaterials: a state of the art", Mathematics and Mechanics of Solids **24**, 212–234 (2019) (cit. on p. 6).

[32]P. Alitalo and S. Tretyakov, "Electromagnetic cloaking with metamaterials", Materials Today **12**, 22–29 (2009) (cit. on p. 6).

[33]T. Chen, S. Li, and H. Sun, "Metamaterials application in sensing", Sensors **12**, 2742–2765 (2012) (cit. on p. 6).

[34]W. J. Padilla and R. D. Averitt, "Imaging with metamaterials", Nature Reviews Physics **4**, 85–100 (2022) (cit. on p. 6).

[35]K. Sun, R. Fan, X. Zhang, Z. Zhang, Z. Shi, N. Wang, P. Xie, Z. Wang, G. Fan, H. Liu, et al., "An overview of metamaterials and their achievements in wireless power transfer", Journal of Materials Chemistry C **6**, 2925–2943 (2018) (cit. on p. 6).

[36]E. Brookner, "Metamaterial advances for radar and communications", in CIE International Conference on Radar (RADAR) (IEEE, 2016), pp. 1–8 (cit. on p. 6).

[37]N. I. Zheludev and Y. S. Kivshar, "From metamaterials to metadevices", Nature Materials **11**, 917–924 (2012) (cit. on p. 6).

[38]M. Wiltshire, E. Shamonina, I. Young, and L. Solymar, "Dispersion characteristics of magneto-inductive waves: comparison between theory and experiment", Electronics Letters **39**, 1 (2003) (cit. on p. 6).

[39]M. Wiltshire, E. Shamonina, I. Young, and L. Solymar, "Experimental and theoretical study of magneto-inductive waves supported by one-dimensional arrays of 'Swiss Rolls'", Journal of Applied Physics **95**, 4488–4493 (2004) (cit. on p. 6).

[40]O. Zhuromskyy, E. Shamonina, and L. Solymar, "Effect of radiation on dispersion of magneto-inductive waves in a metamaterial", in Proc. SPIE 5955 (Metamaterials) (SPIE, 2005), pp. 48–55 (cit. on pp. 6, 11).

[41]H. Liu, D. Genov, D. Wu, Y. Liu, J. Steele, C. Sun, S. Zhu, and X. Zhang, "Magnetic plasmon propagation along a chain of connected subwavelength resonators at infrared frequencies", Physical Review Letters **97**, 243902 (2006) (cit. on p. 6).

[42]G. Dolling, C. Enkrich, M. Wegener, C. M. Soukoulis, and S. Linden, "Low-loss negative-index metamaterial at telecommunication wavelengths", Optics Letters **31**, 1800–1802 (2006) (cit. on p. 6).

[43]E. Shamonina, V. Kalinin, K. Ringhofer, and L. Solymar, "Magnetoinductive waves in one, two, and three dimensions", Journal of Applied Physics **92**, 6252–6261 (2002) (cit. on pp. 7, 13).

[44]C. J. Stevens, "Magnetoinductive waves and wireless power transfer", IEEE Transactions on Power Electronics **30**, 6182–6190 (2014) (cit. on pp. 7, 53, 55, 63, 84).

[45]C. J. Stevens, C. W. Chan, K. Stamatis, and D. J. Edwards, "Magnetic metamaterials as 1-d data transfer channels: an application for magneto-inductive waves", IEEE Transactions on Microwave Theory and Techniques **58**, 1248–1256 (2010) (cit. on pp. 7, 75, 76).

[46]C. W. Chan and C. J. Stevens, "Two-dimensional magneto-inductive wave data structures", in Proceedings of the 5th European Conference on Antennas and Propagation (EUCAP) (IEEE, 2011), pp. 1071–1075 (cit. on pp. 7, 56, 75, 76).

[47]E. Shamonina and L. Solymar, "Magneto-inductive waves supported by metamaterial elements: components for a one-dimensional waveguide", Journal of Physics D: Applied Physics **37**, 362 (2004) (cit. on p. 7).

[48]R. Syms, E. Shamonina, and L. Solymar, "Magneto-inductive waveguide devices", IEE Proceedings - Microwaves, Antennas and Propagation **153**, 111–121 (2006) (cit. on pp. 7, 55, 106).

[49]E. Shamonina and L. Solymar, "Superdirective 'meta-molecules'", in 8th International Congress on Advanced Electromagnetic Materials in Microwaves and Optics (IEEE, 2014), pp. 268–270 (cit. on p. 7).

[50]A. Radkovskaya, S. Kiriushechkina, A. Vakulenko, P. Petrov, L. Solymar, L. Li, A. Vallecchi, C. Stevens, and E. Shamonina, "Superdirectivity from arrays of strongly coupled meta-atoms", Journal of Applied Physics **124** (2018) (cit. on p. 7).

[51]J. Yan, C. Stevens, and E. Shamonina, "A metamaterial position sensor based on magnetoinductive waves", IEEE Open Journal of Antennas and Propagation **2**, 259–268 (2021) (cit. on p. 7).

[52]F. J. Herraiz-Martínez, J. Martínez-Cebrián, and D. Segovia-Vargas, "A passive temperature sensor based on a printed magnetoinductive-wave (MIW) delay line", in 2015 European Microwave Conference (EuMC) (IEEE, 2015), pp. 263–266 (cit. on p. 7).

[53]R. Syms, T. Floume, I. Young, L. Solymar, and M. Rea, "Flexible magnetoinductive ring mri detector: design for invariant nearest-neighbour coupling", Metamaterials **4**, 1–14 (2010) (cit. on p. 7).

[54]R. Syms, I. Young, M. Ahmad, and M. Rea, "Magnetic resonance imaging using linear magneto-inductive waveguides", Journal of Applied Physics **112** (2012) (cit. on p. 7).

[55]X. Fu, X. Zeng, T. J. Cui, C. Lan, Y. Guo, H. C. Zhang, and Q. Zhang, "Mode jumping of split-ring resonator metamaterials controlled by high-permittivity BST and incident electric fields", Scientific Reports **6**, 1–9 (2016), (Left panel of Figure 1.2(b) reproduced from this reference. This work is licensed under CC BY 4.0.) (Cit. on p. 7).

[56]S. Keren-Zur, M. Tal, S. Fleischer, D. M. Mittleman, and T. Ellenbogen, "Generation of spatiotemporally tailored terahertz wavepackets by nonlinear metasurfaces", Nature Communications **10**, 1778 (2019), (Right panel of Figure 1.2(b) reproduced from this reference. This work is licensed under CC BY 4.0.) (Cit. on p. 7).

[57]M. Gorkunov, M. Lapine, E. Shamonina, and K. Ringhofer, "Effective magnetic properties of a composite material with circular conductive elements", The European Physical Journal B - Condensed Matter and Complex Systems **28**, 263–269 (2002) (cit. on p. 9).

[58]A. Radkovskaya, M. Shamonin, C. J. Stevens, G. Faulkner, D. J. Edwards, E. Shamonina, and L. Solymar, "An experimental study of the properties of magnetoinductive waves in the presence of retardation", Journal of Magnetism and Magnetic Materials **300**, 29–32 (2006) (cit. on pp. 9, 108).

[59]E. Tatartschuk, N. Gneiding, F. Hesmer, A. Radkovskaya, and E. Shamonina, "Mapping inter-element coupling in metamaterials: scaling down to infrared", Journal of Applied Physics **111** (2012) (cit. on p. 9).

[60]S. Chu, M. S. Luloff, J. Yan, P. Petrov, C. J. Stevens, and E. Shamonina, "Magnetoinductive waves in attenuating media", Scientific Reports **11**, 7679 (2021), (Figure 4.1(a) reproduced from this reference. This work is licensed under CC BY 4.0.) (Cit. on pp. 11, 76, 81, 108).

[61]C. A. Balanis, *Antenna Theory: Analysis and Design* (Wiley, 2016) (cit. on pp. 11, 81).

[62]L. Solymar and E. Shamonina, *Waves in Metamaterials* (Oxford University Press, 2009) (cit. on pp. 11, 58, 81).

[63]H. Ibach and H. Lüth, *Solid-State Physics: An Introduction to Principles of Materials Science* (Springer, 2009) (cit. on pp. 13, 49).

[64]O. Sydoruk, A. Radkovskaya, O. Zhuromskyy, E. Shamonina, M. Shamonin, C. J. Stevens, G. Faulkner, D. J. Edwards, and L. Solymar, "Tailoring the near-field guiding properties of magnetic metamaterials with two resonant elements per unit cell", Physical Review B **73**, 224406 (2006) (cit. on p. 13).

[65]J. R. Munkres, *Topology: a First Course* (Prentice-Hall, 1975) (cit. on pp. 18, 19).

[66]M. Suddards, A. Baumgartner, M. Henini, and C. J. Mellor, "Scanning capacitance imaging of compressible and incompressible quantum hall effect edge strips", New Journal of Physics **14**, 083015 (2012) (cit. on p. 27).

[67]K. v. Klitzing, G. Dorda, and M. Pepper, "New method for high-accuracy determination of the fine-structure constant based on quantized hall resistance", Physical Review Letters **45**, 494 (1980) (cit. on p. 26).

[68]D. J. Thouless, M. Kohmoto, M. P. Nightingale, and M. den Nijs, "Quantized hall conductance in a two-dimensional periodic potential", Physical Review Letters **49**, 405 (1982) (cit. on p. 27).

[69]M. J. Gilbert, "Topological electronics", Communications Physics **4**, 70 (2021) (cit. on p. 28).

[70]H. Xue, Y. Yang, and B. Zhang, "Topological acoustics", Nature Reviews Materials **7**, 974–990 (2022) (cit. on p. 28).

[71]M. Z. Hasan and C. L. Kane, "Colloquium: topological insulators", Reviews of Modern Physics **82**, 3045 (2010) (cit. on p. 28).

[72]P. Zhang, H. Shen, and H. Zhai, "Machine learning topological invariants with neural networks", Physical Review Letters **120**, 066401 (2018) (cit. on pp. 28, 108).

[73]A. Altland and M. R. Zirnbauer, "Nonstandard symmetry classes in mesoscopic normal-superconducting hybrid structures", Physical Review B **55**, 1142 (1997) (cit. on p. 30).

[74]C.-K. Chiu, J. C. Teo, A. P. Schnyder, and S. Ryu, "Classification of topological quantum matter with symmetries", Reviews of Modern Physics **88**, 035005 (2016) (cit. on p. 30).

[75]R. Roy and F. Harper, "Periodic table for Floquet topological insulators", Physical Review B **96**, 155118 (2017) (cit. on p. 31).

[76]K. Kawabata, K. Shiozaki, M. Ueda, and M. Sato, "Symmetry and topology in non-Hermitian physics", Physical Review X **9**, 041015 (2019) (cit. on p. 31).

[77]J. Feis, C. Stevens, and E. Shamonina, "Wireless power transfer through asymmetric topological edge states in diatomic chains of coupled meta-atoms", Applied Physics Letters **117** (2020) (cit. on pp. 33, 53, 75, 106).

[78]J. Feis, L. Solymar, and E. Shamonina, "Wireless links via coupled topological edge states", in Sixteenth International Congress on Artificial Materials for Novel Wave Phenomena (Metamaterials) (IEEE, 2022), pp. 142–144 (cit. on pp. 33, 53, 75).

[79]J. Feis, L. Solymar, and E. Shamonina, "Topological wireless communication in the stopband of magnetoinductive lines", Journal of Applied Physics **133** (2023) (cit. on p. 33).

[80]J. Feis, L. Solymar, and E. Shamonina, "Topological wireless power transfer with relay edge states", in Seventeenth International Congress on Artificial Materials for Novel Wave Phenomena (Metamaterials) (IEEE, 2023) (cit. on pp. 33, 95).

[81]W.-P. Su, J. R. Schrieffer, and A. J. Heeger, "Solitons in polyacetylene", Physical Review Letters **42**, 1698 (1979) (cit. on pp. 37, 43).

[82]O. Sydoruk, O. Zhuromskyy, E. Shamonina, and L. Solymar, "Phonon-like dispersion curves of magnetoinductive waves", Applied Physics Letters **87** (2005) (cit. on p. 38).

[83]J. J. Sakurai and J. Napolitano, *Modern Quantum Mechanics* (Cambridge University Press, 2017) (cit. on p. 42).

[84]B.-H. Chen and D.-W. Chiou, "An elementary rigorous proof of bulk-boundary correspondence in the generalized Su-Schrieffer-Heeger model", Physics Letters A **384**, 126168 (2020) (cit. on p. 45).

[85]B. I. Halperin, "Quantized hall conductance, current-carrying edge states, and the existence of extended states in a two-dimensional disordered potential", Physical Review B **25**, 2185 (1982) (cit. on p. 47).

[86]M. C. Rechtsman, J. M. Zeuner, Y. Plotnik, Y. Lumer, D. Podolsky, F. Dreisow, S. Nolte, M. Segev, and A. Szameit, "Photonic Floquet topological insulators", Nature **496**, 196–200 (2013) (cit. on p. 48).

[87]S. Yao and Z. Wang, "Edge states and topological invariants of non-Hermitian systems", Physical Review Letters **121**, 086803 (2018) (cit. on p. 48).

[88]Z. Zhang, H. Pang, A. Georgiadis, and C. Cecati, "Wireless power transfer – an overview", IEEE Transactions on Industrial Electronics **66**, 1044–1058 (2018) (cit. on pp. 54, 76).

[89]D. Alley, *Photograph of Nikola Tesla in his laboratory in Colorado Springs.* 1899 (cit. on p. 55).

[90]A. Kurs, A. Karalis, R. Moffatt, J. D. Joannopoulos, P. Fisher, and M. Soljacic, "Wireless power transfer via strongly coupled magnetic resonances", Science **317**, 83–86 (2007), (Figure 3.2(b) used with permission of the AAAS, from this reference; permission conveyed through Copyright Clearance Center, Inc.) (Cit. on pp. 55, 97).

[91]W. Zhong, C. K. Lee, and S. R. Hui, "General analysis on the use of Tesla's resonators in domino forms for wireless power transfer", IEEE Transactions on Industrial electronics **60**, 261–270 (2011), (Figure 3.2(c) used with permission of the IEEE, from this reference; permission conveyed through Copyright Clearance Center, Inc.) (Cit. on p. 55).

[92]L. Wheeler, "II — Tesla's contribution to high frequency", Electrical Engineering **62**, 355–357 (1943) (cit. on p. 54).

[93]N. Tesla, *System of transmission of electrical energy.* US Patent 645,576, 1900 (cit. on p. 55).

[94]N. Tesla, *Apparatus for transmission of electrical energy.* US Patent 649,621, 1900 (cit. on p. 55).

[95]N. Tesla, *Apparatus for utilizing effects transmitted from a distance to a receiving device through natural media.* US Patent 685,955, 1901 (cit. on p. 55).

[96]N. Tesla, *My Inventions: the Autobiography of Nikola Tesla* (Cosimo Classics, 2010) (cit. on p. 55).

[97]M. Song, P. Jayathurathnage, E. Zanganeh, M. Krasikova, P. Smirnov, P. Belov, P. Kapitanova, C. Simovski, S. Tretyakov, and A. Krasnok, "Wireless power transfer based on novel physical concepts", Nature Electronics **4**, 707–716 (2021) (cit. on pp. 56, 73, 107).

[98]S. Assawaworrarit, X. Yu, and S. Fan, "Robust wireless power transfer using a nonlinear parity–time-symmetric circuit", Nature **546**, 387–390 (2017) (cit. on p. 56).

[99]Y. Xie, Z. Zhang, Y. Lin, T. Feng, and Y. Xu, "Magnetic quasi-bound state in the continuum for wireless power transfer", Physical Review Applied **15**, 044024 (2021) (cit. on p. 56).

[100]L. Zhang, Y. Yang, Z. Jiang, Q. Chen, Q. Yan, Z. Wu, B. Zhang, J. Huangfu, and H. Chen, "Demonstration of topological wireless power transfer", Science Bulletin **66**, 974–980 (2021) (cit. on pp. 56, 107).

[101]J. Song, F. Yang, Z. Guo, X. Wu, K. Zhu, J. Jiang, Y. Sun, Y. Li, H. Jiang, and H. Chen, "Wireless power transfer via topological modes in dimer chains", Physical Review Applied **15**, 014009 (2021) (cit. on p. 56).

[102]F. Yang, J. Song, Z. Guo, X. Wu, K. Zhu, J. Jiang, Y. Sun, H. Jiang, Y. Li, and H. Chen, "Actively controlled asymmetric edge states for directional wireless power transfer", Optics Express **29**, 7844–7857 (2021) (cit. on p. 56).

[103]E. Shamonina, V. Kalinin, K. Ringhofer, and L. Solymar, "Imaging, compression and Poynting vector streamlines for negative permittivity materials", Electronics Letters **37**, 1 (2001) (cit. on p. 58).

[104]G. Puccetti, C. J. Stevens, U. Reggiani, and L. Sandrolini, "Experimental and numerical investigation of termination impedance effects in wireless power transfer via metamaterial", Energies **8**, 1882–1895 (2015) (cit. on p. 63).

[105]L. Yerra and P. C. Reddy, "Effects of electromagnetic interference on implanted cardiac devices and their management", Cardiology in Review **15**, 304–309 (2007) (cit. on p. 67).

[106]K. Lu, G. Xia, Y. Tang, F. Teng, J. Luo, and L. Tan, "Research on electromagnetic compatibility of high precision measurement system", in 6th International Conference on Measurement Instrumentation and Electronics (ICMIE) (IEEE, 2022), pp. 55–60 (cit. on p. 67).

[107]M. W. Dewhirst, B. Viglianti, M. Lora-Michiels, M. Hanson, and P. Hoopes, "Basic principles of thermal dosimetry and thermal thresholds for tissue damage from hyperthermia", International Journal of Hyperthermia **19**, 267–294 (2003) (cit. on p. 67).

[108]M. Sumption, J. Murphy, M. Susner, and T. Haugan, "Performance metrics of electrical conductors for aerospace cryogenic motors, generators, and transmission cables", Cryogenics **111**, 103171 (2020) (cit. on p. 67).

[109]B. Warwick, *The Handbook of Risk* (Wiley, 2003) (cit. on p. 69).

[110]M. Scollon and M. P. Kennett, "Persistence of chirality in the Su-Schrieffer-Heeger model in the presence of on-site disorder", Physical Review B **101**, 144204 (2020) (cit. on p. 72).

[111]S. Bilicz, S. Gyimothy, J. Pavo, L. L. Toth, Z. Badics, and B. Bálint, "Modeling of resonant wireless power transfer with integral formulations in heterogeneous media", IEEE Transactions on Magnetics **52**, 1–4 (2015) (cit. on p. 73).

[112]R. Lin and J. S. Ho, "A DIY approach to wearable sensor networks", Nature Electronics **4**, 771–772 (2021), (Figure 4.1(b) reproduced from this reference with permission from Springer Nature.) (Cit. on pp. 76, 77).

[113]X. Tan, Z. Sun, and I. F. Akyildiz, "Wireless underground sensor networks: MI-based communication systems for underground applications", IEEE Antennas and Propagation Magazine **57**, 74–87 (2015), (Figure 4.1(c) used with permission of the IEEE, from this reference; permission conveyed through Copyright Clearance Center, Inc.) (Cit. on pp. 76, 84).

[114]H. Stockman, "Communication by means of reflected power", Proceedings of the IRE **36**, 1196–1204 (1948) (cit. on p. 76).

[115]V. Coskun, K. Ok, and B. Ozdenizci, *Near Field Communication (NFC): From Theory to Practice* (Wiley, 2012) (cit. on p. 76).

[116]I. F. Akyildiz, P. Wang, and Z. Sun, "Realizing underwater communication through magnetic induction", IEEE Communications Magazine **53**, 42–48 (2015) (cit. on pp. 76, 108).

[117]M. C. Domingo, "Magnetic induction for underwater wireless communication networks", IEEE Transactions on Antennas and Propagation **60**, 2929–2939 (2012) (cit. on p. 76).

[118]S. Kisseleff, I. F. Akyildiz, and W. H. Gerstacker, "Survey on advances in magnetic induction-based wireless underground sensor networks", IEEE Internet of Things Journal **5**, 4843–4856 (2018) (cit. on p. 76).

[119]T. E. Abrudan, O. Kypris, N. Trigoni, and A. Markham, "Impact of rocks and minerals on underground magneto-inductive communication and localization", IEEE Access **4**, 3999–4010 (2016) (cit. on p. 76).

[120]Z. Sun and I. F. Akyildiz, "Magnetic induction communications for wireless underground sensor networks", IEEE Transactions on Antennas and Propagation **58**, 2426–2435 (2010) (cit. on p. 76).

[121]V. Coskun, B. Ozdenizci, and K. Ok, "A survey on near field communication (NFC) technology", Wireless Personal Communications **71**, 2259–2294 (2013) (cit. on p. 77).

[122]S. Jiang, X. Liu, J. Liu, D. Ye, Y. Duan, K. Li, Z. Yin, and Y. Huang, "Flexible metamaterial electronics", Advanced Materials **34**, 2200070 (2022) (cit. on p. 77).

[123]D. M. Pozar, *Microwave Engineering* (Wiley, 2012) (cit. on p. 81).

[124]Z. N. Chen, *Antennas for Portable Devices* (John Wiley & Sons, 2007) (cit. on p. 85).

[125]Z. Wu, B. Deng, J. Liu, and B. Zeng, "Highly efficient microwave heating for target area based on metamaterial", Microwave and Optical Technology Letters **59**, 758–761 (2017) (cit. on p. 85).

[126]M.-R. Tofighi and J. R. Pardeshi, "Interference enhanced biomedical antenna for combined heating and radiometry application", IEEE Antennas and Wireless Propagation Letters **16**, 1895–1898 (2017) (cit. on p. 85).

[127]E. A. Kwizera, S. Stewart, M. M. Mahmud, and X. He, "Magnetic nanoparticle-mediated heating for biomedical applications", Journal of Heat Transfer **144**, 030801 (2022) (cit. on p. 85).

[128]A. Goldsmith, *Wireless Communications* (Cambridge University Press, 2005) (cit. on pp. 85, 87, 91).

[129]R. Syms and L. Solymar, "Noise in metamaterials", Journal of Applied Physics **109** (2011) (cit. on p. 91).

[130]J. Feis, L. Solymar, and E. Shamonina, "Topological wireless links with relay edge states", in preparation (2023) (cit. on p. 95).

[131]B. Xie, H.-X. Wang, X. Zhang, P. Zhan, J.-H. Jiang, M. Lu, and Y. Chen, "Higher-order band topology", Nature Reviews Physics **3**, 520–532 (2021) (cit. on p. 105).

[132]M. Rudner and N. H. Lindner, "Band structure engineering and non-equilibrium dynamics in Floquet topological insulators", Nature Reviews Physics **2**, 229–244 (2020) (cit. on p. 105).

[133]N. Okuma and M. Sato, "Non-Hermitian topological phenomena: a review", Annual Review of Condensed Matter Physics **14**, 83–107 (2023) (cit. on p. 105).

[134]I. Khromova, "Charging matters", Cambridge Wireless Journal **2**, 27–31 (2019) (cit. on p. 106).

[135]G. Dima, A. Radkovskaya, C. J. Stevens, L. Solymar, and E. Shamonina, "Design of a remote, multi-range conductivity sensor", Sensors **23**, 9711 (2023) (cit. on p. 107).

List of Figures

1.1 Introductory illustration on metamaterials: homogenisation, examples of different metamaterials. . . . 4
1.2 Magnetic resonators: circuit diagram, spectrum, implementations at different operation frequencies. . . . 7
1.3 Illustration of magnetic coupling of wire loops . . . 10
1.4 Illustration of a monoatomic magnetoinductive line . . . 14
1.5 Dispersion characteristics of a monoatomic magnetoinductive line . . . 17
1.6 Current eigenvectors for a monoatomic magnetoinductive line . . . 18
1.7 Topology as a filing system for mathematical objects . . . 20
1.8 Winding number as a topological invariant . . . 21
1.9 Illustration of a monoatomic tight-binding model in one dimension . . . 24
1.10 Quantum Hall effect . . . 27

2.1 Illustrations of diatomic models . . . 37
2.2 Dispersion characteristics of an infinite diatomic magnetoinductive line . 40
2.3 Winding number of the diatomic chain . . . 44
2.4 Resonances of a diatomic magnetoinductive line . . . 46
2.5 Illustration of interfaces between topologically trivial and topologically non-trivial phases . . . 48
2.6 Current profile of topological edge states . . . 49

3.1 Sketch of a wireless power transfer system based on a diatomic magnetoinductive line . . . 54
3.2 Illustrations for introduction to wireless power transfer . . . 55
3.3 Asymmetric edge state through superposition . . . 57
3.4 Effect of edge element detuning on frequencies of the topological edge states . . . 61
3.5 Topological edge state frequency as function of detuning reactance . . . 62
3.6 Optimised efficiency . . . 64
3.7 Load impedance for optimised power transfer efficiency . . . 65
3.8 Current profile for topological wireless power transfer . . . 67
3.9 Bulk current ratio for efficiency-optimised line . . . 68
3.10 Efficiency fluctuation due to mutual impedance disorder . . . 70

3.11 Efficiency fluctuation due to self-impedance disorder 71

4.1 Proposed use cases of magnetoinductive wave communication 76
4.2 Simplified model for power dissipation by a receiving load resistance in the presence of a source resistance 77
4.3 Sketch of a wireless communication system based on a diatomic magnetoinductive line 79
4.4 Optimisation of the signal power for different ratios of the coupling coefficients 80
4.5 Current for optimal signal transmission through topological line 82
4.6 Optimal signal power profiles for monoatomic, topological and trivial lines 83
4.7 Random accessibility of topological and monoatomic chains 84
4.8 Average signal power enhancement factor achieved by the topological chain compared to the monoatomic chain as a function of disorder strength of coupling disorder 87
4.9 Signal power spectrum for a constant load impedance optimised for maximum signal power at $\omega = \omega_0$ 88
4.10 Scaling of the bandwidth with losses 89
4.11 Scaling of the optimum signal power with losses 90
4.12 Enhancement of the Shannon capacity by employing the topological chain instead of the conventional monoatomic chain for varying quality factor Q and noise power level N_0 91

5.1 Scaling of the optimised transfer efficiency of topological and conventional wireless power transfer with increase in chain length 96
5.2 Illustration of the vanishing overlap for exponentially decaying mode profiles and sketch of the construction of a topological diatomic magnetoinductive waveguide with a topological relay interface 98
5.3 Resonances of a topological magnetoinductive waveguide with a topological relay interface at its centre for varying coupling ratio 99
5.4 Optimum wireless power transfer efficiency spectrum and impact of disorder on power transfer efficiencies for topological diatomic magnetoinductive lines without, with one and with two relay interfaces 100
5.5 Optimum signal power spectrum for topological diatomic magnetoinductive lines without, with one and with two relay interfaces 102

List of Tables

1.1 Symmetry classes for the topological classification of Hamiltonians 30

Acknowledgement

A number of people have assisted me along the journey of this project. Here, I would like to express my gratitude to them.

I would like to thank my supervisors, Prof. Katya Shamonina and Prof. Chris Stevens for giving me the opportunity to embark on this journey with them and accompanying me on it with guidance, encouragement and patience. I would also like to express my gratitude to Prof. Laszlo Solymar for his insightful advice. Further, I would like to thank Grahame Faulkner, for his invaluable assistance with so many things. Also, I am grateful to the staff at the Department of Engineering Science and Christ Church for their support. Without naming all of them individually (though rest assured, I have not forgotten anybody), the many people from the Oxford Metamaterials group and also the colleagues from our office in the Information Engineering I would like to thank for many interactions of the scientific but also the purely social kind. I would also like to express my gratitude to my girlfriend Cerys and my family for their support - thank you for always being there for me.

Finally, I would like to acknowledge financial support by the University of Oxford through a Scatcherd European scholarship and by the Engineering and Physical Sciences Research Council through a Doctoral Training Account.